TAMPEREEN TEKNILLINEN YLIOPISTO
TAMPERE UNIVERSITY OF TECHNOLOGY

Juha Kontio

Fabrication of Sub-Wavelength Photonic Structures by Nanoimprint Lithography

Julkaisu 1131 • Publication 1131

Tampere 2013

Tampereen teknillinen yliopisto. Julkaisu 1131
Tampere University of Technology. Publication 1131

Juha Kontio

Fabrication of Sub-Wavelength Photonic Structures by Nanoimprint Lithography

Thesis for the degree of Doctor of Science in Technology to be presented with due permission for public examination and criticism in Sähkötalo Building, Auditorium S1, at Tampere University of Technology, on the 24th of May 2013, at 12 noon.

Tampereen teknillinen yliopisto - Tampere University of Technology
Tampere 2013

ISBN 978-952-15-3073-9 (printed)
ISBN 978-952-15-3083-8 (PDF)
ISSN 1459-2045

"Ohoh seppo Ilmarinen, takoja iän-ikuinen!
Aura kultainen kuvoa, hope'inen huolittele!
Sillä kynnät kyisen pellon, käärmehisen käännättelet."

"O, thou blacksmith, Ilmarinen, The eternal wonder-forger, Forge thyself a golden plowshare, Forge the beam of shining silver, Thou canst plow the field of serpents, Plow the hissing soil of Hisi."

-Kalevala[†]

[†]By Elias Lönnrot (1849), English translation by John Martin Crawford (1888)

Abstract

Nanoimprint lithography (NIL) is a novel but already a mature lithography technique. In this thesis it is applied to the fabrication of nanophotonic devices using its main advantage: the fast production of sub-micron features in high volume in a cost-effective way.

In this thesis, fabrication methods for conical metal structures for plasmonic applications and sub-wavelength grating based broad-band mirrors are presented. Conical metal structures, nanocones, with plasmonic properties are interesting because they enable concentrating the energy of light in very tight spots resulting in very high local intensities of electromagnetic energy. The nanocone formation process is studied with several metals. Enhanced second harmonic generation using gold nanocones is presented. Bridged-nanocones are used to enhance Raman scattering from a dye solution.

The sub-wavelength grating mirror is an interesting structure for photonics because it is very simple to fabricate and its reflectivity can be extended to the far infrared wavelength range. It also has polarization dependent properties which are used in this thesis to stabilize the output beam of infrared semiconductor disk laser.

NIL is shown to be useful a technique in the fabrication of nanophotonic devices in the novel and rapidly growing field of plasmonics and also in more traditional, but still developing, semiconductor laser applications.

Preface

It has been a privilege to work in the scientific environment of the Optoelectronics Research Centre, Tampere University of Technology, during these years. All the work presented in this thesis was done here. It has been supported by the projects of *Academy of Finland*, the *European Commission* and *Tekes*. I'm also grateful of personal financial support from *TUT President's Doctoral Programme*, *Emil Aaltosen säätiö*, *Jenny ja Antti Wihurin rahasto* and *Ulla Tuomisen säätiö*.

The greatest acknowledgment for the completion of this Thesis goes to my supervisors, professor Tapio Niemi and Ph.D. Janne Simonen. They have been the taskmasters and counselors who have pushed me forward even when all my hope has gone. Great thanks goes to professor emeritus Markus Pessa whose lifework has been an adamant bedrock to build my scientific research on.

I want to thank Dr. Pirjo Leinonen and Dr. Jukka Viheriälä for guiding me along the pathway to the source of those alchemical secrets which are commonly called processing. Special thanks to ORC's former laborant Emmi Blad who in a motherly way instructed me to use those Venus tweezers properly and revealed that there are sample sucking black holes in the cleanroom.

I wish to express my gratitude to all the processing personnel during the years, especially Jarkko Telkkälä, Lauri Rajala, Risto Rönkkö, Pasi Pietilä, Juha Tommila, Matti Haavisto, Kimmo Haring, Maija Karjalainen, Mariia Bister, Mervi Koskinen, Ivy Saha Roy, Heidi Tuorila and Milla-Riina Viljanen. I want to also thank ORC's MBE-group. You are truly the spine of ORC. I also acknowledge the guys of command and service troops: lab über-engineer Ilkka Hirvonen and Bengt Holsmström and ORC's champions against the university's bureaucracy: Anne Viherkoski and Eija Heliniemi. Thanks for

all the help during the years.

Great thanks also goes to professor Martti Kauranen, Dr. Hannu Husu, M.Sc. Mikko Huttunen, Dr. Godofredo Bautista and M.Sc. Jouni Mäkitalo in the Nonlinear Optics group. Their expertise in nonlinear and nanophotonic phenomena was invaluable in realizing this Thesis.

My compliment also goes to professor Markku Kuittinen and Dr. Janne Laukkanen in the University of Eastern Finland and Kari Leinonen in the Karelia University of Applied Sciences for all the help with the NIL master fabrication with e-beam lithography.

I want also thank M.Sc. Jukka-Pekka Alanko and Dr. Antti Härkönen for all the help with VECSEL measurements and Dr. Antti Tukiainen, M.Sc. Teemu Hakkarainen, M.Sc. Riku Koskinen and Dr. Turkka Salminen with other experimental data collection sessions.

I express my gratitude to ORC's afternoon coffee group at cafe Voltti, where no subject is a taboo for open discussion. I also acknowledge Miss Paulig for her charming service of chocolate, coffee and the free extra cup.

I have a privilege of having so good friends in Etelä-Pohjanmaa and Tampere, especially those who in *#bukkis* know that typos are the salt of all the writing. Thanks for all the support during my life. You have made life worth living.

I would also like to thank Dr. Antti Härkönen for superb LaTeX thesis template which has made my life a little bit easier during writing this thesis.

And a final than you to my parents, Heikki and Marja-Liisa, brother Kari, sister Kaija and her family for letting me be this "kiriaviisas" of the family.

Tampere, May 2013
Juha Kontio

Contents

List of Publications

This thesis is a compendium, which contains some unpublished material, but is mainly based on the following papers published in open literature.

[P1] J.M. Kontio, H. Husu, J. Simonen, M.J. Huttunen, J. Tommila, M. Pessa, and M. Kauranen, "Nanoimprint fabrication of gold nanocones with ∼10 nm tips for enhanced optical interactions," *Optics Letters*, Vol. 34, No. 14, pp. 1979–1981 (2009)

[P2] J.M. Kontio, J. Simonen, J. Tommila, and M. Pessa, "Arrays of metallic nanocones fabricated by UV-nanoimprint lithography," *Microelectronic Engineering*, Vol. 87, No. 9, pp. 1711–1715 (2010)

[P3] J.M. Kontio, J. Simonen, K. Leinonen, M. Kuittinen, and T. Niemi, "Broadband infrared mirror using guided-mode resonance in sub-wavelength germanium grating," *Optics Letters*, Vol. 35, No. 15, pp. 2564–2566 (2010)

[P4] S. Rao, M.J. Huttunen, J.M. Kontio, J. Mäkitalo, M-R. Viljanen, J. Simonen, M. Kauranen, and D. Petrov, "Tip-enhanced Raman scattering from bridged nanocones," *Optics Express*, Vol. 18, No. 23, pp. 23790–23795 (2010)

Author's contribution

Teamwork has been an essential part of the work presented in this thesis and it has involved NIL master and stamp fabrication, device processing, optical measurements and simulations. The author's main contribution in all publications has been sample fabrication and the development of the processes. Especially the lift-off process and nanocone fabrication procedures were the author's areas of expertise.

In P1 the author developed the nanocone process, fabricated the samples and characterized their dimensions. The author also participated the planning of the measurements and was the corresponding author of the paper.

In P2 the author was responsible for the fabrication of all of the samples, testing, characterization and analysis of the nanocones except for the finite-element simulations. The author was a co-author in the writing of the paper.

In P3 the author developed the fabrication process, fabricated the samples, planned the measurements and partly conducted them. The author was the corresponding author of the paper.

In P4 the author developed the main concept of the bridged nanocones and fabricated the samples. The author was a co-author in the writing of the paper.

List of Abbreviations and Symbols

Abbreviations

AC	Alternating current, p. 9
AFM	Atomic force microscope, p. 31
Ag	Silver, p. 15
AlInP	Aluminum indium phosphide, p. 68
AP	Azimuthal polarization, p. 65
Ar	Argon, p. 40
ARDE	Aspect ratio dependent etching, p. 28
Au	Gold, p. 9
BEM	Boundary element method, p. 24
CHF_3	Trifluoromethane, p. 40
CV	Crystal violet, p. 66
DFB	Distributed feedback lasers, p. 27
DFG	Difference-frequency generation, p. 20
EBL	Electron beam lithography, p. 36
EM	Electromagnetic, p. 5
EsB	Energy and angle selective backscatter detector, p. 32
EUV	Extreme ultraviolet, p. 37
FDTS	Perfluorodecyltrichlorosilane, p. 28
FEM	Finite element method, p. 22
FIB	Focused ion beam, p. 37
FMM	Fourier modal method, p. 23
Ge	Germanium, p. 3
GMR	Guided-mode resonance, p. 6
h-PDMS	Hard-poly(dimethylsiloxane), p. 28

IC	Integrated circuit, p. 33
ICP	Inductively coupled plasma, p. 48
IR	Infrared, p. 22
ITRS	International Technology Roadmap for Semiconductors, p. 37
J-FIL	Jet and Flash Imprint Lithography, p. 32
LIL	Laser interference lithography, p. 36
LSP	Localized surface plasmon, p. 16
MBE	Molecular beam epitaxy, p. 3
MIM	Metal-insulator-metal, p. 53
MoM	Method of moments, p. 24
MPTMS	(3-mercaptopropyl)trimethoxysilane, p. 52
NA	Nanoantenna, p. 18
NIL	Nanoimprint lithography, p. 2
NP	Nanoparticle, p. 9
NSOM	Near-field scanning optical microscopy, p. 14
O_2	Oxygen, p. 32
ORC	Optoelectronics Research Centre, p. 28
PDE	Partial differential equation, p. 23
PMGI	Polydimethylglutarimide , p. 40
PMMA	Polymethylmethacrylate, p. 36
QW	Quantum well, p. 3
RCWA	Rigorous coupled-wave analysis, p. 23
RIE	Reactive ion etching, p. 48
RP	Radial polarization, p. 65
s-PDMS	Soft-poly(dimethylsiloxane), p. 28
SDL	Semiconductor disk laser, p. 73
SEM	Scanning electron microscope, p. 31
SHG	Second-harmonic generation, p. 19
SERS	Surface enhanced Raman scattering, p. 21
SFG	Sum-frequency generation, p. 20
$SiCl_4$	Silicon tetrachloride, p. 40
SiN_x	Silicon nitride, p. 43
SiO_2	Silicon dioxide, p. 15

SP	Surface plasmon, p. 12
SPL	Scanning probe lithography, p. 38
SPP	Surface-plasmon polariton, p. 2
SPR	Surface plasmon resonance, p. 13
SRR	Split-ring resonator, p. 65
TEM	Transmission electron microscope, p. 38
TERS	Tip-enhanced Raman scattering, p. 22
THG	Third-harmonic generation, p. 19
UV-NIL	Ultraviolet nanoimprint lithography, p. 25
VECSEL	Vertical external-cavity surface-emitting lasers, p. 73

Symbols, Greek alphabet

α_i	Polarizability, p. 16
ε_0	Electric permittivity of the vacuum, p. 5
ε_{air}	Relative permittivity of air, p. 15
ε_d	Permittivity of a dielectric, p. 13
ε_m	Relative permittivity of the metal, p. 15
ε_r	Relative permittivity, p. 5
θ	Angle of incidence, p. 13
κ	Extinction coefficient, p. 5
μ_0	Magnetic permeability in vacuum, p. 5
μ_r	Relative permeability, p. 5
ρ	Charge density, p. 5
σ	Conductivity, p. 5
χ	Dielectric susceptibility, p. 5
ω	Angular frequency, p. 5
ω_p	Plasma frequency, p. 11

Symbols, other

B	Magnetic flux density, p. 5
D	Electric displacement, p. 5
e	unit charge of electron, p. 11
E	Electric field, p. 5
$\hbar$	Dirac constant (Planck constant divided by 2π), p. 11
H	Magnetic field, p. 5
J	Current density, p. 5
k_{SPP}	Wave vector of the surface plasmon polariton, p. 13
k_{x}	x-component of the wave vector of the incident beam, p. 13
l_s	Skin depth, p. 14
n	Index of refraction, p. 5
n	Electron density, p. 11
m	Mass, p. 11
r	Radius, p. 16
$\mathbb{Z}$	Integer, p. 13

Chapter 1

Introduction

In the history of mankind, the trend of development of tools has been towards both extremes in size: larger and smaller. Nowadays we have cranes that can be used for in building high skyscrapers such as Burj Khalifa in Dubai. Professor Richard Feynman once said that ”There’s plenty of room at the bottom” [1]. This is very true as it has become a commonplace to shape matter in nanometer-scale. This is nanotechnology[†].

It might be claimed that nanotechnology is only nano-hype because there is nothing fundamentally new that has not been around since the 60s or 70s. I truly see nanotechnology as a revolution because it has enabled not only scientists or researchers, but also industry to control and shape matter in nanoscale for commercial products. In addition to controlling matter, it is now feasible to control light in ways that have not been possible before. This is nanophotonics.

Nanophotonics offers tools and technology for controlling and shaping electromagnetic fields, in other words light, using structures which are often smaller in size than the wavelengths of visible light. Light can be, for example, a coherent laser beam or incoherent sunlight. The sub-wavelength nature results in extraordinary optical properties that are almost irrational compared to classical optics. For example, negative index of refraction, which could enable the dream of many epic sagas, an invisibility cloak, has become possible at least in theory but also in a limited form in laboratories.

The main driving force behind the development of nanotechnology is advanced lithog-

[†]The word ”nano” comes from the Greek word *nanos* and means a midget.

Figure 1.1: *The Lycurgus cup, which is from the 4th century AD [6]. It is located in the British Museum. In the left picture the cup is illuminated from outside and in the right the same cup is illuminated from the inside. The color difference is caused by metal nanoparticles embedded in the glass. Reprinted with permission of the British Museum.*

raphy techniques. Traditional photolithography is limited by the diffraction of light. Its limits have been extended by using smaller wavelengths [2] and immersion lithography [3].

To overcome these restrictions Chou et al. presented nanoimprint lithography (NIL) based on molding in 1995 [4]. This NIL technique does not suffer from the limitations caused by the wavelength of light. Instead, it is limited by the accuracy of the mechanical systems and the properties of the materials used in the imprint process. Hua et al. have demonstrated that NIL can reach even molecular scale resolution [5].

Plasmonics is a technology which refers to the interaction of light and the free electrons of a conductor, e.g. metal. Light can be confined into the surface of a metal as a propagating surface plasmon polariton (SPP). Plasmons are currently a hot research topic but mankind has been using them for a long time to make beautifully colored glass (Fig. 1.1). Already the ancient Romans mastered the skill to color glass with metals in the 1st century BC [7]. Therefore, plasmons are an old invention but the development of nanotechnology has brought us the tools to control them.

Incentives

I started this work in 2005 when the Optoelectronics Research Centre had acquired a new mask aligner with UV-nanoimprint lithography (UV-NIL) modules. My M.Sc. thesis focused on the fabrication of metal structures using NIL. In that time we were learning to use NIL to make nano-sized patterns, and any nanopattern on a wafer was a triumph.

My task was to test the fabrication of metallic nanostructures using NIL. The results were promising and I was able to make metallic nanostructures over a large area.

When ORC started to invest in metrology equipment and nanophotonics became one of the spearheads in TUT's strategy, NIL-based research really started to move forward. I started my PhD studies in 2006.

The first goal of my PhD work was to combine metallic nanostructures with molecular beam epitaxy (MBE) grown semiconductor quantum wells (QW) using plasmonics. There were some promising results in high level scientific publications in this field [8]. After a large collection of destroyed NIL stamps and semiconductor QW wafers we concluded that by using our fabrication tools and methods this was not possible.

Luckily, I accidentally fabricated conical gold structures, nanocones, which were fascinating from plasmonics point of view. By using nanocones, light can be concentrated into tight spots in the tips of the nanocones. Nanocones were used in P1 to demonstrate the enhancement of second-harmonic generation in the tips of the nanocones.

Our versatile process can also produce more complex structures. To demonstrate this, we used bridged nanocones to enhance tip-enhanced Raman scattering (TERS) from dye molecules in P4, which is discussed in detail in Chapter 5.1.

During testing of the nanocone formation in P2 we observed that germanium (Ge) can be used to fabricate smooth structures. Ge is interesting because it is a dielectric material with a high index of refraction in infrared wavelengths. We used these properties to design a guided-mode resonance mirror in P4. The polarization selectivity of the mirror was used in stabilization of a semiconductor disk laser.

This thesis is combination of applications of plasmonic and photonic structures fabricated by UV-NIL. It will give the reader an overview of plasmonics and detailed descriptions of various aspects of nanofabrication. The theory of SHG and TERS and the numerical methods used are discussed in a level relevant to the work done in this thesis.

Chapter 2

Theoretical background

In this chapter the theoretical background of the thesis is discussed. Although the focus of the thesis is mainly in applications it is essential to comprehend the theory. In many cases physical insight is the key to tackle the problem, but usually the structures are too complex to understand only with intuition. Therefore, simulations are needed to explore the mechanisms behind the phenomena.

First, Maxwell's equations are presented because they are the basis of understanding almost all optical phenomena. The results and predictions of this elegant fundamental theory affect our everyday life, providing tools for engineering cell phones and understanding the colors of the rainbow.

2.1 Fundamentals: Maxwell's equations

James Clerk Maxwell presented his famous equations in 1861 [9] and they are considered to be central results of physics among Newton's laws of motion, quantum mechanics and Einstein's theory of relativity. Oliver Heaviside later used vector analysis formalism to describe Maxwell's 20 original equations [10] and was able to present them in a

compact form of the well-known vectorial equations

$$\nabla \cdot \mathbf{D} = \rho \tag{2.1}$$

$$\nabla \cdot \mathbf{B} = 0 \tag{2.2}$$

$$\nabla \times \mathbf{E} = -\frac{\partial \mathbf{B}}{\partial t} \tag{2.3}$$

$$\nabla \times \mathbf{H} = \mathbf{J} + \frac{\partial \mathbf{D}}{\partial t} \tag{2.4}$$

where **D** is the electric displacement, **E** is the electric field, **H** is the magnetic field, **B** is the magnetic flux density, ρ the charge density and **J** the current density.

The fields are also connected to the other related physical magnitudes with the formulas

$$\mathbf{D} = \varepsilon_0 \mathbf{E} + \mathbf{P} = \varepsilon_0 \mathbf{E} + \varepsilon_0 \chi \mathbf{E} \tag{2.5}$$

$$\mathbf{H} = \frac{1}{\mu_0 \mu_r} \mathbf{B} \tag{2.6}$$

where ε_0 is the electric permittivity and μ_0 is the magnetic permeability in vacuum respectively. μ_r is the the relative permeability (= 1 for a nonmagnetic material). **P** is the electric dipole moment per unit volume. Usually the relation between **P** and **E** is expressed by dielectric susceptibility $\chi = \varepsilon_r - 1$, which describes how easily a dielectric material polarizes in a response to an electric field. ε_r is the relative permittivity.
Current density **J** is linked to the electric field **E** via conductivity σ as

$$\mathbf{J} = \sigma \mathbf{E}. \tag{2.7}$$

Relative permittivity ε_r can be expressed in a complex form

$$\varepsilon_r = \varepsilon_1 + i\varepsilon_2 = \varepsilon_1 + i\frac{\sigma}{\omega \varepsilon_0} \tag{2.8}$$

where ε_1 is real part of electric permittivity, ε_2 is the imaginary part and ω is the angular frequency. The index of refraction n can be defined from the relative permittivity as

$$n = \sqrt{\varepsilon_r} = n_0 + i\kappa. \tag{2.9}$$

It describes the optical density of material. κ is the extinction coefficient, which quantifies the absorption or gain of the electromagnetic (EM) field in the medium.

2.2 Nanophotonics

Nanophotonics is a large research field, studying the peculiar properties of light and light-matter interaction in nanostructures. In this section the basic concepts of diffraction, guided-mode resonance (GMR), plasmonics, nonlinear optics and Raman scattering are introduced.

2.2.1 Guided-mode resonance

Guided-mode resonance is an optical phenomenon where a grating and a waveguide are optically coupled, which dramatically alters the optical response of the grating [11, 12]. This can be seen as either high reflection or transmission of the grating. These spectral features can be very narrow because of the resonant nature of the coupling. GMR type phenomena were at first observed by Wood et. al 1902 [13]. They are known as Wood's anomalies in optical gratings and were explained in 1965 by Hessel et al. [14] using the term "guided complex waves supportable by the grating". The initiator of the new GMR era was Prof. Robert Magnusson [15]. He and his colleagues proposed GMR to be exploited in filters and reflectors.

Before going into details of the GMR, the basic concepts of diffraction gratings are presented.

Diffraction in gratings

In grating diffraction, multiples of the grating vector are added to the wavevector of the incident field to produce the wavevector of the diffracted field:

$$k_{\mathrm{xi}} + mG = k_{\mathrm{xd}}. \tag{2.10}$$

Here k_{xi} is the horizontal component of the wavevector of the incident field, $G = \frac{2\pi}{\Lambda}$ is the grating vector and k_{xd} is the horizontal component of the wavevector of the diffracted field and $m \in \mathbb{Z}$ is the diffraction order. This equation determines the directions where the diffracted field is directed as illustrated in Fig. 2.1. The length of the wavevector is $|k_d| = |\frac{2\pi}{\lambda}|$.

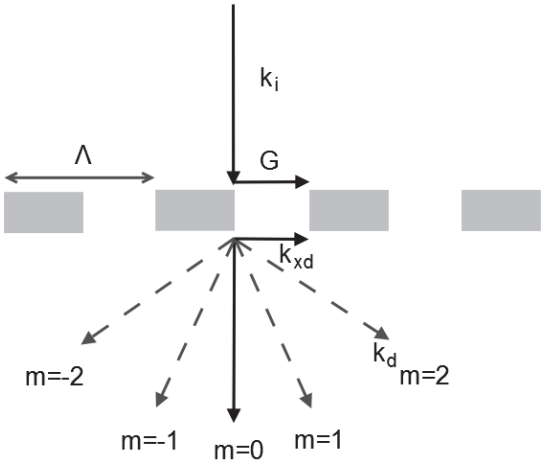

Figure 2.1: *Diffraction in a transmission grating. The phase matching requirement causes the length of the wavevector of the diffracted field to fulfill Eq. 2.10.*

Traditionally, gratings have been used for dividing a light beam into spectral components. The diffraction equation can be derived from the phase-matching relation (2.10) as

$$n_1 \sin\theta_i - n_2 \sin\theta_d = \frac{\lambda_0}{\Lambda} m \tag{2.11}$$

where θ_i and θ_d are the angles of the incident and the diffracted fields, n_1 and n_2 are the indices of refraction of the materials, λ_0 is the wavelength of the incident field in vacuum, Λ is the period of the grating and $m \in \mathbb{Z}$ is the diffraction order. Every transmitted wavelength diffracts to its own direction according to Eq. 2.11.

When $\Lambda \to \infty$ in Eq. 2.11, the equation reduces into Snell's law, which describes normal refraction at the boundary of two materials.

Gratings and guided-mode resonance

In guided-mode resonance a grating couples light to a leaky mode of a waveguide. This only takes place at certain incident angles and wavelengths. The mode re-radiates out from the waveguide while propagating and gradually dies out.

Propagation constant β describes how the phase and amplitude of light evolve in the

propagation direction in an optical waveguide. It is defined as

$$|\beta| = \frac{2\pi}{\lambda_0} n_{\text{eff}} \tag{2.12}$$

where λ_0 is the wavelength in vacuum and n_{eff} is the so-called effective index of refraction or modal index. In addition to the materials, it depends on the geometry of the waveguide and is characteristic of each mode supported by the waveguide.

By using a grating on the waveguide it is possible to couple the incoming beam into the waveguide. The coupling condition for the beam entering into the waveguide can be expressed as

$$k_{\text{ti}} + mG = \beta \tag{2.13}$$

where k_{ti} is the tangential component of the wave vector of the incident light beam. For coupling the beam into the waveguide the incident angle should be

$$\sin\theta_{\text{i}} = \frac{1}{n_1}(n_{\text{eff}} + m\frac{\lambda_0}{\Lambda}) \tag{2.14}$$

For the leaky mode the effective index of refraction can be defined [16] as

$$n_{\text{eff}} = n'_{\text{eff}} - in''_{\text{eff}} \tag{2.15}$$

where n'_{eff} is real part of the modal index of refraction and n''_{eff} the complex part of the modal index. It can be shown that the connections between the spectral and spatial bandwidths for efficient coupling are [16]

$$\Delta\lambda_{FWHM} = 2n''_{eff}\Lambda \tag{2.16}$$

$$\Delta\theta_{FWHM} = 2n''_{eff} \tag{2.17}$$

Eq. 2.16 fundamentally means that losses cause widening of the resonance peak which is a common phenomenon. With dielectrics having low losses, sharp resonances can be obtained, leading to narrow filter or reflector bandwidths.

GMR filters can be designed to work as reflectors [17] or narrow band filters [18] by optimizing the structure. Usually the designed structures are polarization dependent but they can also be designed to be polarization independent [19]. The grating can also be designed to operate as a broadband reflector such as in P3. This can take place when

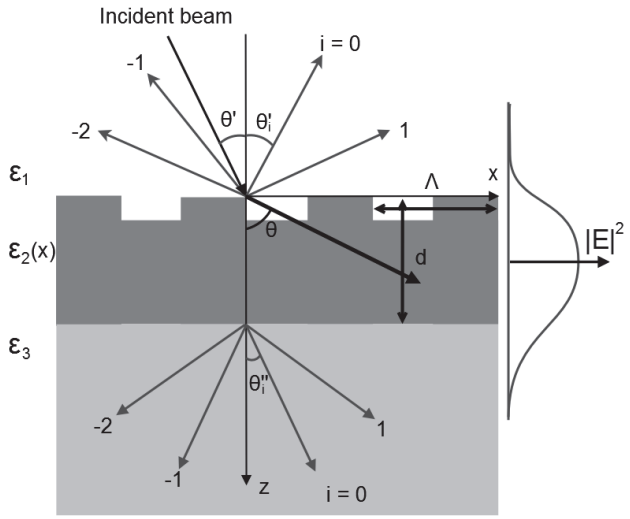

Figure 2.2: *Diffraction in a GMR grating.* θ_i*' are the angles of the ith backward-reflected wave.*

several resonances together form a broad reflecting band. There are no clear rules of thumb for the grating design, but the parameters of the grating structure must be optimized using numerical methods described in Section 2.3.2 to achieve desired operation taking into account fabrication limitations and material parameters.

2.2.2 Plasmonics

Although plasmonics is still quite an unknown branch of science for the public, it has been studied for over 100 years. The biggest application of plasmonics along with glass coloring is still the pregnancy test where pregnancy hormones trigger clustering of colloidal gold (Au) nanoparticles (NP), which leads to a change of color indicating pregnancy [20]. In the following a brief history of the first steps of plasmonics is presented and some milestones highlighted.

History

The very basis of plasmonics is Maxwell's equations, as is the case for all electromagnetism related areas of research. In 1899 Arnold Sommerfeld [21] studied the propagation of the radio waves over a conducting surface, which was the first theoretical

formulation of plasmons.

In the year 1902 Robert W. Wood observed unexplained features in optical reflection measurements of metallic gratings [13]. This observation was a key breakthrough for all resonant phenomena in the gratings.

In 1904 J.C. Maxwell Garnett described the bright colors observed in metal-doped glasses [22] which was a starting point to understanding of the particle plasmons in metal nanoparticles. However, this phenomenon had been known and used in applications for thousands of years (see Fig. 1.1).

In 1908 Gustav Mie studied the scattering of light in a colloidal metal particle solution [23]. This phenomenon is still known as Mie scattering. Also electromagnetic scattering by a homogeneous, isotropic sphere is called as Mie theory, although Alfred Clebsch in 1863 was the first to solve the elastic point source scattering problem of a perfectly rigid sphere using potential functions [24].

In 1956 David Pines suggested that the anomalous energy loss of light in metal foils was due to the excitation of conducting electrons creating plasma oscillation. He introduced the term "plasmon" to describe *"the quantum of elementary excitation associated with this high-frequency collective motion"* [25]. Two years later John Hopfield introduced the word "polariton" for the coupled oscillation of bound electrons and light in transparent media [26].

In 1957 Rufus Ritchie suggested a theory that plasmon modes can exist on the surfaces of metal, which was the first theoretical prediction of surface plasmons [27]. In 1968 Ritchie et al. described the anomalous optical behavior of metal gratings in terms of surface plasmon resonances excited on the gratings [28]. In the same year another invention was made by two groups. Kretchmann and Raether [29] and also Otto [30] in another paper suggested a method for excitation of surface plasmons by a prism. Giving an opportunity for researchers to study the phenomena, these two milestones can be said to be the starting point for modern plasmonics.

In 1970 Kreibig and Zacharias compared the electrical and optical properties of gold and silver in terms of surface plasmons for the first time [31]. The term surface plasmon-polariton (SPP) was introduced by Cunningham in 1974 to describe the measured oscillating modes on doped semiconductors [32].

Simultaneously, one of the biggest application areas of plasmonics was discovered when Fleischmann et al. discovered that a roughened surface of a silver eletrode was enhancing Raman scattering from pyridine [33]. At that time they did not understand the mechanism to be related with plasmons but this lead to development of surface enhanced Raman scattering (SERS) and later tip enhanced Raman scattering (TERS) which is also related to the topic of this thesis.

Plasmons

What is a plasmon? The term gives a hint that it has something to do with plasma, and the "-on"-ending refers to a separate particle or quantum. Fundamentally, a plasmon is a charge density oscillation, i.e. an oscillation of a conductor's electron plasma.

Plasmons can exist in metals, highly-doped semiconductors and other materials with free electron gas [34]. The most common materials for plasmonics are the noble metals.

Bulk plasmons

The quasiparticles of electron gas oscillation in a lattice, such as in bulk metal, are called bulk or volume plasmons. They are classically one-dimensional longitudinal oscillations of a free electron gas in a lattice which has positive ion background of atom nuclei of metal. They are excited by particle impact, which interferes with the free electron gas and causes a longitudinal density wave. However, a recent letter claims that a bulk plasmon does not have a purely longitudinal nature if it is treated as a 3D object [35].

Because of its longitudinal nature, a volume plasmon can not be excited by a transverse electromagnetic wave such as a plane wave. Using the equation of motion for the density fluctuation in an electron gas, we can derive an equation for the plasma frequency ω_p as

$$\omega_p{}^2 = \frac{ne^2}{\varepsilon_0 m} \tag{2.18}$$

where n is the electron density, e the unit charge of the electron, ε_0 is the vacuum permittivity and m the rest mass of the electron. This plasma frequency ω_p can be seen in metal thin films as an energy loss when energetic incident electrons lose energy in the multiples of $\hbar\omega_p$ [36].

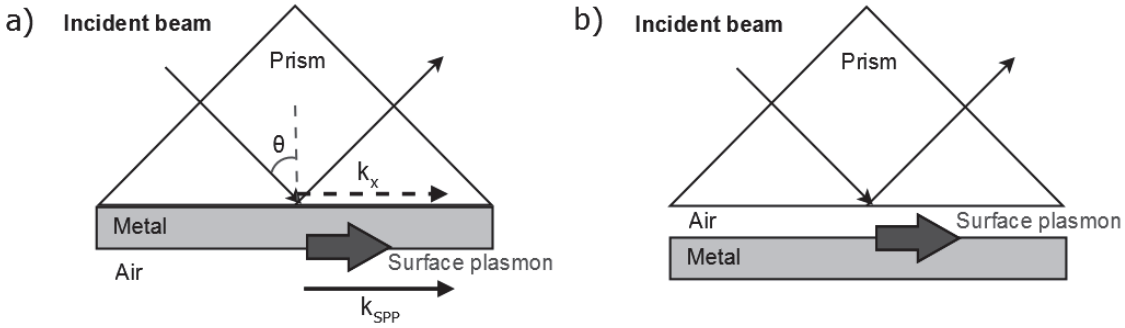

Figure 2.3: *a) The Kretschmann coupling method. b) The Otto coupling method. The blue arrow presents a propagating surface plasmon on the metal surface.*

Surface plasmon polaritons

Surface plasmon polaritons (SPPs) are the main concept of modern plasmonics. SPPs are electromagnetic excitation modes which are propagating at the interface of a dielectric and a conductor. The term "polariton" refers to the quasi-particle nature of the SPPs.

Generally a surface plasmon (SP) is an oscillation of conductor's free electron plasma caused by EM interference, for example by light or an energetic electron beam. A SPP is specifically a photon coupled to the plasmon which is bound to the surface of the metal. SPPs have both a transverse and longitudinal oscillation character.

In 1954 Ritchie et al. [27] investigated the loss spectra of low energy electron beams in thin metallic films. It was expected that there would have been losses at the energy $\hbar\omega_p$ because of the bulk plasmon excitation, but it turned out that the losses were at the energy $\hbar\omega_p/\sqrt{2}$ as predicted by Eq. 2.19, which gives the plasmon frequency ω_{sp} for the SPP as

$$\omega_{sp} = \frac{\omega_p}{\sqrt{1+\varepsilon}} \tag{2.19}$$

where ε is the relative permittivity of the environment, typically air ($\varepsilon = 1$).

Coupling methods Two classical plasmon coupling methods are the Kretschmann (Fig. 2.3a) and Otto configurations (Fig. 2.3b). They both use a prism, but in the Kretschmann configuration a metal layer is deposited on the prism's glass surface. A light beam enters the prism, hits the prism facet with metal in an angle larger than the critical angle for total internal reflection, and an evanescent field excites the propagating

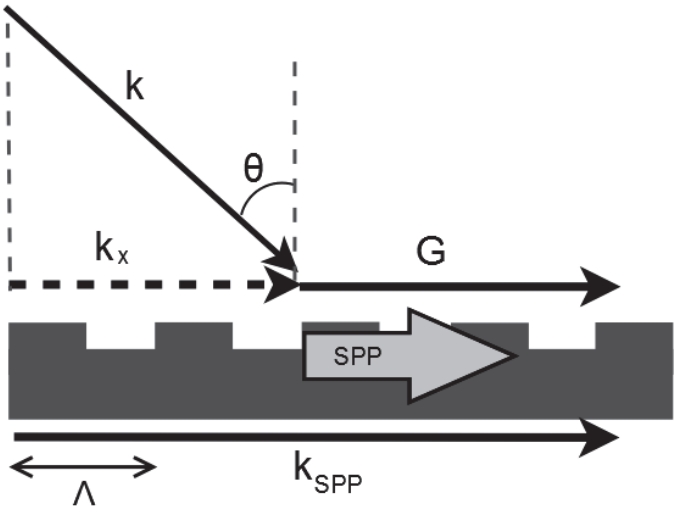

Figure 2.4: *The principle of grating coupling. When the* $\mathbf{k}_x$ *component is boosted with the grating vector* $\mathbf{G}$ *and match the* $\mathbf{k}_{SPP}$*, light is coupled to the metal surface as a surface plasmon polariton.*

plasmon on the metal/air interface. In the Otto configuration there is an air gap between the metal film and the prism surface. The separation must be less than λ for the evanescent field to excite the plasmon on the metal film.

A more advanced coupling method is grating coupling. It is based on a fundamentally the similar concept as described in Chapter 2.2.1 for the gratings on waveguides. The wave vectors of the photon and the surface plasmon are matched and the light couples to the grating as a plasmon. Coupling takes place when the phase-matching, which is similar to Eq. 2.13, is fulfilled:

$$k_{SPP} = k_x + mG \tag{2.20}$$

where k_{SPP} is the wave vector of the SPP, k_x is the x-component of the wave vector of the incident beam, G is the grating vector and $m \in \mathbb{Z}$. The length of k_x can be tuned by changing the angle of incidence θ.

A surface plasmon propagating on the surface of a metal can also be coupled back to light by using a grating [37]. Eq. 2.20 can also be applied to understand the coupling of the random surface roughness which offers a very large number of grating vectors. Therefore, plasmons can scatter from a rough surface to light. This loss mechanism

directly affects the propagation length of the plasmons. A smoother metal surface means a longer propagation length and lifetime for the plasmon polariton.

One of the applications of SPPs is the surface plasmon resonance (SPR) biosensor [38]. They are widely used in the detection of chemical and biological analytes. SPR sensors are based on the prism coupling of SPs. The analyzed biosamples are dispensed over the metal surface where the SPs are propagating. A light beam excites the SPs and the reflected beam is detected as a function of the angle. The SPR excitation can be seen as a dip in the reflectance at the certain angle. The dispensed samples change the refractive index on the surface which leads to the shifting of the resonance peaks. The EM field on the metal surface is exponentially decaying, leading to a high sensitivity near the surface.

Near field excitation is used in near-field scanning optical microscopy (NSOM, a.k.a. SNOM) [39]. It is based on using a metal coated tip with a sub-wavelength aperture. The tip is brought into contact with the metal surface and an evanescent near field from the tip excites the plasmon on the metal surface. By using leakage radiation, an image map of the plasmons in the structure can be formed. The configuration can also be arranged so that the tip is coated with metal and an external laser beam is used to excite plasmons via the tip. This configuration is called apertureless SNOM.

Propagation The propagation length of surface plasmons is limited by two major factors: scattering and attenuation [40]. Normally the maximum plasmon propagation length is only tens of micrometers at visible wavelengths, but with longer wavelengths, e.g. at 1.5 µm, even 1 mm can be reached [41]. Metals have an imaginary part of the dielectric function which means that there will always be losses. This is the main drawback for plasmonics in general. Moreover, scattering from defects couples plasmons back to light and decreases the energy of the plasmons [42]. Therefore it is crucial to have as smooth as possible metal surfaces when the propagation length is a critical issue.

Skin depth l_s represents how deep the electric field of the SPP penetrates into the metal before decaying by a factor of $1/e$. Skin depth can also be stated for the dielectric

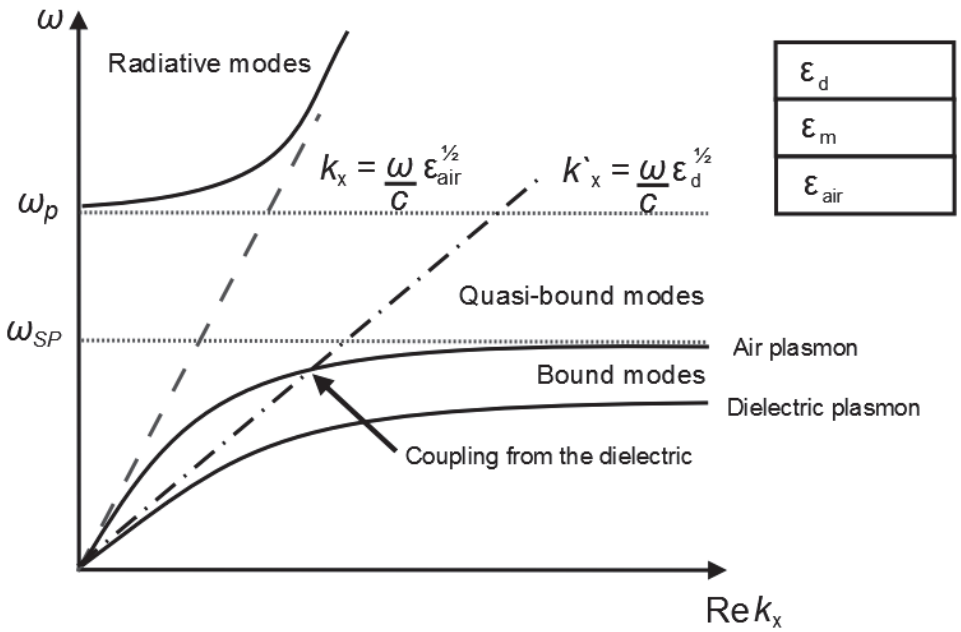

Figure 2.5: *Dispesion relations for plasmons in a dielectric/metal interface. The dashed line is the called light line for the metal/air interface and the dash-dot line is the light line for the metal/dielectric interface.*

side of interface. Singh et al. give the following equation for the skin depth [43]

$$l_s = \sqrt{\frac{2}{\sigma\mu\omega}} \tag{2.21}$$

where σ is the conductivity.

Skin depth reaches its minimum at the surface plasmon resonance wavelength [44]. For silver (Ag) and SiO_2 it is 15 nm at the wavelength of 355 nm. For SPPs in general the skin depth in the metal at longer wavelengths than the surface plasmon resonance is $\sim$20 nm. Skin depth describes how effectively light can be concentrated onto the surface using plasmons.

Dispersion The dispersion relation for plasmons reveals how the optical parameters are connected to each other in the system. For surface plasmons the following equation can be derived using the Eq. 2.18 and $\varepsilon_m = 1 - (\frac{\omega_p}{\omega})^2$ (Drude model for lossless free

electron gas):

$$k_{\mathrm{SPP}} = \frac{\omega}{c}\sqrt{\frac{\varepsilon_{\mathrm{m}}\varepsilon_{\mathrm{d}}}{\varepsilon_{\mathrm{m}}+\varepsilon_{\mathrm{d}}}} = \frac{\omega}{c}\sqrt{\frac{(\omega^2-\omega_{\mathrm{p}}^2)\varepsilon_{\mathrm{d}}}{(1+\varepsilon_{\mathrm{d}})\omega^2-\omega_{\mathrm{p}}^2}} \tag{2.22}$$

$$\omega_{\mathrm{sp}} = \frac{\omega_{\mathrm{p}}}{\sqrt{1+\varepsilon_{\mathrm{air}}}} \tag{2.23}$$

where $\varepsilon_{\mathrm{air}}$, ε_{m} and ε_{d} are the relative permittivities of the air, the metal and the dielectric.

Using Eq. 2.22 dispersion curves can be plotted as shown in Fig. 2.5. The dashed line is the so-called light line. It shows that light cannot be coupled directly into plasmons or vice versa, i.e. light cannot directly excite a plasmon on a perfectly smooth metal surface due to the mismatch of the wave vector. The light line (dashed line) depicts the maximum possible value for k_{x}, which is reached when the angle of incidence θ is 90°, i.e. parallel to the surface. When the light tunnels through the metal to the metal/air interface, $\mathbf{k}_{\mathrm{x}}$ can match the plasmon dispersion curve of the air/metal interface and the coupling takes place.

The higher energy branch of the curve above ω_p in Fig. 2.5 is the radiative mode, called the Brewster mode, where the EM field is light. The lower part below ω_{SP} is the area where the EM field is a propagating plasmon. The Brewster mode is not a real plasmon because it is not really a true surface wave, according to the electron plasma model, due to the fact that the normal component of the wave is not purely imaginary [45].

Particle plasmons

In metal particles the excited plasmons are called localized surface plasmons (LSP) and they are confined to the surface of the structure. The plasmon resonance in a metal particle can be seen as a dipole oscillator which starts to follow the EM field. The shape and size of the metal particle have a strong influence on the wavelength of the plasmon resonance which results a color change in a nanoparticle solution.

If metal nanoparticles are considered as spheres, the internal and scattered field can be expanded into spherical vector wave functions (Mie theory) [46]. The field amplitude follows the field of a dipole and is proportional to r^{-3} close to the surface of the

sphere. When the distance is greater than the wavelength of light, the field strength is proportional to r^{-1}.

Using a quasi-static approximation [47], the polarizability α_i of the metal nanoparticle in the direction of an *i*-axis of an ellipsoid can be expressed as

$$\alpha_i = \frac{4\pi}{3} abc \frac{\varepsilon_m - \varepsilon_e}{\varepsilon_e + A_i(\varepsilon_m - \varepsilon_e)} \tag{2.24}$$

where ε_m and ε_e are the permittivities of the metal and the environment, A_i is the shape or depolarization constant, and a, b and c are the half axes of the ellipsoid.

From the Eq. 2.24 we can see that the plasmon resonance in NP depends on the environment, which also means that the plasmon resonance wavelength is different in air and in liquid. A higher index of refraction of the environment leads to a red-shift of the NP plasmon resonance. This can be exploited, for example, if the wavelength of the laser used in the measurements needs to be tuned to the resonance wavelength.

The resonance condition of the nanoparticle is full-filled when the denominator of the 2.24, $|\varepsilon_e + A_i(\varepsilon_m - \varepsilon_e)|$, is minimized. In the case of sphere ($\alpha_i = \frac{1}{3}$) this takes place when the real part is $\varepsilon_m = -2\varepsilon_e$.

In metal NPs, resonances are damped in different ways; radiation damping, energetic relaxation and pure dephasing. Radiation damping refers to re-radiation of the EM fields when the oscillating charge distribution radiates energy out from the NP. Energetic relaxation imply ohmic losses in the metal. Also the excitation of electron-hole pairs causes energetic relaxation when they decay by they own scattering mechanisms. Pure dephasing is the elastic scattering of SPs themselves causes dephasing of oscillation with the exciting the EM field. The dephasing means that the phase difference between the SP and exciting field/scattered field starts gradually to grow and eventually they cancel each other. The dephasing can be caused by scattering on surfaces or by simple decay of the collective mode due to inhomogeneous phase velocities caused by the spread of the excitation energy or local inhomogeneity of the nanoparticles [48].

When an extinction spectrum is measured from a metal NP solution or array, polarization can be used to investigate the shape of the NPs. If the shape of the NP is spherical, polarization will not have an effect on measured spectra. If the NPs are elliptical the plasmon resonance is blue-shifted when the polarization is along the short ellipsoid axis and red-shifted when the polarization is along the long ellipsoid axis.

When the metal NPs are very close to each other, the near-fields of the excited plasmon resonances can overlap and interference patterns are observed in the near-field scans [49]. When the separation of NPs increases enough, the modes will not overlap. Then a single NP can be considered as a single dipole and their collective radiation can be seen as a fringes of the far-field. Also sub-wavelength periodicity helps to avoid diffraction, which can lead to energy losses in extinction measurements and complicate the interpretation of the results.

Nanoantennas Elongated rod-like NPs can work as plasmonic nanoantennas (NA). In practice they are similar to radio antennas but the radiation of the nanoantenna is at visible or near-infrared regime [50] and the plasmon resonance is the source of the radiation. A nanoantenna can be, for example, a rod-like or a bowtie-like dimer antenna [51]. In the bowtie nanoantennas a strong local field is created between the sharp edges of triangular metal nanostructures.

NPs work well as nanoantennas because their extinction cross-section is very large, even larger than their actual size. At the plasmon resonance the absorption is the most efficient. The resonances can also be sharp, which improves the efficiency of the nanoantenna. This combined with efficient field-localization capabilities make them very interesting for investigating nonlinear properties, such as two-photon excitation [52].

In nanoantennas an interesting phenomenon is Fano resonance. It is an asymmetric resonance which arises from the coupling of dark and bright plasmon modes [53]. Bright modes in NPs are strongly radiative dipolar particle plasmon modes. In large metal structures there are also multipole resonances, dark modes, which do not radiate effectively. When these two kinds of modes couple, an asymmetric resonance is observed [54], called a Fano resonance after Ugo Fano [55]. Fano resonances are extremely sensitive to changes in the environment, which makes them very interesting in biological sensing applications.

An interesting aspect of plasmonic nanoantennas for this thesis is the lightning rod effect [45, 56]. It is the same everyday phenomenon that makes lightning strike in elevated metallic structures during thunderstorms, and it can be used to protect buildings and electrical equipment. Because of the geometry, charges tend to accumulate to the

tips or sharp corners. The increased surface density of charges at a geometrical singularity causes high and very confined EM field localization. Coupling from the incident light to the localized EM field is strongest when the beam is polarized parallel to the tip axis and hits the plasmon resonance of the metal NP, although coupling is very strong also out of resonance. Experimental results related to the lightning-rod effect will be described in Section 5.1.1 when the results of second-harmonic generation (SHG) in nanocones are discussed.

2.2.3 Nonlinear optics

Nonlinear optics deals with higher order responses of light-matter interaction, which become relevant when the intensity of light is high, i.e. the optical response depends on the field strength. In every day life this is rarely observed but with lasers this is a very ordinary phenomenon. A common application of nonlinear optics is imaging. Third-harmonic generation (THG) microscopy can be applied to image biological tissues [57].

Plasmonics is connected to the nonlinear optics by the fact that strong fields can be locally produced by the plasmons and a strong nonlinear response is achieved. Metal surfaces also possess intrinsic nonlinear properties and they can be further enhanced using plasmonics [58].

Another important issue is sensitivity. Surface plasmons create strong fields and the properties of plasmons are very sensitive to changes in the index of refraction. High local fields alter these parameters nonlinearly and change the resonances in the structure. This can be utilized in sensor applications.

The polarization of the material can be written as a power series

$$\mathbf{P} = \varepsilon_0[\chi^{(1)}\mathbf{E} + \chi^{(2)}\mathbf{E}^2 + \chi^{(3)}\mathbf{E}^3 + \ldots] \tag{2.25}$$

where $\chi^{(2)}$ and $\chi^{(3)}$ are second- and third-order harmonic nonlinear susceptibilities.

Second-harmonic generation

$\chi^{(n)}$ component is the *n*th order harmonic component of the nonlinear response and its components related to that term give rise to different nonlinear phenomena. $\chi^{(n)}$ is a

tensor and nonlinear optics is more or less studying the components of this very complex matrix. Symmetry rules can be applied to eliminate some components and simplify the structure of the tensor [59]. In practice this can be done with metallic nanoparticles in arrays where the shape of the patterns breaks the symmetry of the pattern array. This can be made with, for example, with L-shaped structures or other asymmetric nanopatterns.

$\chi^{(2)}$ is the first nonlinear component in the optical response. The most common second order phenomenon is the frequency doubling of light. It was first observed by Franken et al. 1961 [60] and it can be seen as a repercussion of the demonstration of the laser [61]. In this process two photons with frequency ω are combined into one 2ω photon in sum-frequency generation (SFG) in a nonlinear crystal with a high power laser. This has been a common method to produce green laser light from the near-infrared region because there has been a lack of lasing materials at the green wavelengths [62]. Difference-frequency generation (DFG) can be used to create longer wavelengths [63].

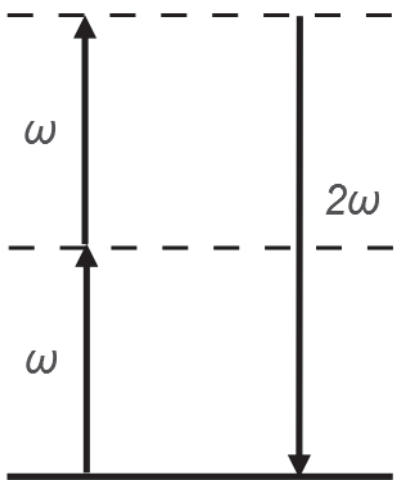

Figure 2.6: *A schematic for the second-harmonic generation. The black line is the ground state and the dashed lines are virtual states.*

In this thesis SHG presented itself as emission from the hot spots at the tips of the nanocones. As mentioned in Section 2.2.2, nanocones can support the lightning-rod effect and concentrate high local fields which are important for SHG. Since SHG is a very sensitive process for local field changes, it can be used in sensing. Bautista et al. [64] used SHG in scanning a nanocone array fabricated by the author to evaluate the quality of the structures.

2.2.4 Raman scattering

Raman scattering was found experimentally by a group lead by C. V. Raman collaborating with K. S. Krishan [65] in 1928. Raman scattering takes place when a photon is absorbed and emitted but a small fraction of the scattered light has a lower (or higher)

energy than the original photon, i.e. the scattering is inelastic. This energy goes to the vibration or rotation modes of the chemical bonds of the molecules. Every molecule has different vibration modes, which creates a unique fingerprint for every molecule, enabling their identification.

If the scattered photon has less energy than incident, scattering is called Stokes scattering [66]. The incoming photon loses energy to the vibration or rotation modes of the molecules. If a vibration mode is de-excited and gives energy to a scattered photon, the process is called anti-Stokes scattering. Compared with normal fluorescence, Raman scattering is a much weaker process and anti-Stokes scattering is the weakest of them.

Raman scattering is not in general a resonant effect, i.e. it does not need specific frequency to happen. Morover, Raman peaks have a constant separation from the excitation peaks. This is caused by specific rotation and vibration energies. Raman scattering scales linearly with the intensity of the incoming excitation beam, so powerful lasers help to detect the Raman peaks. There is, however, a problem with powerful lasers and biological samples; too much power damages them, especially in the green wavelength range. One advantage of the nanocones presented in P4 is the fact that a longer wavelength and less power can be used which means that the measurement is more gentle for the sample molecules.

After the invention of the laser, Raman scattering has become a widely used tool for chemists to identify chemical molecules. Raman peaks are very well documented and their daily use is relatively straightforward. An especially interesting and important practical application is the identification of counterfeit of Scotch single malt whiskies using Raman scattering [67].

SERS

Surface enhanced Raman scattering (SERS) is currently one of the biggest application areas of plasmonics. It was noticed in 1977 that the Raman signal can be enhanced by using Ag surfaces [68,69]. This was very exciting at that time because enhancing Raman signal even more than 10^{10} times meant that extremely small concentrations could be detected [70]. Even single molecules can now be measured [71].

Plasmons in metals can be used to produce very high local fields in the nanoscale.

This tight localization of light is one important key of SERS. Traditionally this enhancement has been done on a rough metal surface, typically on Ag or Au. According to Kerker [72], the EM field contribution to the total enhancement of the Raman signal R can be expressed as

$$R \propto \frac{|E_{\text{loc}}|^4}{|E_0|^4} \tag{2.26}$$

where E_{loc} is the localized EM field and E_0 the incoming EM field. This equation gives directly an answer to why SERS is so important for the applications of Raman.

There is also another enhancement mechanism called chemical enhancement. Chemical enhancement works by altering the adsorbate electronic states or creating new states upon adsorption [73]. In practice this mechanism works simultaneously with the field enhancement in SERS systems.

The lightning rod effect described in Section 2.2.2, is also contributing to the enhancement of the Raman signal [74]. This effect is a geometrical factor which is wavelength independent. For this reason sharp metal corners are beneficial for SERS.

TERS

In tip-enhanced Raman scattering (TERS) strong local-field are generated using sharp metal tips where the field concentrates similarly to the way charges concentrate to the corners of a metal cage. The development of TERS started in 1985 by Germin et al. [75] and it was further developed by Zenhausern et al. [76] and also Todd and Morris [77]. The first real demonstration of locally confined and enhanced Raman scattering were done in 2000 [78–80].

In practice, the nanocones presented in this thesis are TERS tips that can be used as probes or field-enhancers as in publication P4. The lightning rod effect plays important role in enhancing TERS in sharp metal tips, such as in the nanocones [81].

2.3 Simulation methods

In this section the simulation methods used in this work are presented in a level relevant to this thesis. These methods are used in analysing and designing of the applications.

Some practical issues related to these simulation methods are also presented.

2.3.1 Finite element method

Finite element method (FEM) was used to calculate the field distribution in a nanocone with a light beam (see Fig. 5.2b).

FEM is based on dividing the structure into smaller regions, i.e. an element grid, and solving differential equations (PDE) to get a solution using these elements and applying boundary conditions [82]. The solution is approximated by using piecewise polynomials.

For plasmonics and especially for nanocones and other sharp tips a problem of FEM is that near the sharp edges of metal structures the element grid must be very dense. In plasmonics every nanometer has a huge impact as the fields decay exponentially away from the surface/edge. If the overall structure is several hundreds of nanometers large the number of elements in the grid a very large and calculations are very heavy for a desktop computer. Therefore, effective use of FEM needs very powerful multicore computer with a large amount of memory or a cluster of computers.

The simulation in Fig. 5.2b) was carried out using axial symmetry to ease the simulation. With a conical structure it was possible to change the 3D problem to a 2D problem. Only one half of the cross-section of the nanocone is needed to simulate the structure successfully. It was observed that even a nanometer change in the radius of curvature increased hugely the electric field density in the tip. Also in that scale accurate measurement of the radius of curvature is very difficult and can be only approximated roughly, so these FEM simulations can only be used as guidelines on how the EM field behaves in the nanocones.

2.3.2 Fourier modal method

Fourier modal method (FMM), also called rigorous coupled-wave analysis (RCWA) or differential method, is used widely to solve nanophotonic problems [83, 84]. It is well-suited for periodic problems which are very common.

In FMM electric field $\mathbf{E}$, magnetic field $\mathbf{H}$, permittivity ε and magnetic permeability μ are expanded in Fourier series. A plane-wave expansion of the field is done before

and after the grating structure and in the grating a Bloch wave presentation of the field is used. Then the fields are matched at the interfaces and finally calculated in the whole system.

The FMM method was used to calculate and optimize the Ge grating structure presented in P3. FMM is an excellent tool for simulating this kind of grating structures.

2.3.3 Boundary element method

In P4 the boundary element method (BEM) [85], also known as the method of moments (MoM), was applied to solve the local field amplitude distribution in a bridged nanocone.

The basic idea of BEM is to use boundary conditions to fit the boundary values of an integral equation, which is a solution of the governing partial differential equation. This methods suits surfaces for which the Green's function [86] can be defined.

When the volume of the structure is small or the structure is non-periodic the BEM method can be more efficient than the FEM. A mesh grid is needed only on the surface of the simulated structure [87]. This is well-suited for plasmonics and nonlinear optics where phenomena happen on the surfaces and interfaces.

Chapter 3

Nanolithography methods

Nanoimprint lithography can be seen as a result of the technological development that started with Gutenberg's printing press. However, printing itself is a much older invention. The earliest surviving evidence of printing dates back to 2200 BC when the Sumerians in Mesopotamia used blocks for printing patterns on the surfaces of bricks [88]. An interesting detail related to this thesis is that there is evidence of printing in gold from the 6th century BC in the areas of Greek and Turkey. Naturally, these objects of art did not have anything to do with nanophotonics. However, these ideas have been developed further and reinvented to solve problems with a different scale and purpose.

Industrial lithography as we understand it today started to develop in the 1960s when the first microchips emerged. In those days, the features were measured in micrometers but they have since been replaced by nanometers.

In this chapter, the lithography methods used for realizing these nanostructures are presented in detail. The main focus is in ultraviolet nanoimprint lithography (UV-NIL) and its process flow, but also other methods are presented, since the fundamental nature of NIL is replication, instead of direct lithography. Therefore, NIL always needs other lithography techniques for master mold fabrication as discussed in Section 3.1.1.

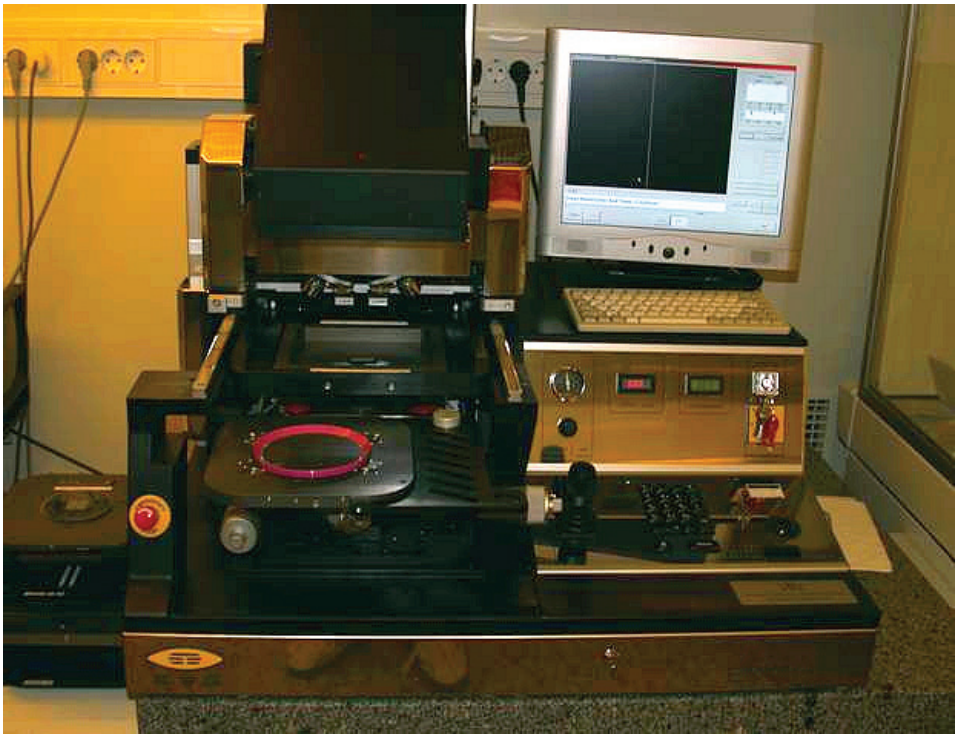

Figure 3.1: *The EVG620 lithography system which was used for NIL in this thesis.*

3.1 UV Nanoimprint lithography

NIL is fundamentally similar what we used to do in sandpits as children; forming patterns using preshaped molds. Instead of using plastic buckets, carefully designed stamps are used to transfer the desired nanoscale patterns into the resist and further onto the wafer. NIL can be divided into two branches: thermal NIL, which uses heat to harden the resist to the shape of the stamp, and UV-NIL, where UV-radiation is used to harden the polymer resist. NIL diverges by definition from nano- and microimprint, nanocasting and molding techniques. The purpose of NIL is to lithographically make patterns which are further transferred to the surface of the wafers, not to produce the final shape by itself.

NIL was introduced by Chou et al. in 1995 [4] and it was first applied to magnetic memory and transistor applications. The main advantage of NIL is that it can replicate nanoscale patterns in a fast and relatively cheap way. It can be adapted to nanophotonic

applications, such as distributed feedback lasers (DFB) [89,90], quantum dots arrays [91] and nanoperforated SiN membranes for optical and mechanical filtering [92].

The stamp can be either hard or soft, which has a large effect on the imprinting process. Hard stamps can be made of, for example, silicon, SiO_2 or nickel. A hard stamp does not bend or conform to the shape of a defect, which makes it adamant with dimensions but unforgiving to the cleanliness of the substrate. This means in practice that any particle between the substrate and the stamp can cause severe distortion of the patterns.

With soft stamps the polymer material is flexible and it can bend to accommodate external particles. The patterning fails locally but the overall imprint is of good quality.

3.1.1 Masters and stamps

Master molds for NIL are usually fabricated of silicon. Aluminum or silica can also be used but silicon wafers are preferable due to their processability, endurance and price. Especially in EBL silicon wafers are a natural choice because of their electrical conductivity, which makes the EBL step easier compared with non-conductive substrates, e.g. silica wafers.

The most important factor that favors Si wafers is the availability of well-controlled etching processes for silicon. NIL as a lithography technique can replicate extremely small features, but master fabrication in a reasonable scale is tedious and expensive. Very small trenches have been demonstrated using NIL but the size reduction has used a processing trick [93, 94].

LIL was used in this thesis to fabricate gratings and hole arrays. These masters were acquired from a commercial supplier when the wafer-scale pattern areas were needed. Because of its interference nature, periodicity in LIL is usually accurate over the wafer-area.

With EBL, pattern sizes are limited by the exposure time. This is a major problem with optical measurements. Usually transmission or reflectance measurements need at least 1 mm^2 patterned areas due to the beam size of the laser, especially for collimated beams. This is a limitation with commercial automatic measurement systems where the beam size is fixed and often quite large. However, EBL is still the best way to fabricate

complex and functional structures.

The stamp material has changed in ORC from soft-PDMS (s-PDMS) to hard-PDMS (h-PDMS) and finally to Ormostamp. At ORC was s-PDMS the first material used to produce patterns in a NIL process. But it soon became clear that it was not able to produce grating structures because of s-PDMS linepairing, which takes place when two grating lines collapse together [95]. In this case, h-PDMS was better if the aspect ratio was around one. Ormostamp is still one step further in hardness of the stamp material. It is a UV-cured material in contrast to h-PDMS which is thermally cured. This simplifies the fabrication of the stamp.

The masters are coated with perfluorodecyltrichlorosilane (FDTS) by vacuum evaporation to enhance antiadhesive properties, which is essential for h-PDMS stamps to be released from the silicon master. Also in prolonged use it helps to keep the master clean. Frequent cleaning in Panasolve (Dynasolve 211) is needed to remove PDMS remnants [96]. The current stamp configuration consists of a thick glass wafer, a PDMS mattress, and a thin glass wafer with an Ormostamp-based nanopatterned layer. This sandwich structure is flexible but the pattern layer is still hard. The PDMS mattress makes it flexible and the thin glass wafer prevents elongation of the thin Ormostamp layer. This kind of stamps are also durable compared with the old PDMS-based stamps.

The aspect ratio of the patterns is very important in the design of the master. The depth of the pattern should not be larger than the linewidth because usually an aspect ratio over one increases the risk of failure in imprinting. Especially h-PDMS has a tendency that the grating lines peel off if the aspect ratio is larger than one. The most usual case was that the resist was stuck to the stamp, peeling off from the substrate.

Another issue with the aspect ratio is the variation of the etching depth depending on the size of the etched structure, in other words aspect ratio dependent etching (ARDE) [97]. This leads to problems when the master consists of patterns with different linewidths. For example, with the structure in Fig. 3.2, the holes were etched deeper than the bridge which caused problems in the etching of the bias layer (as explained in detail in Section 3.1.2) since the bias was thicker in the bridge.

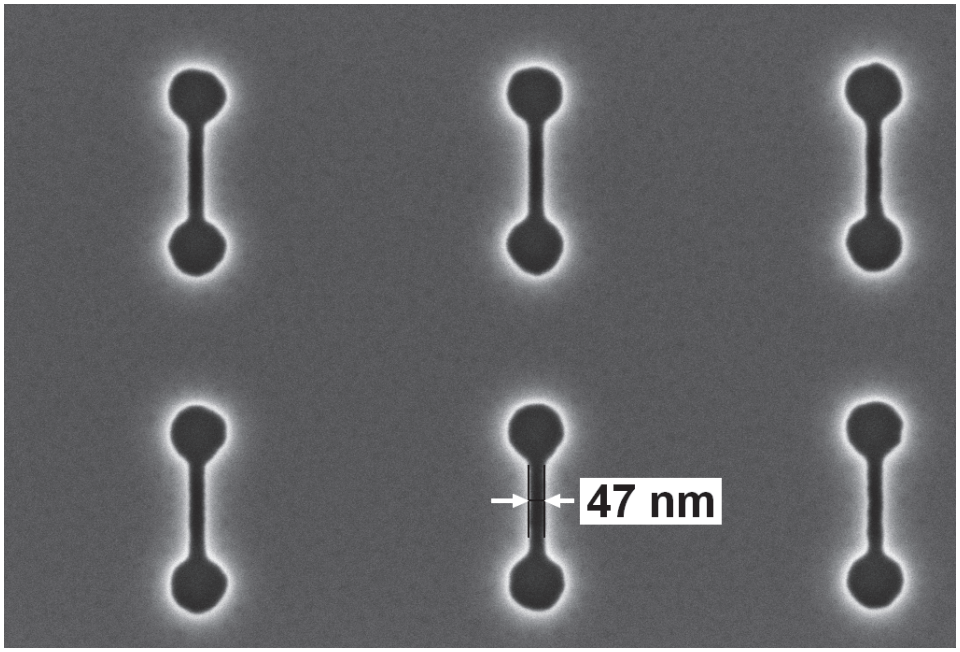

Figure 3.2: *A master mold with connected dots. This master was used to fabricate the bridged cones presented in P4. The main idea of this master was to form a shallow bridge between the two separate nanocones. The ridge part of the pattern is blocked up early during evaporation and a shallow bridge is formed. The depth of the patterns is 65 – 70 nm.*

3.1.2 Imprinting

An EVG620 mask aligner was used as the UV-NIL tool in this thesis (Fig. 3.1). It is an optical lithography system with a NIL tool option installed. The system uses an i-line (365 nm) halogen lamp for the exposure.

The UV-NIL system consists of a chuck that uses vacuum to attach the sample to the holder and a vacuum ring which is used to create and maintain vacuum conditions during imprinting. The stamp is attached to a stamp holder with vacuum and the stamp holder orientation is fine-tuned to compensate a possible wedge-shape of the stamp.

In the first step, the stamp and the sample are loaded into the holders. A rough alignment is done between the stamp and the sample by pins before the contact. The stamp and the sample are in close contact but still the sample can be aligned if needed.

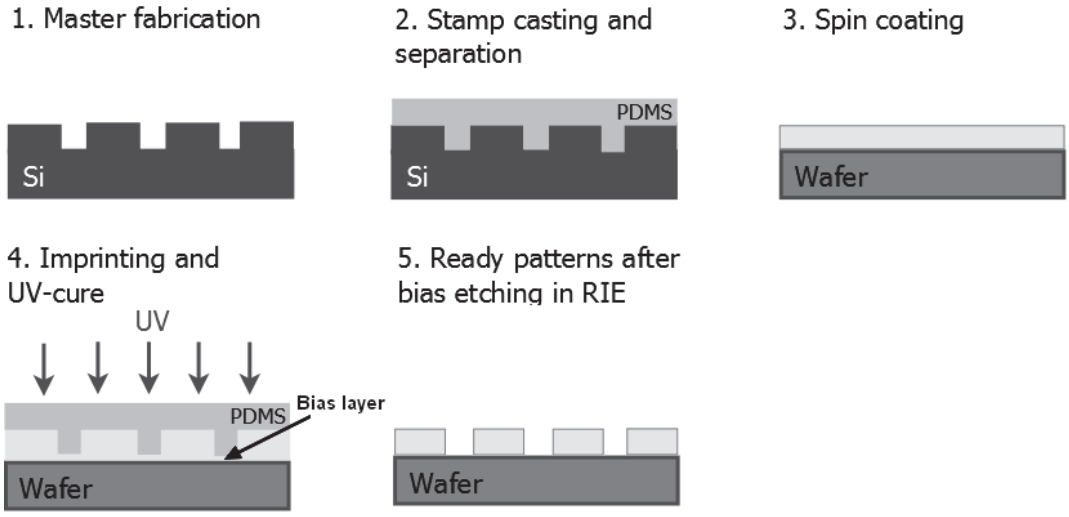

Figure 3.3: *The NIL process flow: 1. The master mold is fabricated using LIL or EBL on a Si wafer. 2. The stamp is fabricated by casting. The PDMS is hardened and peeled off from the master mold. 3. A NIL resist is dispensed over the wafer, usually by spin coating. 4. The stamp is pressed to the surface of the wafer, the resist fills the pattern in the stamp and UV exposure is used to harden the resist. Finally the stamp is peeled off. 5. The bias layer is removed by dry etching and the wafer is ready for further processing.*

Small vacuum is applied inside a vacuum ring seal which contains the sample and the stamp.

The vacuum is then adjusted to a desired pressure and the stamp and the sample are brought into contact (see Fig. 3.3-4). These steps need some delay because it takes some time for the resists to fill the patterns in the stamp. Then UV light is used for hardening the NIL resist. Three minutes with mr-UVCur and five minutes with Amonil resists are enough. Previously an additional UV exposure was used in an UV-oven to guarantee the hardening but it turned out to be redundant after the evolution of the overall process. The stamp and the master are detached by bending the edge of the sample gently until the stamp peels off from sample surface.

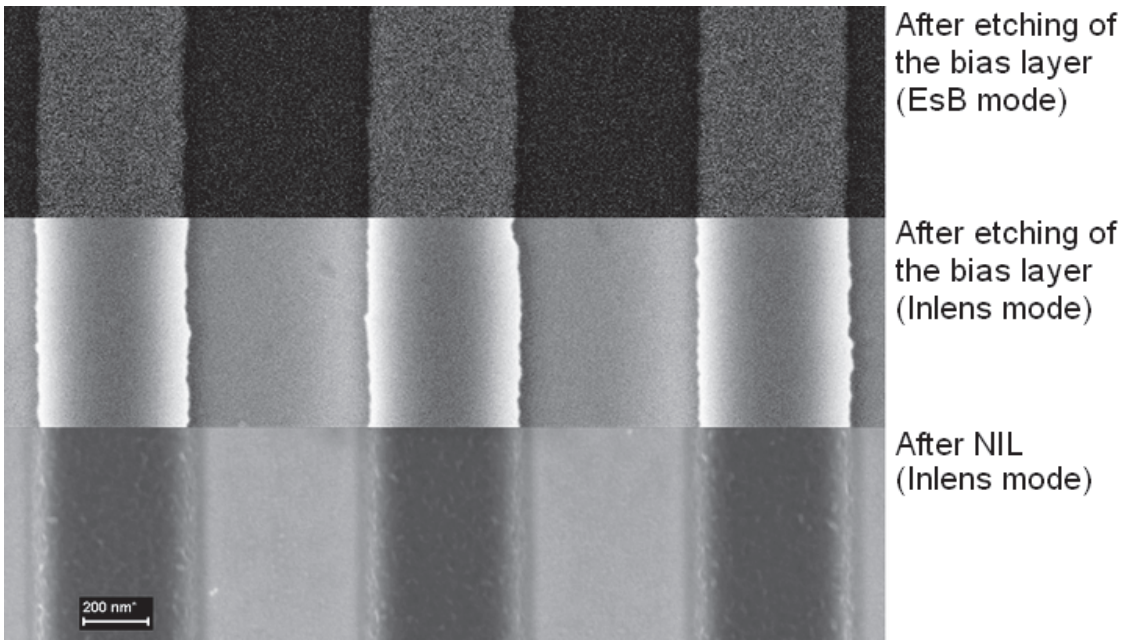

Figure 3.4: *A SEM micrograph of a nanoimprinted grating. The lowest picture presents the grating immediately after nanoimprinting. The bias layer is visible at the bottom of the grating as a rougher surface. The middle picture is after the bias etching with O_2 plasma. Fused silica wafer is exposed under the NIL resist and can be seen as a smoother surface. The two first pictures were taken with a secondary electron detector (Inlens). The topmost picture represents the same grating after the bias etching but with the EsB detector used in SEM imaging.*

Residual layer

The biggest problem of NIL is the residual layer, i.e bias layer, which is always left at the bottom of the imprinted pattern (see Fig. 3.3-4). After filling the pattern in the stamp, the extra resist remains between the stamp and the surface of the wafer. A low viscosity resist helps, but still the residual layer is always present in the imprinted structures. Usually, after optical or e-beam lithography the bottom of the pattern is clean after the development of the resist or only minor debris can be present and it can be usually removed easily with a few seconds of O_2 plasma.

The bias layer can be seen with a scanning electron microscope (SEM) or an atomic force microscope (AFM). Usually the bias layer and NIL resist at the top of the nanoim-

printed pattern are rougher than the substrate which can be seen in the middle and lowest part of the Fig. 3.4. The smooth bottom surface in a SEM image taken with the Inlens mode usually indicates that the bias layer has been fully etched. An energy and angle selective backscatter detector (EsB) can be used to enhance material contrast in the SEM imaging (see the topmost figure in Fig. 3.4). It makes easier to validate whether the bias layer has been fully etched from the bottom. Especially the partially etched bias layer can be seen easier with the EsB detector compared with the normal secondary electron mode. AFM can also be used to evaluate the thickness of the bias layer after etching provided that the original pattern depth is known. When the bias layer is fully etched down to the surface of the wafer, the pattern is also very smooth (roughness R_a is less than a nanometer) compared with the polymer surface. These methods can be used to estimate the success of the bias layer etching.

To tackle with the residual layer, the spin coated resist layer must be matched to the fill factor of the patterns to minimize the the thickness of the extra resist which forms the residual layer. The patterns in the master template must also be designed so that the variations in the fill factor are not too large. This would cause an inhomogeneous residual layer thickness which means in practice that thin residual layer areas will be overetched in the bias layer etching. This limits the complexity of the structures on the same wafer.

Sparse and dense patterns have different bias layer thicknesses which leads to the above described problems. This can be solved by inkjet coating of the resist unevenly depending on the fill factor like in Jet and Flash Lithography (J-FIL) [98] or by using "capacity-equalized" masters, which utilize constant averaged depth regardless of pattern density [99].

In the masters used in this thesis, the depths of the master templates varied locally based on linewidths of the structures, therefore broad grating lines were usually deeper than the narrow lines. This effect depends on the quality of the etch process of the master manufacturing. The residual layer was removed by anisotropic dry etching after NIL patterning, using a fluorine-based plasma for the Amonil resist and an O_2 plasma for the mr-UVCur resist.

3.1.3 Resists

Amonil resists (Amo GmbH) have traditionally been ORC's backbone of NIL resists. They are silicon hardened polymers which are quite etch resistant. For example, O_2 plasma does not etch Amonil which makes it challenging in the development of process recipes. In this case a fluorine-based etch chemistry can be used to etch the residual layer or a lift-off process to remove the etch mask layer. Wet chemical etchants or solvents cannot remove UV-hardened Amonil resist from the wafer.

Currently the NIL resist used in ORC is mr-UVCur [100] from Micro Resist Technology GmbH. It has lower viscosity and better etching properties than Amonil resists. This improves imprint quality and makes the process flow easier. Especially etchability with O_2 plasma makes mr-UVCur a much better resist for the processes. The resist can be removed with a short O_2 plasma process which does not harm dielectrics, metal or semiconductor surfaces. This helps to reduce etch remnants after the lithography step.

3.1.4 NIL and nanophotonics: practical aspects

Advantages

The main advantages of NIL are wavelength independence, fast replication of nanopatterns and repeatability. Diffraction is not a limiting factor of linewidth like in optical lithography[†]. The speed of NIL enables the fabrication of nanostructures in the industrial scale.

In the integrated circuit (IC) industry, size reduction has driven the manufactures to utilize costly stepper systems which can cost millions of euros. These systems are cost-effective only in large-volume mass production like in computer micro chips. A basic NIL system is relatively cheap and replication is very fast if the system is optimized for a standard processes in the production line. These aspects make NIL suitable for an industrial-scale production tool in small and medium-sized enterprises, for example in photonics.

[†]Although the linewidth of the optical lithography can be further reduced by using X-ray sources, there are no materials available which could be used as a lens or mirror for the X-rays. This limits X-ray lithography to a 1:1 shadow projection technique.

From the point of view of plasmonics and R&D, NIL offers a fast replication method even if one parameter, for example layer thickness, needs to be varied in a series of samples. The stamp accurately maintains the dimensions of the patterns between the samples if the process parameters are otherwise fixed.

The biggest benefit with NIL in an R&D environment can be achieved when it is used as a secondary lithography technique. For example, an EBL system is used to make prototypes and when the process is mature, NIL can be used for frequent lithography processes. In this case NIL can greatly reduce the workload of the EBL system. These features make NIL a strong candidate for next the generation lithography technique. NIL can also be developed further to reach molecular dimensions.

Disadvantages

Unfortunately, NIL also has many disadvantages. The biggest drawback is master fabrication. The development cycle is very long and time-consuming when the master molds have to be fabricated separately. The path from an idea to a fabricated prototype device becomes very long, even three or four months.

Usually in an R&D environment NIL's main advantages become irrelevant and unexploited, i.e. fast replication and repeatability, if there's no EBL tool available in the lab. Also NIL resists require extra processing steps compared to optical or e-beam lithography.

NIL usually needs a flat surface if the patterning is done on a wafer. Steps and holes in the wafer can cause an uneven resist thickness after spin coating, which results in a varying residual layer thickness over the wafer after imprinting. This could be avoided by adding an extra processing step: planarization. Also higher reliefs above an otherwise flat wafer surface have a thinner resist layer after spin coating and during imprint more force is directed to these higher areas, which results in the resist squeezing out of the stamp pattern.

One major problem in pattern design is the variable fill factor, since it determines the amount of resist needed to fill the patterns in the stamp. The extra resist forms the bias layer and quantifies its local thickness. The problem must be taken into account in master design by designing structures with as equal fill factor as possible. Nevertheless,

it is not always possible, which causes problems when different pattern areas have non-uniform bias layer thicknesses and some areas need more dry etching to remove the residual layer. This leads to over-etching of the mask layer and a failure of the process, which makes it difficult to test different kinds of patterns, such as dots and gratings, at the same time with a good pattern quality and yield. This can be avoided if a more advanced resist dispensing method than spin coating is applied.

NIL also has problems with sparsely located patterns, especially when the imprinted patterns are holes, i.e. the stamp contains pillars. A soft stamp material gets squeezed, the patterns widen and the imprinted patterns become shallower and misshaped (see Fig. 3.1.4). This problem was encountered in the fabrication of sparse nanocone samples for SHG scanning [64]. The used stamp material was h-PDMS because Ormostamp had some issues with filling the holes in the master. Holes in the used master had 50, 100 and 150 nm diameters and were organized in a square lattice with 8 periods between 500 nm – 10 µm. With the 500 nm period, the 100 and 150 nm diameter imprinted patterns were formed well but the diameter of the holes was expanded by about 50 nm. The patterns with the 50 nm diameter were not imprinted at all.

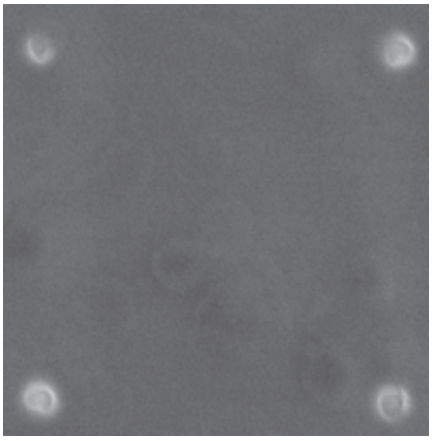

Figure 3.5: *Sparse holes patterns after NIL patterning. The period of the array is 2 µm. The shape has distorted and the diameter has widened.*

When the period of the lattice increased the imprint quality got worse. Especially, the shape of the hole started to deteriorate. With 5 and 10 µm periods hardly any imprinted patterns were visible. The reason for this was the squeezing of pillar patterns in the stamp. A harder stamp material, such as Ormostamp or other, could solve this problem. The problems with Ormostamp could be solved by using different anti-adhesion coatings. The used master was also a textbook example of the poor fill factor design because there were structures with the different diameters and periods at the same master, which we attempted to be fabricated at once. Therefore, focusing on patterns with a

single period at a time would be more a successful approach.

3.2 Electron beam lithography

Electron beam lithography (EBL), which was introduced in 1973 [101, 102], is based on exposing a resist, usually polymethylmethacrylate (PMMA), with a narrow beam of electrons which are accelerated using a high voltage. The exposed areas become soluble (or non-soluble) and are removed after treatment with a developer. The strengths of EBL are good resolution (<10 nm) and applicability to different scales. Its biggest drawback is the slow speed of patterning. Therefore it is mostly used in R&D and in mask fabrication for photolithography.

The diffraction limit is the ultimate limit to the resolution of the EBL, i.e. de Broglie's matter wavelength of the electron (5.4 pm at 50 kV), but in practice diffusion and scattering of the electrons in the resist are the limiting factors [103]. Moreover, electromagnetic interferences are a source of external noise in the electron beam, and they can arise from the electrical power network or from other devices located nearby the EBL system. It has been demonstrated in 2011 that a 9 nm pitch resolution can be achieved [104] and 3 nm gaps between patterns are possible to fabricate reliably [105].

Note that the sample must be conductive to allow the electrons to ground. If an insulating substrate is used, a thin layer of metal is needed on top of or under the EBL resist.

3.3 Laser interference lithography

Laser interference lithography (LIL) is based on the interference of two or more laser beams where the interference pattern exposes the resist on a wafer [106]. LIL is a very powerful and cost-efficient lithography technique in the fabrication of large area periodic structures, such as gratings or arrays of holes. Many nanophotonic structures and applications utilize this type of patterns.

On the other hand, the main disadvantage of LIL is the simplicity of the obtainable structures. More complex patterns need other lithography techniques which allow more

flexibility, such as EBL.

The minimum period is, at least in our vendor's system, limited to 180 nm. The limiting factor is the used wavelength of light. The theoretical limit for the periodicity of the pattern in LIL is $\lambda/2$ [107].

3.4 Other nanolithography methods

Many other nanolithography methods are available but they were not used in this thesis. However, it is worth presenting some methods that are used in practice or are promising for the future. These techniques belong to the International Technology Roadmap for Semiconductors (ITRS) which forecasts development of semiconductor technology, e.g. the linewidths in the integrated circuits (IC) [108].

A laser beam can be used as direct lithography tool. A focused beam is simply used to write patterns to resists similarly to an e-beam. In this method, diffraction is a limiting factor and the linewidths are limited by the used wavelength. However, this limitation can be overcome by a nonlinear process called multiphoton absorption. This allows 3D structures to be formed with sub-50 nm resolution [109].

Currently, immersion lithography dominates in the IC industry. The space between the resist and the lens is filled with liquid, usually water, to improve the numerical aperture. With this technique, 193 nm deep-UV systems have been extended to the 32 nm node [110].

One strong candidate to achieve the 22 nm node and beyond [111] is extreme ultraviolet lithography (EUV). These systems use 13.5 nm EUV light in the exposure. This technique is under development in major companies and is extremely expensive.

Multiple electron-beam lithography is a promising technique to fabricate patterns in the nanoscale. The basic idea is to use several hundreds or thousands of electron beams simultaneously in the exposure [112]. However, mass-production requires even millions of beams to be cost-effective in practice. This increases the complexity of the system and the price becomes unreachable for small and medium-sized enterprises. The potential is still vast and very active development is this field is going on [113].

Focused ion beam (FIB) is very popular in R&D because it is quite a handy tool for

making single or small arrays of nanopatterns or modifying the existing structures [114]. In FIB an ion beam (usually Ga, Ne or He) is used to sputter material from the surface with a resolution of $\sim$5 nm [115]. These systems are usually integrated with a SEM which enables in situ monitoring of the sputtering process. A major disadvantage of FIB is of course the time consumption with large pattern areas which limits its applicability in production, but it is still widely used in analysis, mask repair and sample preparation for transmission electron microscopes (TEM) .

Directed self-assembly is one of the most promising fields in nanolithography [116]. Its fundamental idea is to use molecular structures or polymers without an external controller guiding the direction of evolution. This can be achieved for example by crystallization on a surface forming desired patterns, or molecules attaching to certain points in a predefined structure. The main advantages of directed self-assembly are the possibility of large volume fabrication and speed. Controllability and stability are the main challenges, along with the complexity of the processes.

In scanning probe lithography (SPL) a surface is manipulated with a scanning stylus to form nanopatterns on it. This manipulation can be mechanical, e.g. scratching or nano intendation, chemical, heating or electric [117]. Although SPL can operate in the molecular level, it is still a relatively slow technique but the potential is high in atomic scale nanopatterning.

Chapter 4

Fabrication of photonic structures

In this chapter the fabrication of photonic structures by the lift-off process is discussed in general and in Chapter 4.3 the developed fabrication process of the conical metal nanostructures, which are an essential part of this thesis, is reviewed in detail.

4.1 Lift-off process

In this thesis the lift-off process was mainly used in the fabrication of metal patterns. It is very widely used in the industry and in R&D. Au nanopatterns were mainly fabricated by the lift-off process because wet etching and plasma sputtering of Au turned out to be difficult with NIL patterned surfaces. Wet etching of Au with a KI:I_2:H_2O solution is very fast, and it is hard to control the linewidth of the patterns due to the isotropic nature of the etching process. Plasma sputtering would be another option, but it is more damaging for the substrate than the lift-off process. Nevertheless, a plasma sputtering system was not available in our facilities.

The basic concept of lift-off is to create vertical or even negative side-wall profiles (see Fig. 4.1b) in a resist or other polymer which can be easily removed, for example, by solvent. These profiles can be achieved by an image reversal process or by using a negative resist in photolithography or by etching. In this thesis, dry etching by RIE was used to form the lift-off structures.

In NIL processes polymers are used as sacrificial layers under the NIL resist. Usu-

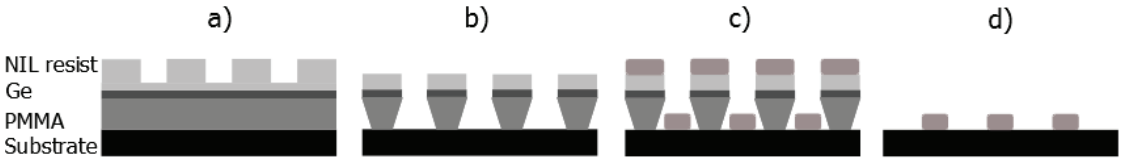

Figure 4.1: *A basic lift-off process flow: a) The lift-off-structure formed: spinning of the PMMA layer, evaporation of the Ge layer and finally NIL-patterning of the resist. b) Etching through the layers to form the lift-off structure. c) Evaporation of the metal. d) Lift-off in solvent to remove extra metal and the sacrificial layer. Only metal patterns left on the wafer.*

ally PMMA [118] or polydimethylglutarimide (PMGI) [119] is used as sacrificial layer. PMMA is commonly known as acrylic glass. It is important to check that the solvent used to dilute the NIL resist does not dissolve the underlying layer. This problem is usually avoided by adding a thin metal layer between the polymer and the resist. Germanium is widely used for this purpose. In addition, Ti, Ni, Cr and Al were tested but there were problems with graininess and difficulties in the etching process. Especially Al was found to produce deformed patterns after etching with $SiCl_4$. Overall the best performance was found with an intermediate layer made of Ge, which is very easy to etch with fluorine and chlorine-based chemistries.

In the beginning of my research a CHF_3:Ar:O_2 etch chemistry was used to etch through the Ge layer because a similar CHF_3:Ar based chemistry was used to etch the bias layer with the Amonil resist. This approach had an advantage of synergy since conditioning, i.e. driving the recipe in a RIE chamber before the actual etching of the sample, was not needed. The purpose of conditioning is to remove residual gases from the process chamber which affect the plasma chemistry and the etching results. Usually a 10 min conditioning is enough. With CHF_3:Ar:O_2 and CHF_3:Ar the plasma chemistries were similar enough and conditioning was not needed. However, after bias etching with CHF_3:Ar, chamber cleaning by O_2 plasma was still needed to remove the etch residuals.

A $SiCl_4$ based chemistry was also tested in etching Amonil bias and Ge layer. However, with a PMGI sacrificial layer it caused problems by forming a layer of unknown material on PMGI which did not etch properly with an O_2 plasma. A clear reason for this was not found but it must be related to the polymer forming due to $SiCl_4$ with other

etching residuals. Pure Cl_2 was not available at that time.

With the mr-UVCur resist, O_2 plasma was used in bias etching, which was a major improvement compared to the Amonil resist. O_2 plasma is milder for the chamber because it is frequently used to clean the chamber. Also the etched sample surface was very clean after the bias etch step. Moreover, the mr-UVCur resist is easy to remove from the wafer, which was difficult with the Amonil resist. CHF_3:Ar:O_2 was still used as a Ge etching gas until SF_6 was installed to our system.

A pure SF_6 based etching recipe was found to be very fast and clean for Ge etching in the lift-off process. A 5 s etch time was found to be enough for a 20 nm Ge layer. This combined with the mr-UVCur resist with O_2 plasma turned out to be a perfect combination for fast and reliable etching of the lift-off structure. It was also unforgiving because the edges of the patterns did not round during the etching. With a CHF_3:Ar based etching a small imperfection in, for example, the hole shape could be smoothed out by over-etching.

Etching through the sacrificial layer was done by O_2 plasma. The amount of undercut could be controlled by changing the RF power or the chamber pressure in the RIE. Especially in the nanocone fabrication process the amount of undercut becomes crucial. Too much undercut in deep PMMA or PMGI etching can collapse the whole structure. For these reasons 5 – 10 mTorr pressures were used in the lift-off etching with an RF power of 10 – 150 W in order to keep the wall profile vertical during the etching.

Development of the lift-off process

In this section a brief description of the developed lift-off process (see Fig. 4.1), which has evolved during the years is given. Although, it is carried out with NIL patterning, it can be easily applied to other patterning techniques.

In the beginning the substrate, which can be a Si, silica or other semiconductor wafer, is cleaned thoroughly with acetone, methanol and isopropanol using ultrasonic agitation followed by drying with a N_2 blow. Then a PMMA layer, which is at least 50% thicker than the planned metal layer, is spin coated over the wafer. Usually I have used a 100 nm PMMA layer for all metal layers thinner than 70 nm. The PMMA is baked on a hotplate at 170 °C for 90 seconds.

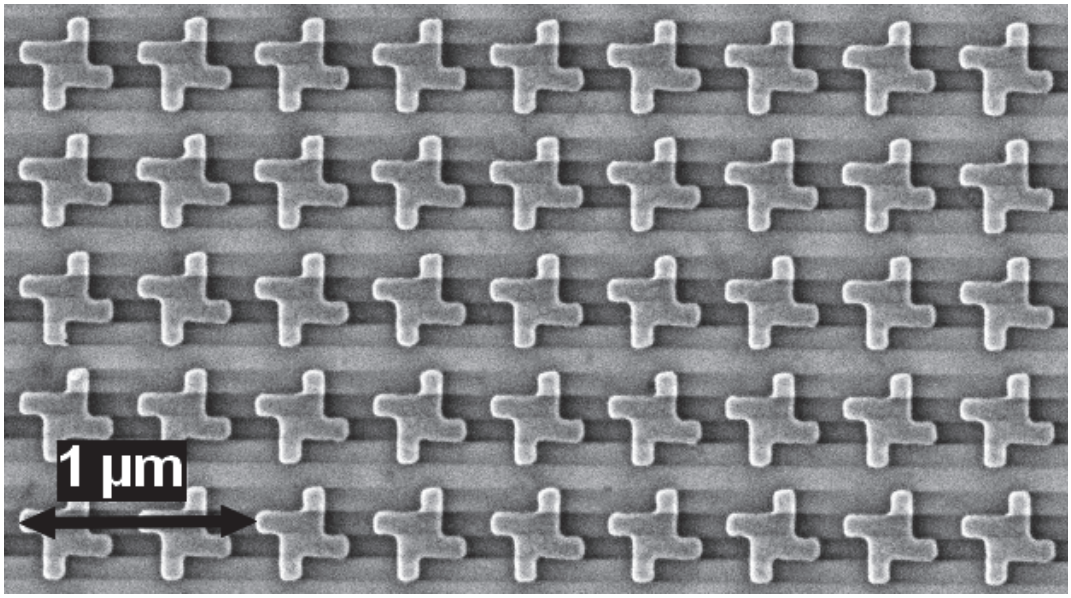

Figure 4.2: *Metallic propellers fabricated by the lift-off process.*

Next, a 10 – 20 nm thick Ge layer, serving as an etch-stop layer, was deposited by electron beam evaporation. This layer improves the controllability of the etching steps and prevents intermixing of the UV-NIL and PMMA resist layers. A thin layer of mr-UVCur resist was then spun over the Ge layer.

Nanoimprinting was carried out by an EVG 620 mask aligner using a stamp made of Ormostamp or h-PDMS. After inspecting the imprint quality with the SEM, reactive ion etching with O_2 plasma was used to etch through the NIL resist. The Ge layer was etched with 5 seconds of SF_6 plasma, and the PMMA layer was subsequently etched anisotropically with O_2 plasma, exposing the substrate.

In the next step, the adhesion layer and the metal layer were deposited by an e-beam evaporator. The metal layer over the PMMA was peeled off with UV-tape. Finally, the lift-off was done in an ultrasonic bath using the heated Microposit 1165 Remover for about 5 minutes. Now the metal patterns were ready on the wafer (see Fig. 4.2).

4.2 Germanium grating process

The fabrication process of a germanium guided-mode resonance mirror is based on etching the Ge using a NIL patterned resist layer as an etch mask.

We fabricated a 3×3 mm^2 GMR mirror with the parameters obtained from simulations. The GMR gratings were fabricated from e-beam evaporated amorphous Ge on a 1" fused silica wafer as a substrate. It was observed that the thick Ge layer laminated from the the fused silica wafer. To improve the adhesion, the substrate was coated with a 10 nm layer of silicon nitride (SiN_x) using plasma-enhanced chemical vapor deposition (PECVD). Immediately after this, a 550 nm thick Ge layer was deposited by electron beam evaporation. To guarantee the accuracy of the thickness of the Ge layer the growth rate was calibrated with a 100 nm test sample by maintaining the measured growth rate. Finally, a 70 nm SiNx etch mask layer was deposited by PECVD.

In the next step, 60 nm of NIL resist (mr-UVCur06) was spin-coated on the sample. The nanoimprinting of the grating pattern was performed with an EVG 620 mask aligner using a PDMS-stamp. Reactive ion etching (RIE) with O_2 plasma was then used to etch through the residual layer of the NIL resist on the bottom of the grating grooves. A mixture of CHF_3/Ar was used to etch through the SiNx mask layer. Prior to the etching of Ge the surface of the sample was cleaned using O_2 plasma to remove possible residuals left from the Freon etching. The Ge layer was then etched in ICP using $SiCl_4/Cl_2$/He chemistry and He backside cooling. The recipe was optimized to achieve a a vertical etch profile with smooth sidewalls. A low etching pressure with a moderate ICP power were the key points to success.

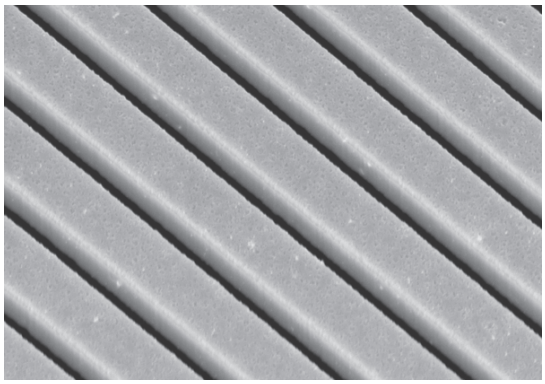

Figure 4.3: *A Ge grating. The period of the structure is 1 μm and the SEM image has been taken in a 34° tilting angle.*

After the fabrication process, a thin layer (about 35 nm) of residual SiN_x remained on top of the grating lines. It was not removed since in the simulations its effect was

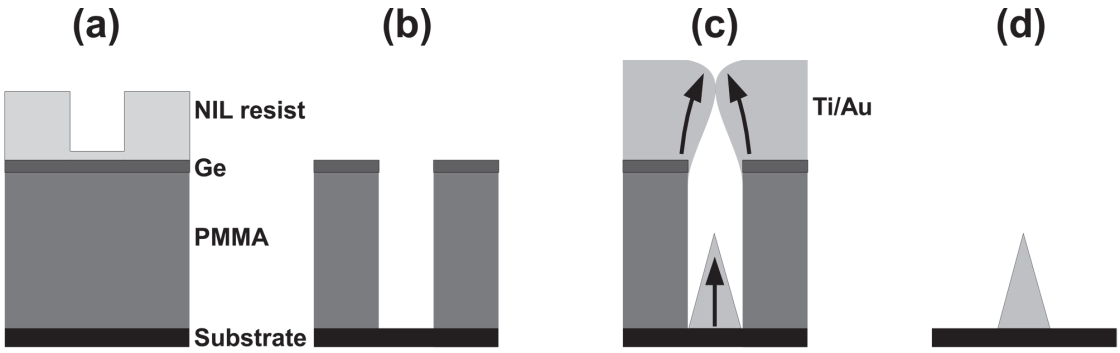

Figure 4.4: *A basic process flow for nanocone fabrication. a) Lift-off structure formed: spinning of the PMMA layer, evaporation of the Ge layer and finally NIL-patterning of the resist. b) Anisotropic etching through the layers to form the lift-off structure. c) Evaporation of the metal until the cone is formed. d) Lift-off in a solvent to remove the extra metal and the sacrificial layer. Only nanocones are left on the wafer.*

negligible and removal of the top SiN_x layer would have also damaged the adhesion layer. However, this SiN_x layer can be be removed by phosphoric acid if needed, as was done for the grating in Fig. 4.3. Also pure hot H_2O etches germanium. Therefore, in cleaning of the sample isopropanol (IPA) should be used instead of deionized water prior to drying with nitrogen blow.

4.3 Nanocone fabrication process

The nanocone fabrication process is one of the key results of this Thesis. In this section the basic concept and reasons which lead to cone formation are presented. The experimental results are later described in Chapter 5.1.

UV-NIL combined with e-beam evaporation can be used to fabricate large arrays of nanocones out of various metals. The method is relatively simple, low-cost, versatile, scalable, and it works on any flat surface with various metals. In the following section a brief description of developed nanocone process is represented.

We fabricated regular arrays of conical metal nanoparticles, i.e. nanocones, which usually have 90 – 200 nm base diameters and are organized in a square grid typically with a 180 nm – 1 µm period.

A master template having a 2D lattice of cylindrical holes was prepared by laser-interference lithography (LIL) or e-beam lithography on a silicon wafer. The nanopatterns on this master template were copied to a transparent elastomer stamp made of Ormostamp. A silicon, GaAs or silica substrate was spin-coated with a 600 nm layer of PMMA and baked on a hotplate at 170 °C for 90 seconds.

Next, a 20 nm thick Ge layer was deposited by electron beam evaporation. A thin layer of UV-NIL resist (mr-UVCur) was then spun over the Ge layer. Nanoimprinting was carried out by an EVG 620 mask aligner using the Ormostamp stamp. Following imprinting, reactive ion etching with O_2 plasma was utilized to etch through the NIL resist and the Ge layer was etched through with a brief SF_6 step, and the PMMA layer was subsequently etched anisotropically with O_2 plasma, exposing the substrate.

In the next step a metal (Ag, Al, Au, Cr, Ge, Ni, Pt and Ti available) layer was deposited by the e-beam evaporator. First, the 20 nm layer of Ti was evaporated to promote adhesion. During the Ti deposition, the pressure in the chamber was usually lowered to 10^{-8} mbar due to the residual gas gettering [120]. For all other metals the pressure remained at 10^{-7} mbar, except for Ni, for which the pressure was 10^{-5} mbar. The e-beam evaporator chamber was water-cooled during the evaporation and heated during venting to avoid moisture condensation on the chamber walls. The deposition was continued until the holes in the resist mask were completely filled with metal.

Then, using UV-tape attached with N_2 blow the metal layer was peeled-off from the substrate. Finally, a lift-off process was performed in hot a Microposit 1165 Remover bath using ultrasonic agitation. After this step we observed an array of metallic nanocones on the substrate (Fig. 5.1).

4.3.1 Nanocone formation

Nanocone formation is based on imperfect step coverage in the evaporation deposition [121]. With perfect step coverage the evaporated material forms a uniform film on every surface of the sample, including sidewalls. In thermal evaporation with an e-beam the material flux arrives on the sample surface perpendicularly. Ideally all evaporated molecules are unidirectional, but in practice there are small variations in the directions of the molecules.

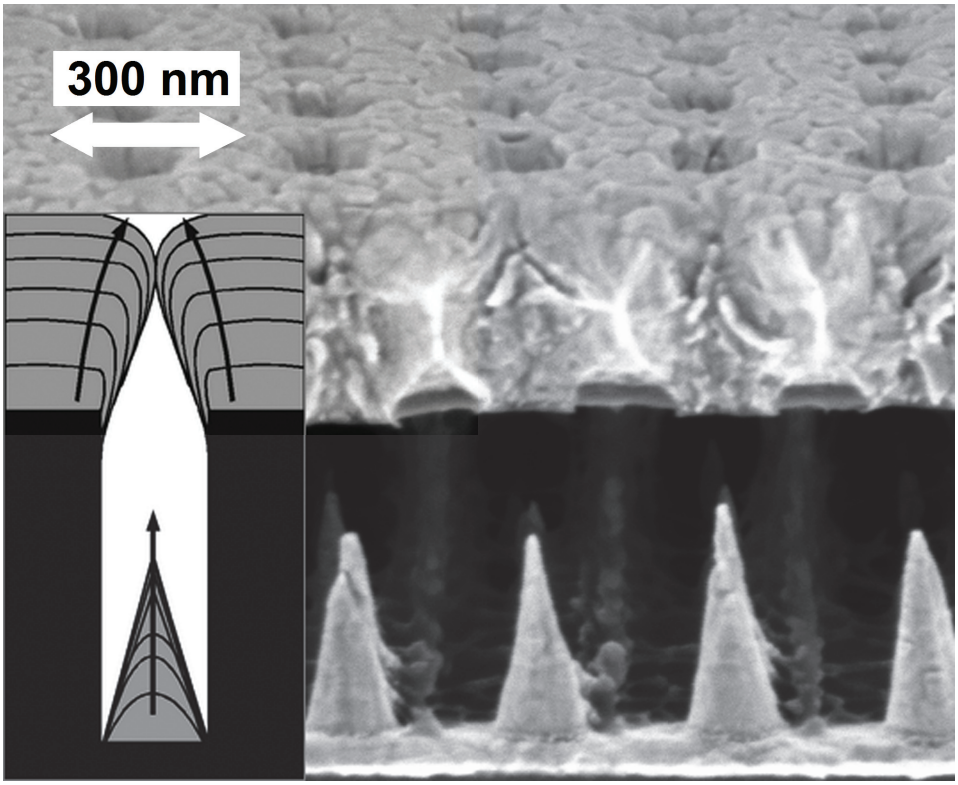

Figure 4.5: *The principle of the cone formation process. When metal is evaporated into a deep hole structure, the hole starts to shrink gradually and at the bottom of hole a conical metal shape starts to form. In the SEM picture a cross-section of the lift-off structure for nanocones is presented. The evaporated Au is on top and the darker material beneath is the PMMA layer.*

The process is the same in all lift-off processes but the main difference is in the aspect ratio of the etched hole (Fig. 4.4). When the depth of the etched hole is greater than the width, the hole can close even when the metal layer does not fill the pattern fully. Also the negative wall profile promotes this process. Otherwise the nanocone fabrication process is identical to a normal lift-off process.

The formation of nanocones takes place when the evaporated material starts to close the hole (see Fig. 4.5). As the upper end of the hole shrinks, a cone starts to form below. It starts to build up as a hemisphere-like metal dot but as the upper end of the hole closes a sharp tip begins to grow.

With metal atoms with a low sticking probability diffuse, reflect and resputter from the surface and result in a good step coverage of the film. With a higher sticking probability metal atoms attach to surface as they arrive and the deposited film grows more vertically [122]. Ideally with an infinite sticking probability the evaporation into holes would lead to the formation of the cylinder. However, with a finite sticking probability atoms will always diffuse and reflect to the sidewalls and conical shapes are formed unless diffusion is so strong that the atoms will always end up in the bottom of the trench.

The key points in the cone formation process are the directional metal vapor beam, the high-aspect ratio of a trench or a hole, and the properties of the evaporated materials. In an e-beam system the crucible, i.e. the source of the metal vapor, is located about 50 cm away from the sample, resulting in a directional vapor flux. This produces in a poor step coverage in normal samples, but in our case it is one of the features that enable the success of the process.

Since in an electron beam evaporator the sample is usually cooled with water flow, migration and thermally activated diffusion on surface are minor phenomena. Therefore, sticking probability is the main factor that determines the height of the cones. It gives rise to the hole shrinking that leads to cone formation. A low sticking probability produces short cones, as the metal particles are able to reflect and resputter, increasing the shrinkage of the hole diameter. Sticking probability can be tuned with temperature and it could possibly be utilized to tune the height of the nanocone, but in our e-beam evaporator there is no means to control the temperature of the sample holder.

4.3.2 Nanocones with various metals

After developing the nanocone process for Au, the next step was to test other metals. For this purpose in P2 a 4 cm^2 array with a lift-off mask was cut to several pieces to have a similar mask for all of the metals.

The conical shape of the nanocones was defined through the deposition of investigated metal layers on top of a titanium adhesion layer (10 nm). The same adhesion layer was used for each studied metal to ensure a comparable reference surface. The metals were Ti, Cr, Pt, Ni, Ge (a metalloid), Au, Ag, and Al. The evaporation rate was constant, 2.5 $\text{Å}/s$, and the pressure of the chamber after the evaporation of the Ti reference was

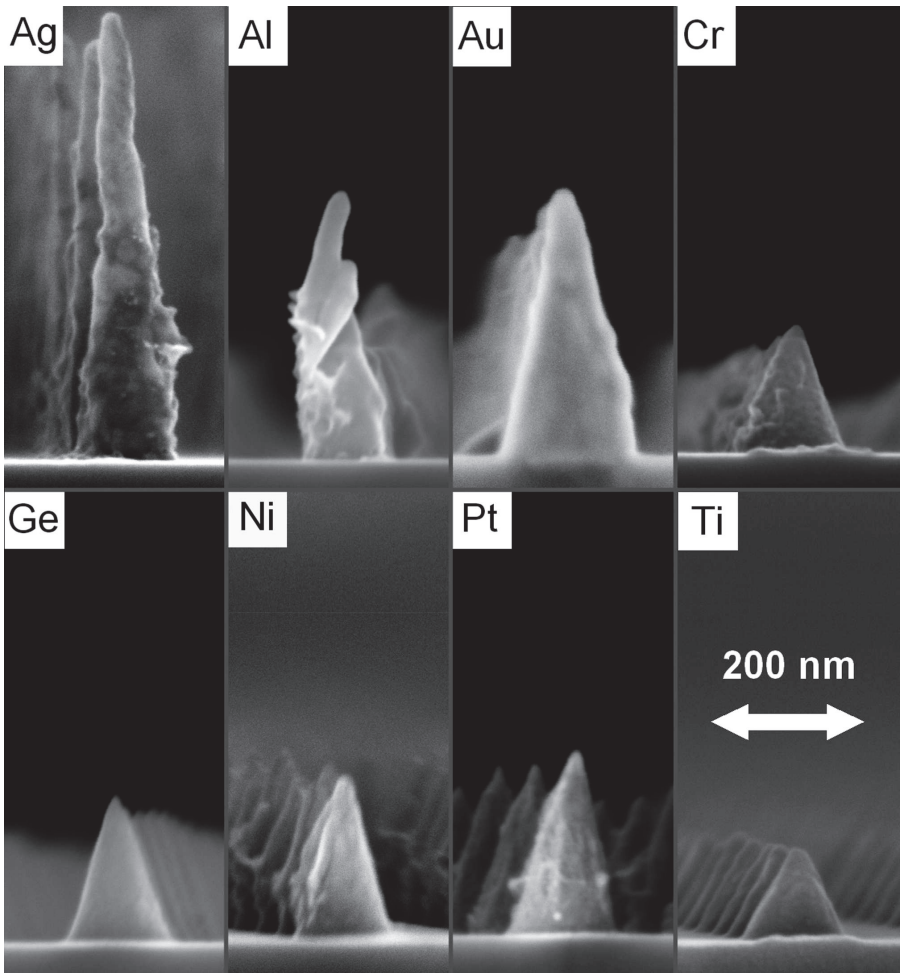

Figure 4.6: *The cone profiles of the nanocones fabricated with different metals. All the figures are in the same scale.*

about 10^{-8} mbar.

The shape and quality of the nanocones were investigated by an atomic force microscope (AFM) and a field-emission scanning electron microscope (FE-SEM) (Fig. 5.1). The dimensions and other parameters are shown in the Table 4.1. The yield of the nanocone process was approximately 95% over an area of 4 cm^2 which consisted of 4.4×10^9 nanocones. Fig. 4.6 shows the SEM micrographs of nanocones fabricated with eight different metals. It is obvious that the height and quality of the cones strongly depended on the material. Here the sticking probability plays a crucial role and it depends on temperature.

Metal	Evaporated	*h* nm (AFM)	*h* nm (SEM)	Aspect ratio	Hole status
Ag	1000	446 – 645	530 – 603	4.3	Open
Al	350	181 – 325	251 – 354	1.9	Open and closed
Au	400	295	281 – 335	2.4	Open
Cr	300	160	159 – 172	1.2	Closed
Ge	350	186 – 190	186 – 195	1.5	Closed
Ni	300	233	217 – 239	1.8	Closed
Pt	300	253	243 – 246	1.9	Closed
Ti	225	111	123 – 131	0.9	Closed

Table 4.1: *Characteristic dimension of the nanocones for different metals. SEM and AFM were used to define the heights. Hole status refers to the hole in the resist mask upon metal evaporation – an open hole means that depositing additional metal to the cone would have been possible.*

Comparison of the metals

The Au nanocones were reasonably high (aspect ratio ≈ 2.4) and their uniformity was good. Ag formed the highest nanocones (aspect ratio ≈ 4.3) but the height uniformity was the poorest of all the materials, due to grain formation which caused irregular shrinkage of the hole in the mask. This could be clearly seen after the evaporation of Ag when most of the etched holes were still open but the hole diameter varied substantially. Moreover, silver is soft, and the cones bent easily during processing, especially during the lift-off in the solvent using ultrasonic agitation. Even higher Ag nanocones could be fabricated, but the uniformity would decrease further.

Aluminum formed the largest grains, yielding polygonal holes instead of the desired round holes (see Fig. 4.7). Therefore, the Al cones were very non-uniform. Uniformity was also a problem with chromium but for a different reason. Cr formed small cones (aspect ratio ≈ 1.2) which were circular and symmetric, but the yield was poor because

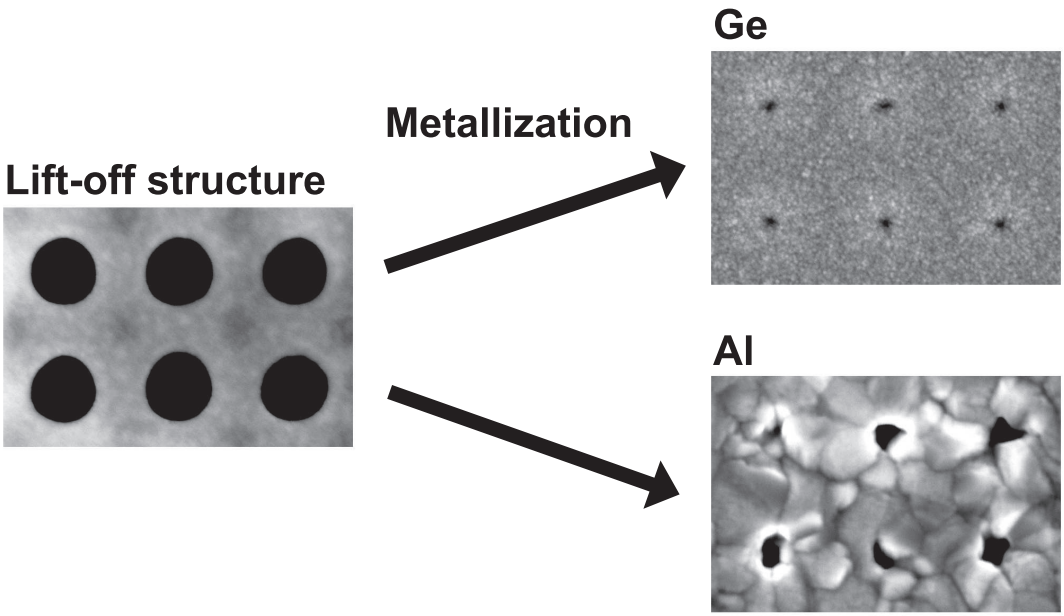

Figure 4.7: *A comparison of two materials to show how the material affects roughness of the evaporated metal layer in the lift-off process. Ge and Al were evaporated on top of the Ge etch stop layer. The strong grain formation caused the non-uniformity of the Al cones.*

the Cr layer peeled off and started to roll up on top of the resist mask during evaporation. The Cr layer was so strained after solidification that it ripped the intermediate germanium layer off the PMMA layer. This could be a serious problem in fabricating large arrays of Cr patterns.

The Ge cones were relatively low (aspect ratio ≈ 1.5) but the quality and the uniformity were the best of all the materials. Due to this the Ge nanocone array was later used as a master mold for the NIL stamp for making anti-reflection surfaces on semiconductors (see Chapter 5.1.3). Ge is a metalloid and an interesting material for the infrared spectral range, due to its very high refractive index ($n \approx 4.0$). Ge is neither transparent nor metallic in the visible band [123] but could be coated, for example by Au, to achieve high-quality metallic nanocones. Nickel also formed nanocones with reasonable uniformity.

Platinum created sharp cones of average height (aspect ratio ≈ 1.9). Platinum can be used in inert probe tips, an area where titanium cones can also be used. Ti formed

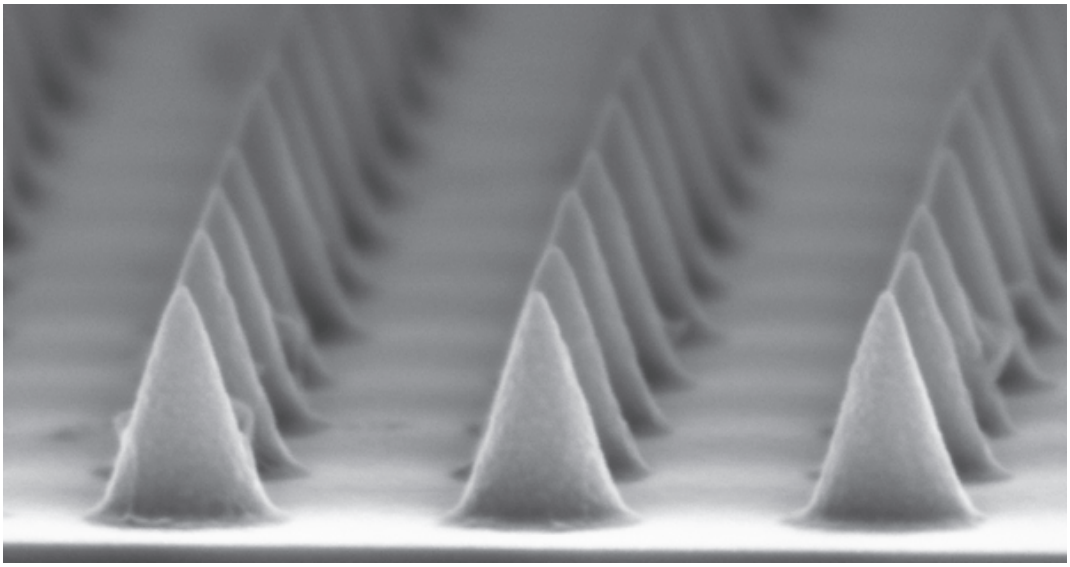

Figure 4.8: *Rows of Ge cones. The Ge cones were the smoothest of the tested materials. The uniformity was also the best which is caused by the small grain size after the metal evaporation (Fig. 4.7).*

the smallest cones, and being a very strong material might excel in applications where mechanical durability is an issue. Ti could also can be used to shrink the hole-size during the cone process to form "hat-like" cones with an intermediate Ti layer, for example, with Au.

Silver produced the tallest cones, with an aspect ratio of about 4.5 (see Table 4.1). However, silver cones were not eminently sharp, because the hole was not shut after the evaporation and the sharp tip was not formed.

Uniformity of the cones

The uniformity of the height of the cone was directly proportional to the grain size of the metal film after the evaporation. The grain size was characteristic of every material and is the main challenge for our method. Not only did grainy metals grow into irregularly shaped grainy cones, but also covered the holes non-uniformly, leading to wide variations in the height of the cones. Aluminum was a prime example of this effect (see Fig. 4.7).

The same problem was also observed for silver, but the circular shape of the cones

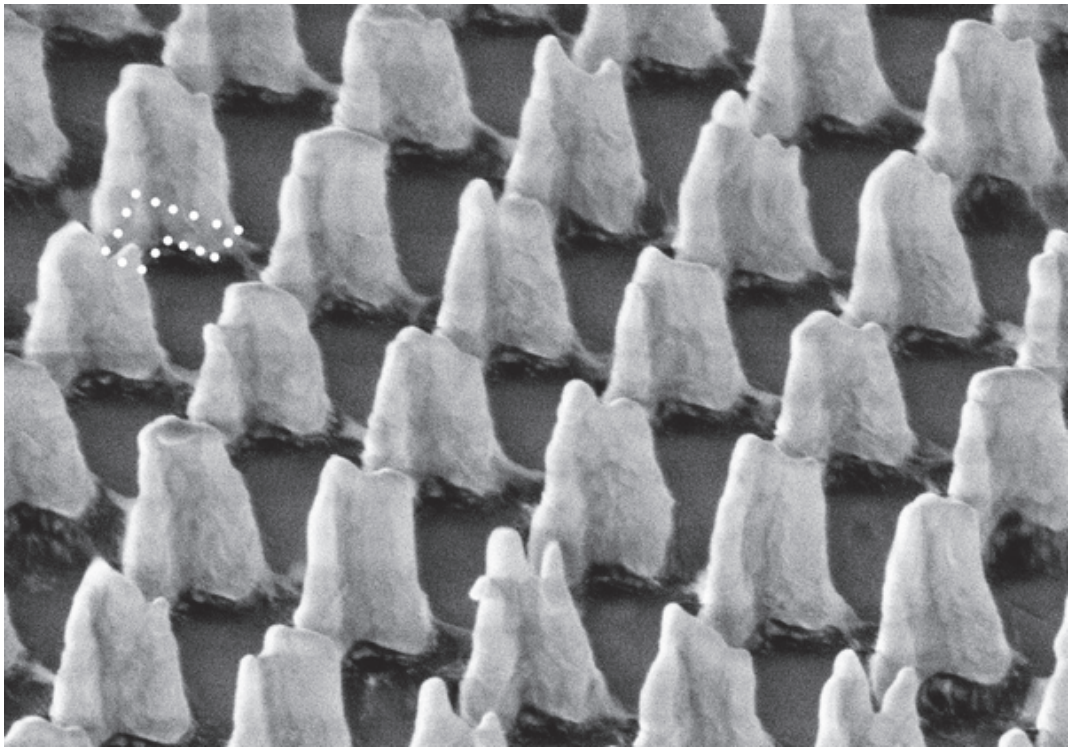

Figure 4.9: *An array of conical L-shaped metal structures. Initially, the patterns were L-shaped holes. Note that the tip of the cone is not one solid ridge. The L-shaped original pattern is roughly sketched at the basis of the conical structure at the left side. Imperfections in the patterns cause peaks to the wings of the "L".*

was less distorted. However, the high aspect ratio of the Ag cones caused considerable non-uniformity in cone heights. With germanium the grains were very small (see Fig. 4.7) resulting in uniform and symmetric nanocones (see Fig. 4.8). With chromium, the limiting factor for the uniformity was peeling off of the metal layer during the evaporation. In the SEM micrographs (not shown) the Cr layer was seen to peel off the Ge intermediate layer from the PMMA. The adhesion between Ge and PMMA was poor, as expected. The PMMA layer could be replaced by another, harder material to alleviate this problem.

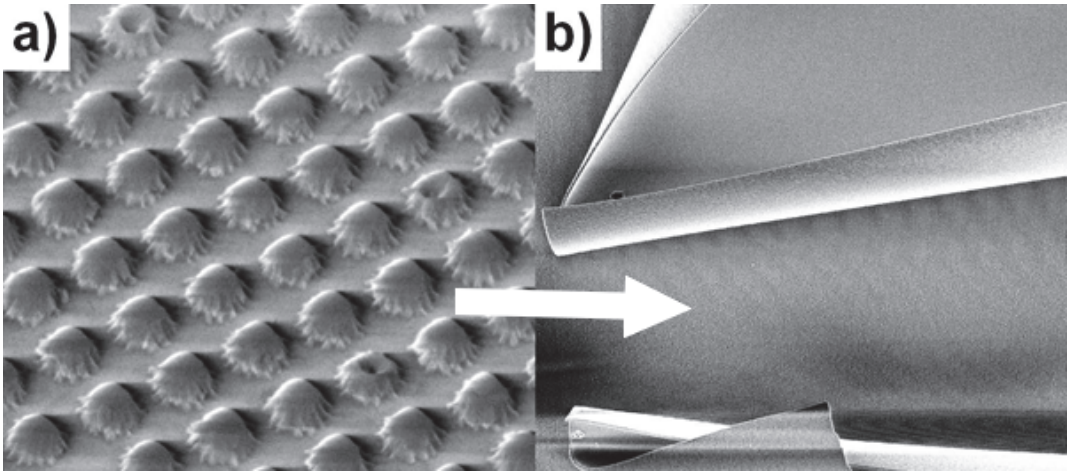

Figure 4.10: *Al_3O_2 cones. a) Al_3O_2 hemipherical semi-cones. b) A peeled off Al_3O_2 layer after evaporation. Strong stress causes rolling of the evaporated Al_3O_2 layer.*

Other structures using the nanocone process

With dielectric materials, such as Al_3O_2, our process did not produce nanocones, but formed structures that resembled hemispherical dots (see Fig. 4.10). In principle, any material that can be deposited by e-beam evaporation or other physical vapor deposition techniques may be used. Similar hemispherical Au dots can be also produced by evaporating less metal (lower inset in Fig. 5.4).

The final cone height and sharpness can be accurately controlled by the evaporation rate and time. It is possible to fabricate multi-layered cones, such as metal-insulator-metal (MIM) nanostructures (see Fig. 4.13), from any e-beam vaporizable materials. Also, nanocones with various height could be prepared at the same time if the patterned holes had different diameters. Large holes take more time to be covered, resulting in higher cones when compared with the holes with small diameters.

The base of the cone does not need to have a circular cross-section – any shape of a resist groove will grow into a structure with a sharp tip. For example, consider Fig. 4.9, which depicts patterns formed through an L-shaped hole. The ridges of the L-shaped structures have considerable variation of the ridge height along the arms of the L. This is a result of imperfections of the etched hole.

Summary of the nanocone process

The main advantages of our nanocone fabrication method are a result of using UV-NIL. After producing the initial master pattern, for example by expensive EBL, the pattern could be replicated hundreds of times cost-effectively. Moreover, the cones could be made of different metals or a combination of metals. By using UV-NIL, the arrays of nanocones can cover wafers as large as 6 inches [124] which are widely used in silicon industry. Our nanocone process is a rather gentle method to fabricate metal tips on the substrate compared with, for example, FIB etching [125]; the most damaging step is an O_2 plasma RIE etching step.

A disadvantage of our method compared to FIB is that the deposited metal structures are always grainy. However, in many applications, metal structures are in any case deposited directly onto a substrate, so that our cones will be of similar quality.

4.4 Dry etching

The pattern transfer in the nanocone process and nanophotonic device fabrication using NIL is based on dry etching. The residual layer (details in Section 3.1.2) must always be removed by anisotropic dry etching. The anisotropic nature of the etching process is a key element in linewidth control in order to replicate the master template as accurately as possible onto the sample substrate.

Wet etching is usually not an option in NIL because resists are insoluble in the most common solvents and the isotropic nature of etching makes the linewidth control more difficult. In this thesis mainly reactive ion etching (RIE, Oxford Plasmalab System 100) was used in the etching through the lift-off mask. Inductively coupled plasma (ICP, Oxford Plasmalab System 100) was used for etching the germanium GMR mirrors (2.2.3).

The selection between RIE and ICP is mainly determined by the etching gasses available in the system as well as cleanroom policies. Freon-based chemistries and polymer etchings are generally done in RIE, and semiconductor and chlorine-based etches in ICP in order to improve the repeatability and to avoid contamination.

Our lift-off etch process has developed during the years. In order to guarantee good etch selectivity in every step, a basic NIL resist/Ge/PMMA lift-off structure was used.

Etching the metalloid Ge was done by adding a small flow of O_2 into the fluorine plasma. This has two functions. First, O_2 consumes carbon, oxidizing it from the freon plasma and increasing an amount of fluorine radicals in the plasma [126] and it also prevents polymer formation in the freon etching. Second, the etching process of Ge oxide is a faster than the etch rate of the pure metalloid surface. This increases the overall etching rate.

It was observed that the Amonil and Ge etching steps were best done in a row without braking the vacuum in order to maintain repeatability of the process. Apparently the Ge surface oxidized in air and the Ge etching rate decreased. The main goal was to get good selectivity between the etch mask and the lift-off layers. With chlorine good selectivity was achieved between the Amonil and Ge in test etching with a dummy wafer but when the lift-off structure was applied, the PMGI layer became impenetrable. Chlorine and fluorine gases cause this kind of problems when used in the same process chamber, which has been known in the field for years.

After installing the SF_6 gas to the RIE system, it was possible to etch the Ge layer with pure fluorine. The freon based plasma always causes the formation of carbon-based polymers in the process chamber and the on the surfaces of the samples. With SF_6 the etch process was much cleaner and selectivity between the mr-UVCur resist and Ge was extremely good.

In the fabrication of GMR mirrors, ICP etching was applied. Vertical sidewalls were essential because parameter tolerances were quite narrow (see Fig. 5.2). With ICP, the properties of the plasma can be tuned. In RIE, the power and the plasma density go hand in hand but in ICP with a low RF a power high plasma density can be achieved. This helps when low pressure is needed, e.g. in etching deep holes into semiconductors, but a high etch rate is still desired.

In ORC's ICP system helium backside cooling can be applied to control the temperature of the sample which can improve selectivity and the etch profile and prevents resist burning during etching. In order to get a vertical etch profile, a $SiCl_4/Cl_2$/He based chemistry was used in the recipe. $SiCl_4$ is a very good etching gas when vertical sidewalls are needed because of sidewall passivation due to silicon-based polymers. A similar recipe has been used in etching high aspect ratio Ge zone plates [127].

The etch rate with this recipe turned out to be very high and the ICP power was lowered in order to improve controllability. The plasma had also stability issues in low pressures and the chamber pressure was increased until the plasma was stable. A low pressure strike was applied for igniting the plasma.

4.4.1 Linewidth control

Line width control is important for the accurate replication of the designed structure to a final working device. In critical applications line broadening due to NIL or etching must be taken into account in designing the master template.

The period of the patterns is usually almost constant in NIL processes but in extremely accurate applications such as in DFB diode lasers even variations of a few nanometer are too large [128]. The imprint process itself usually broadens the linewidth when the stamp gets compressed. This happens especially when the aspect ratio of the pattern is more than one. The etching step is the most crucial step in the linewidth control.

Sparse patterns also cause broadening as mentioned in section 3.1.4. This happens when the stamp material is not hard enough to keep its shape under pressure. This could also be taken into account in the master design if the broadening is tested beforehand with another master.

In the lift-off process the keypoint in linewidth control is the intermediate Ge layer. If it is etched properly then the etching of the sacrificial layer is quite straightforward. O_2 even with with longer etch times does not etch Ge and only ion sputtering consumes it. Usually sputtering in RIE etching consumes a few nanometers per minute with high RF powers.

4.4.2 Practical views

Over the years several handy tricks were found which helped to increase the yield, i.e. the number of the nanocones of good quality from the patterns in the stamp, in the lift-off process. One of the best ones was preventing the nanocones from falling with adhesive tape. Nanocones were fallen and bent after the lift-off process and it was observed

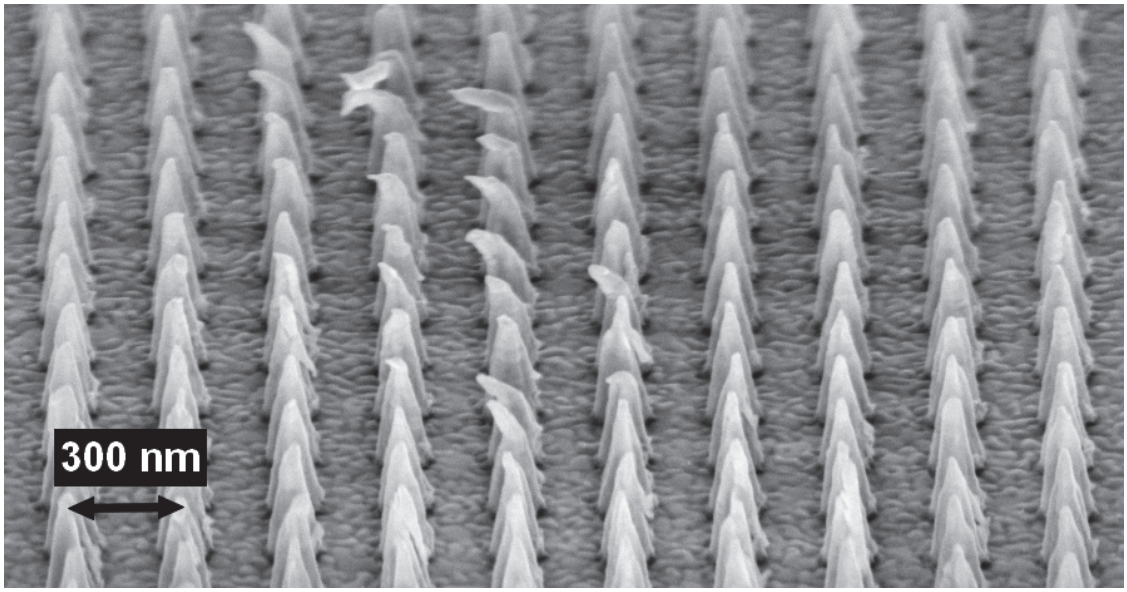

Figure 4.11: *A SEM micrograph of the fallen and twisted nanocones. In the lift-off metal flakes damage the nanocones mechanically. Tape assisted lift-off was used to tackle this problem.*

that pieces of metal flakes during the ultrasonic agitation in the solvent bombarded the nanocones and twisted them mechanically (see Fig. 4.11).

This problem was solved by attaching a tape used with wafer scribers to the metalized sample surface and peeling of the evaporized metal layer before the lift-off in the solvent. An UV-detachable tape was found to be the best for this purpose. With this procedure the metal layer could be reproducibly removed from the top of the polymer. Naturally this does not work when the metal is directly on top of the hard sample surface. The most gentle way to attach a tape to surface of the sample was by a N_2 blow, which also removed the bubbles from under the tape efficiently.

Usually heated solvents work better in the lift-off, but heating also helps to crack the top metal layer to allow the solvents to penetrate the sacrificial layer. However, heating of acetone is not recommended because of the low flash point (-20 °C) of acetone vapors. The boiling point is also low (56 °C) [129]. With PMMA and PMGI, Shipleys's Microposit 1165 Remover [130] was used. Due to different thermal expansion, the metal film laminates from the surface of the polymer and speeds up the lift-off process.

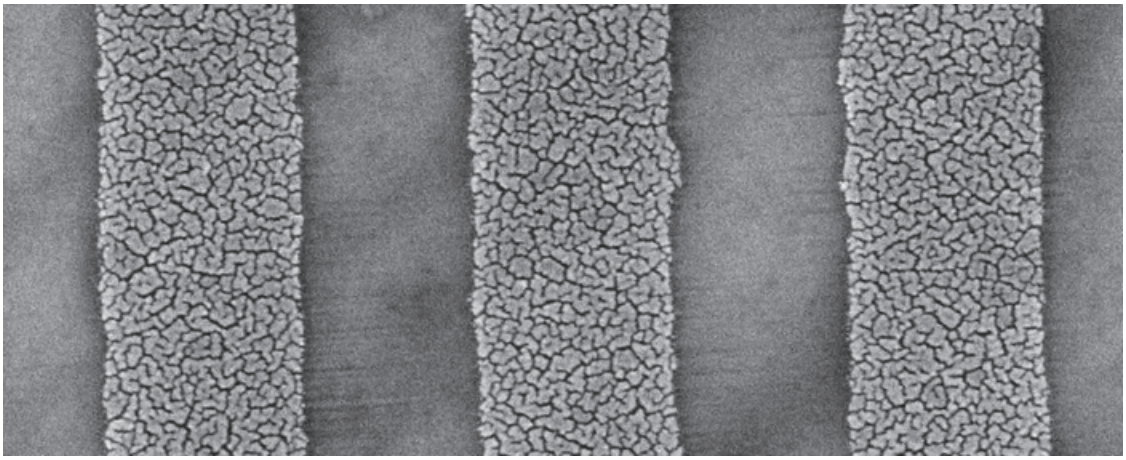

Figure 4.12: *5 nm of Au without an adhesion layer. Below 8 nm film thickness Au layers started to become grainy.*

Ultrasound was used frequently in the lift-off. It makes the lift-off faster and in many cases a good yield is impossible without an ultrasonic agitation if the metal layer does not crack. It also helps to remove the unsolvable etch residuals from the surface. It is recommended that the solvent, if possible, is pre-heated before immersion of the sample to the ultrasonic bath.

A CO_2 snow gun can be used to remove extra metal from the sample. However, rapid cooling and hard mechanical stress can also detach the delicate nanostructures from the wafer. A CO_2 snow gun can not be recommended for everyday lift-off, but only as a last means of recovery before acknowledging the failure.

Au nanopatterns usually need some adhesion layer between them and fused silica, although they can also be produced without it. In this thesis titanium was mainly used as an adhesion layer. It has some influence in plasmonics as the plasmon resonance wavelength and losses depend on the used materials in the nanostructure. According to Aouani et al. [131] TiO_2 and Cr_2O_3 would be the best choices in terms of fluorescence enhancement with molecules. The adhesion layer also causes absorption. At ORC, metals and dielectrics are deposited with two separate e-beam evaporators, so dielectric adhesion layers can not be fabricated without braking the vacuum. Therefore, Ti was used as an adhesion layer.

Since Ti is a bad material for plasmonics the adhesion layer was kept as thin as

possible. With gratings and dots thinner than 100 nm, 3 – 10 nm of Ti is enough. In the nanocone process a 20 nm of adhesion layer was found to be sufficient. With a deep lift-off structure used in the nanocone process less metal was deposited on the bottom of the hole and a thin adhesion layer was not adequate. Also more metal is deposited to the center of the hole causing the Ti adhesion layer to become hemispherical (see Chapter 4.3.1).

There's also another method to improve the adhesion. Before the metallization, a monolayer of 3-mercaptopropyltrimethoxysilane (MPTMS) can be vaporized on the surface of the wafer [132]. This was tested and found to work very well in wafer scale. The Au layer fabricated on top of the MPTMS passed the standard "Scotch tape test", which is widely used in the R&D laboratories to evaluate the adhesion properties of films after evaporation.

The MPTMS treatment was also applied to the lift-off process with poorer results. The MPTMS deposition was done after the O_2 plasma etching of PMMA. After about 3 hours of vacuum evaporation of MPTMS the Au patterns were quite poorly attached to the wafer. However, in a recent paper by Habteyes et al. a similar procedure was applied successfully [133]. They used a much longer evaporation time of 3 h – 3 days. The long idle time limits the practical processing and for everyday fabrication this is quite a poor option.

An adhesion layer is not mandatory with Au nanostructures if the mechanical endurance is not the main goal. We tested the tuning of the plasmon resonance with very thin Au gratings. The plasmon resonance shifts to longer wavelengths when the grating lines get thinner. For these tests no adhesion metal was applied to get a stronger optical response. For 8 – 50 nm thickness the Au gratings endured the lift-off process if ultrasound agitation was not applied. The structures were strong enough to be measured in the laboratory. A problem was only that Au layers thinner than 8 nm were not smooth films but grainy after the Au evaporation (see Fig. 4.12).

Also sandwiched metal-insulator-metal (MIM) structures [134] can be fabricated without an adhesion layer at the metal-dielectric interface (Fig. 4.13). We tested this by fabricating similar samples which consisted of Ti/Au/ZrO_2/Au 1/10/5/10 nm layers. Au and ZrO_2 layers were deposited by e-beam but in a different system, i.e. the vacuum

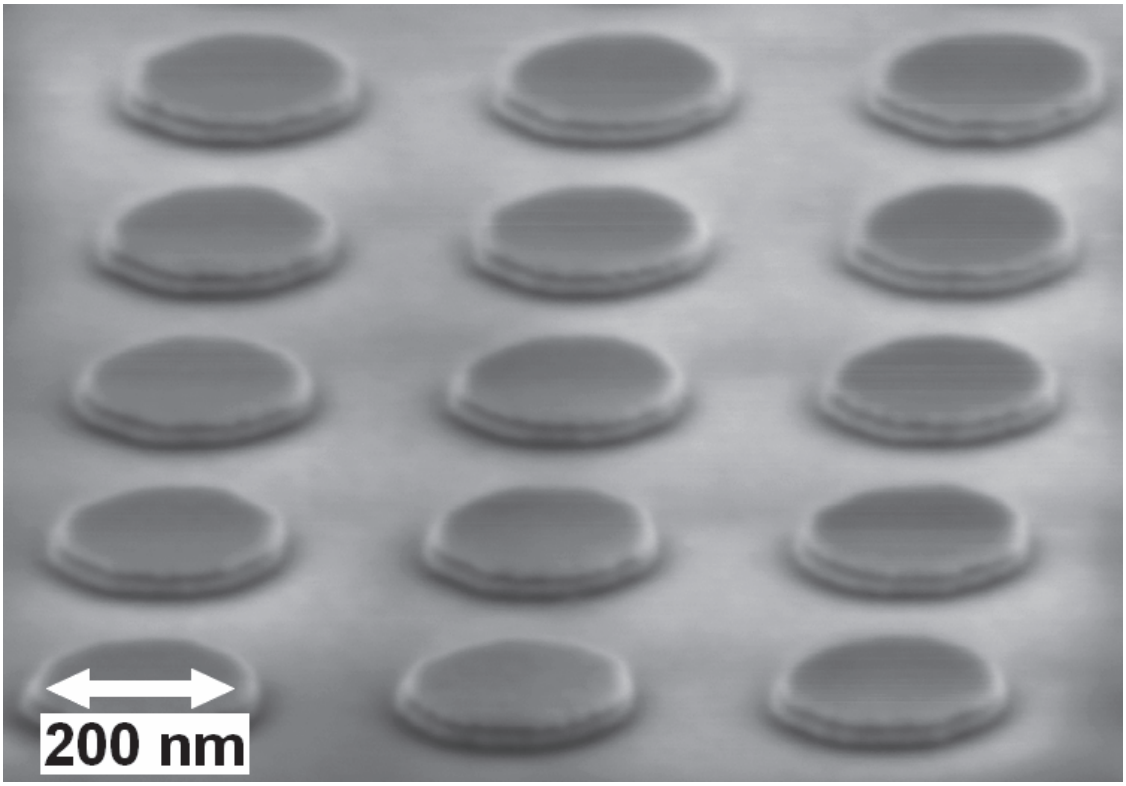

Figure 4.13: *Ti/Au/ZrO_2/Au 1/10/5/10 nm MIM structure on a Si wafer without adhesion layers between the Au and ZrO_2 layers.*

was broken between evaporations. This probably decreases adhesion due to surface contamination but still the layers did not notably laminate. The yield, i.e. the percentage of the undamaged MIM structures from the patterns in the stamp, was about 95%.

Chapter 5

Applications of sub-wavelength photonic structures

In this chapter the main results of the thesis are presented and discussed. A large share of this thesis is about the fabrication of metallic nanocones. These nanocones are very interesting structures for plasmonics. They localize light into a tight spot at the tip of the cone. This gives rise to the enhancement of various interactions, for example, second harmonic generation (SHG) and Raman scattering.

Also a guided-mode resonance (GMR) mirror is presented. It was used to realize a broadband mirror with a high reflectivity. This GMR mirror was applied in a semiconductor disk laser as an output coupler mirror.

5.1 Nanocones

As described earlier in Chapter 1, gold nanocones were more or less a lucky a by-product of other tests. This is the way new discoveries are often made in science and technology, although it is not commonly acknowledged. Furthermore, like many useful practices related to processing, the fabrication method of the cones was found to have been proposed in the 1960s, in this case by Spindt et al. [135]. A similar process has been used in the fabrication of field-emission cathodes. Recently the cathodes have been applied in surface-conduction electron-emitter displays [136]. However, such a process has not

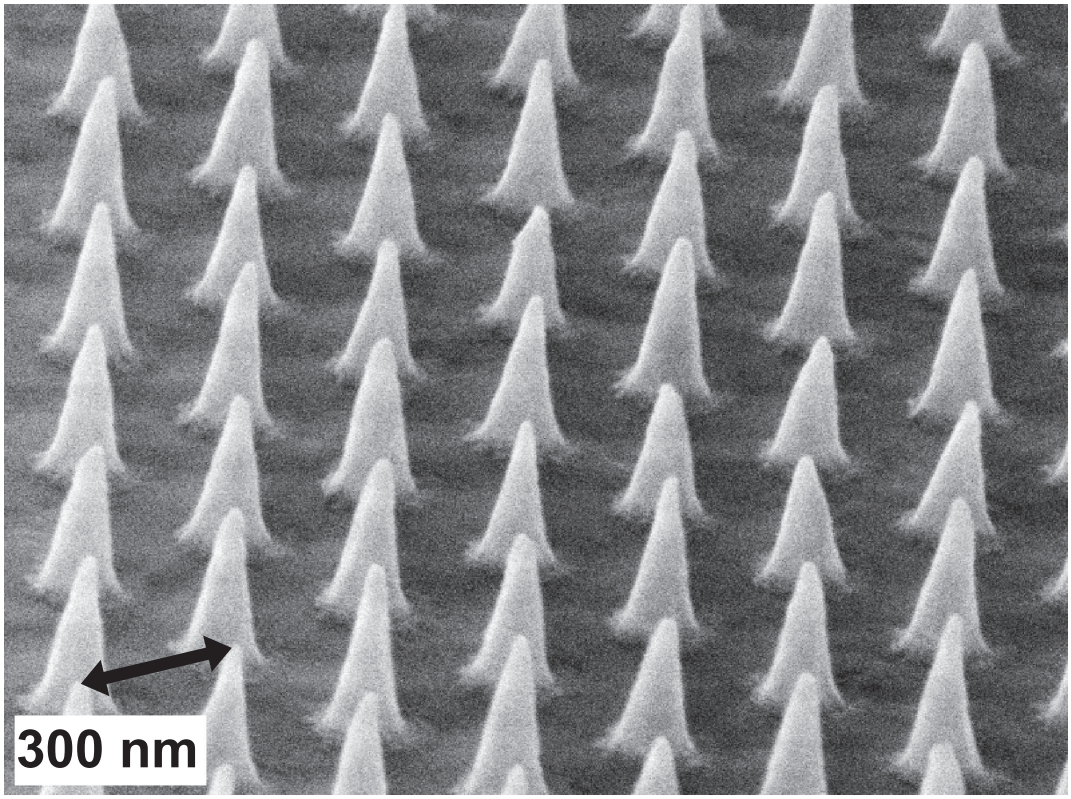

Figure 5.1: *An array of Au nanocones on a Si wafer. The period is 300 nm and the base diameter is 130 nm.*

been reported with NIL yet.

5.1.1 SHG in nanocones

As described above, metallic nanocones were expected to efficiently concentrate incident light at their tips. To investigate this local field enhancement in practice the plasmonic and nonlinear optical properties of the nanocones were studied in P1. Extinction measurements can be used to reveal the plasmon resonances. A SNOM would be an obvious choice for studies of the local-field but we had no access to such a system. However, SHG can be used to get qualitative data of the local fields. The SHG signal scales with the fourth power of the field intensity. Therefore, it is very sensitive to changes in the local fields. The SHG studies were made by the Nonlinear Optics Group in the Optics Laboratory, Tampere University of Technology.

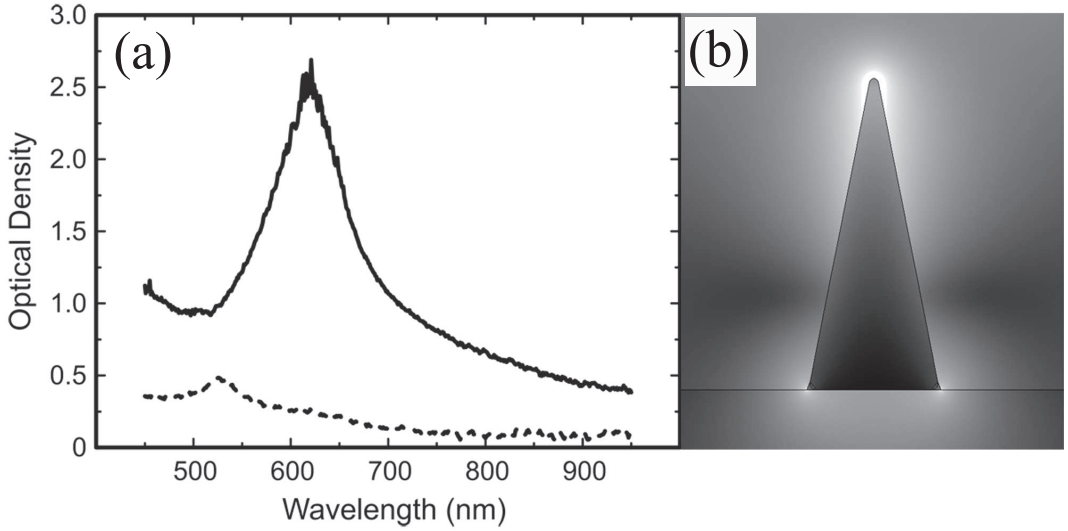

Figure 5.2: *(a) Extinction spectra for TM-polarized light at 50 °C angle of incidence for nanocones with (solid line) and without (dashed line) sharp tips. (b) A 3D finite-element simulation of electric field distribution in a gold nanocone with a 5 nm tip radius of curvature, illuminated from above by a focused radially-polarized beam at 1060 nm wavelength. The scale is logarithmic and cropped at 85% for better visibility.*

To quantify the enhancement of the SH response from the nanocones, we had a reference sample consisting of a similar array of half-cones with 88 nm height. The half-cones were fabricated by stopping the metal evaporation before the hole was closed and the sharp tip was formed. Their longitudinal plasmon is shifted to a slightly shorter wavelength of 525 nm (Fig. 5.2a) compared to the full nanocones that had a resonance at 615 nm. Therefore, our reference sample is actually closer to the secong harmonic frequencies of our laser than the sample with the sharp tips.

To demonstrate the strong local fields at the tips of the cones, optical SHG with an ultrafast pulsed Nd:glass laser (wavelength 1060 nm, pulse length 200 fs, repetition rate 82 MHz) was used. Note that the fundamental wavelength is non-resonant with the plasmon peak, but the SH wavelength of 530 nm is inside the rather wide resonance. The diameter of the focal spot in the experiment was about 3 μm, so there were approximately 80 nanocones within the spot area. The SH signal was detected by a photomultiplier tube combined with a single-photon counting system.

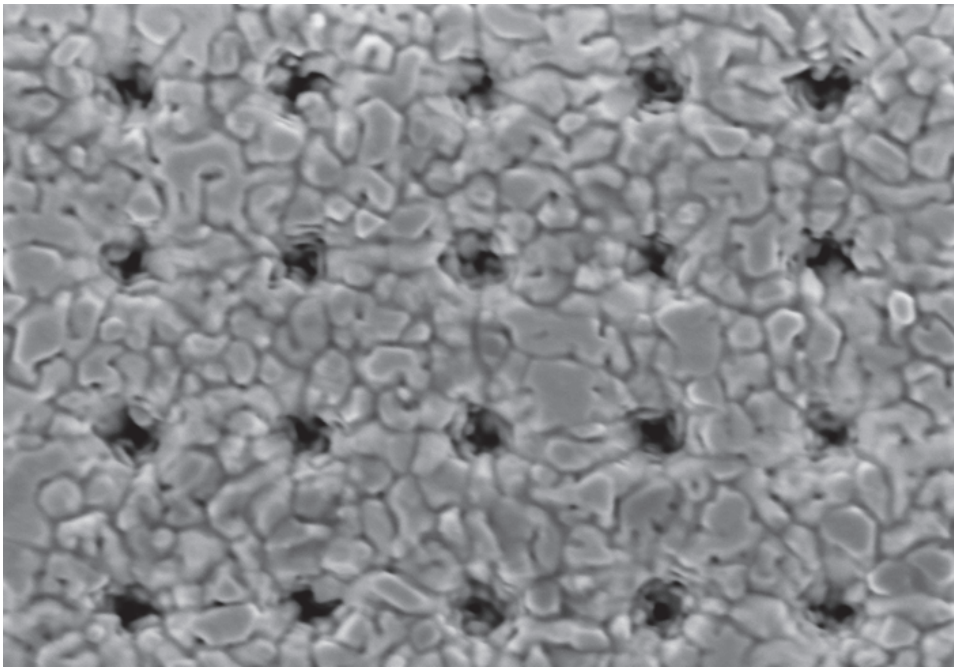

Figure 5.3: *A nanocone sample immediately after evaporation of Ti/Au 20/400 nm. Au has started to form grains but the holes have still shrunk uniformly.*

In order to couple the incident beam with the plasmon resonance in the direction of the axis of the cone, a polarization component along the axis direction was needed. To avoid problems caused by an oblique angle of incidence with the periodic structures we used a focused radially-polarized fundamental beam, which has a strong longitudinal electric field component at the focal plane, while the lateral polarization components cancel each other. Simulations using the finite-element method (Comsol, see Chapter 2.3.1) show that this situation leads to a strongly enhanced field (white area in Fig. 5.2b) at the tip of the cone.

Fig. 5.4 presents the SH signals from the two samples as they were scanned in the focal plane. There is a significant fluctuation in the SH signal for the sharp nanocones, whereas the signal from the reference sample is slightly more uniform. During the scan the nanocones are moving into and out of the focal area.

The sensitivity of the nanocones arises from the fact that the SH intensity is proportional to the fourth power of the local fundamental field and to the second power of the local SH field. Therefore, the SH signal is very sensitive to the variations in the features

of the nanocones and further to their local fields. To quantify the enhancement, the SH signals was averaged over the whole transverse scan. The SH intensity from the sample with the sharp nanocones was enhanced by a factor of 150 compared to the half-cones. Clearly, the sharp nanocones are efficient in producing strong local electric fields.

SH scans reveal that the nanocones are not totally identical. Imperfections tend to accumulate in the fabrication process. Therefore, variations in the master mold will be amplified after the NIL and the lift-off steps. An even stronger effect comes from the granulation of the metal layer during the evaporation of the metal. The granulation is very strong, especially with Ag and Al. However, grain formation can be seen also with Au (see Fig. 5.3) which causes a small variation in shrinkage rate of the hole. These things together cause the variation of the SH signal.

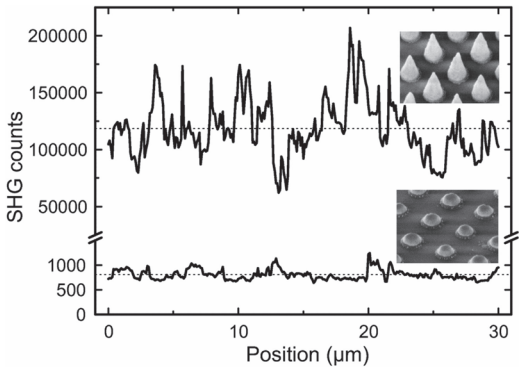

Figure 5.4: *A SHG signal as the sample is scanned in the transverse direction. The measurement is done for sharp nanocones, height* 291 *nm, and half-cones, height* 88 *nm. Dashed lines illustrate the average SHG intensities.*

SHG can be used to identify defects of the individual metallic nanoparticles by scanning with the cylindrical vector beam [137] the area where the nanopatterns, in this case nanocones, are located [64]. The beam size must be smaller than the period of the nanocones in order to see the response from the individual nanocones. When radial (RP) or azimuthal polarization (AP) is applied, light can couple to a nanocone. The SHG response is sensitive to the geometry and changes in the morphology. Using cylindrical vector beams in the SHG scan it is possible to see features that would not be visible when scanning with linearly polarized light.

5.1.2 Raman scattering in nanocones

The nanocone process is also capable of producing more complicated shapes. In addition to the L-shaped particles shown before, pairs of cones with a low bridge between them were fabricated. A simple approach to prepare the bridged nanocones with sharp

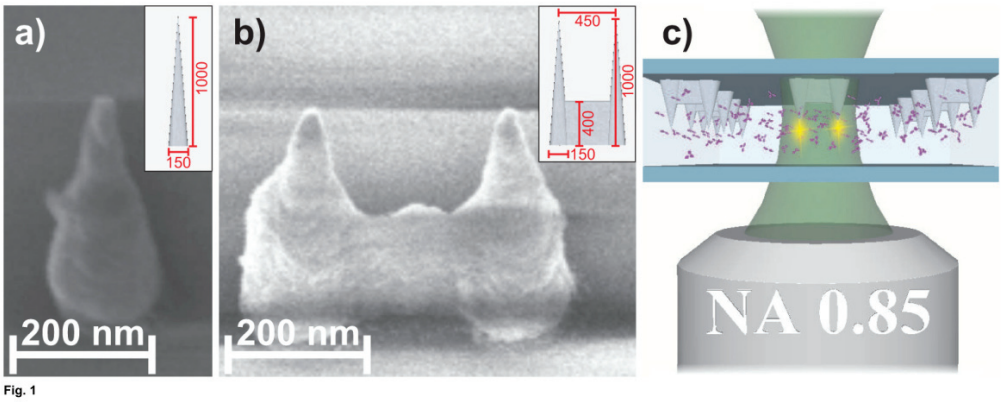

Figure 5.5: *a) A single Ag nanocone. b) A bridged nanocone. Dimensions are in the inset. c) A schematic from the measurement setup.*

tips that outperform single nanocones in terms of the achievable Raman signal enhancement was presented in P4. The measurements were done in the ICFO, Spain. Two silver nanocones were connected by a silver bridge that overcomes the relatively large separation distance to achieve plasmon coupling between the two cones. The structure was intended to mimic the planar ”U-shaped” split-ring-resonator (SRR) where plasmon coupling between the two arms is facilitated through a base wire [138, 139]. Additionally, the sharp tips at the ends of the arms are shown to be favorable for the field enhancement effects.

A master template having a lattice of both cylindrical holes (single nanocones) and connected hole pairs (bridged nanocones) was first prepared by EBL on a silicon wafer. The fabrication process of the nanocones followed a similar lift-off procedure as presented in 4.1. The conical shape of the nanocones was defined through the deposition of a titanium adhesion layer (20 nm) followed by the evaporation of 1000 nm of silver. Because the bridge between the holes is narrower than holes, it is closed earlier and the height of the bridge remains lower than the height of the nanocones themselves. This process gives rise for the ”U-shaped” metal nanostructures.

Each cone had a base diameter of 150 nm and a height of approximately 1 µm with a final tip radius of curvature of approximately 5 nm. The period of the single cone array was 1 µm. The bridged nanocone structures consisted of two nanocones separated by

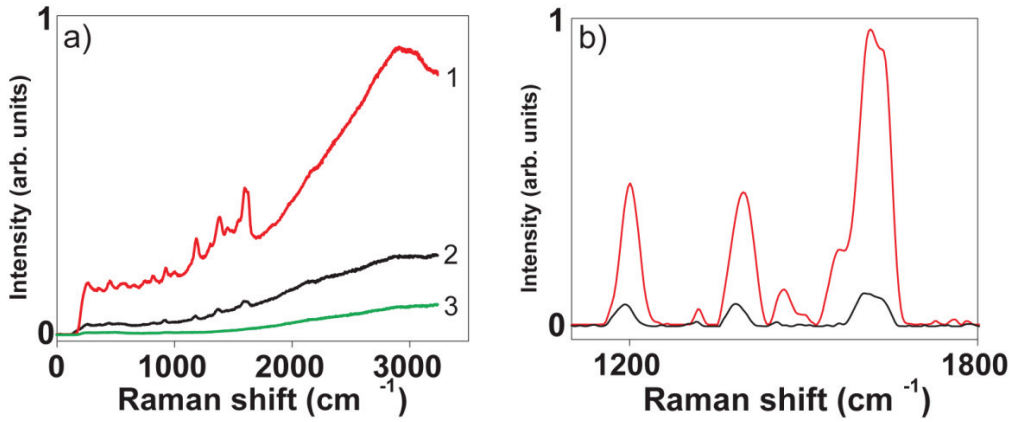

Figure 5.6: *Raman spectra from the bridged nanocone. a) The emission spectra for the bridged nanocone (1) and single nanocone (2) in the presence of crystal violet. The background signal (3) was obtained by measuring from a point in the solution away from the cones. b) The resulting Raman bands after the CV fluorescence background has been removed demonstrating the TERS enhancement improvement of the bridged nanocones (red) compared to the single nanocone (black).*

450 nm and connected with the metal bridge in an array of the same periodicity as the single cones. The bridge was 50 nm wide and 330 nm in height. An array of single nanocones with the period of 450 nm was fabricated and tested in order to mimic a pair of cones in the absence of a bridge as a reference.

A comparison of the emitted signals from the structures in the presence of crystal violet (CV) molecules is given in Fig. 5.6. The Raman and fluorescence bands of the CV molecules are clearly observed and at this dye concentration, no Raman signal and a low fluorescence signal above the noise level was observed at the same excitation power out of the area of the nanocones. The three main peaks, at 1200, 1400, and 1615 cm^{-1}, agree with the previous observations of the CV SERS spectrum [140].

The bridge clearly alters the optical properties of the system, leading to a four-fold increase in the fluorescence output from a single nanocone. The TERS enhancement is even higher: the three main CV peaks experience an average 8-fold Raman intensity increase relative to the single nanocone.

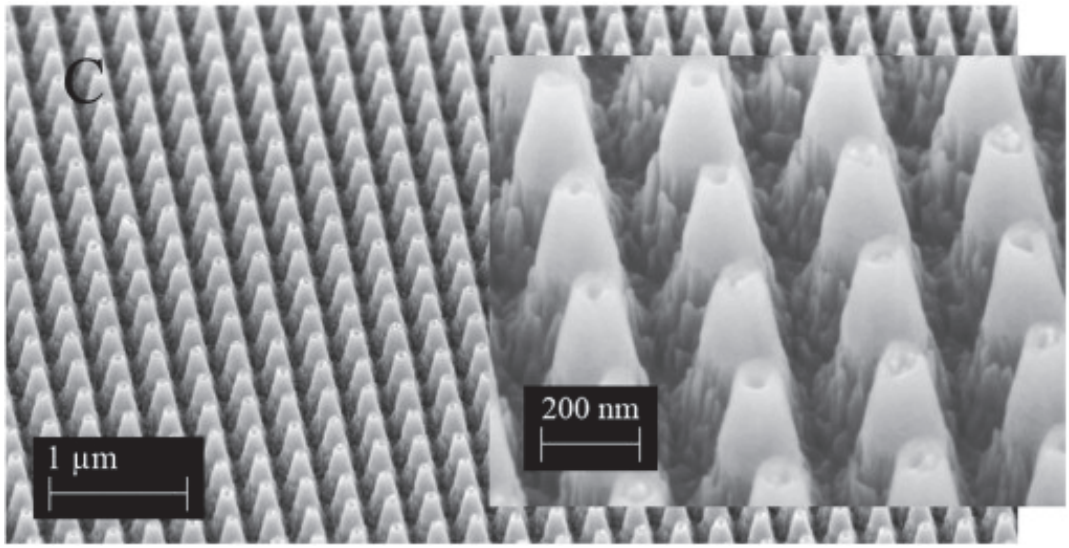

Figure 5.7: *Etched AlInP nanocones fabricated using the Ge nanocone array as a master mold of the NIL stamp. Reprinted from [141]. Copyright (2010), with permission from Elsevier.*

5.1.3 Moth-eye templete

Solar cell technology is highly growing branch of photonics. Since a single (semiconductor) junction only captures light at a limited spectrum, a multijunction cell are ofter used [142]. To collect all available light into the active region of the cell, an antireflective coating is needed. One way to realize a highly efficient antireflective layer is to use a moth-eye structure [143].

Tommila et al. [141] used nanoimprint lithography to realize the moth-eye structure on aluminum indium phosphide (AlInP) compound commonly used as a window layer in high-efficiency multijunction solar cells. They used Ge nanocones as master template for NIL stamp fabrication. Ge nanocones are very attractive for this purpose because of good uniformity, a feasible shape of the structures and a large area of the patterns. With this stamp conical resist patters were imprinted. These resist cones were further dry etched into SiN_x which was used as an etch mask for the etching of the AlInP layer. Etch recipes were optimized to preserve the aspect ratio and the shape of the patterns.

With the moth-eye AR coating an average reflectivity of 2.7% was achieved for a

wide spectral range of 450 – 1650 nm. An un-etched 1 μm AlInP layer was used as a reference which exhibited an average reflectivity of 26.4% over the measured spectral range. Therefore, this biomimetic structure resulted in an order-of-magnitude decrease in reflectivity.

5.2 Guided-mode resonance mirror in IR wavelengths

During the testing of the fabrication of the nanocones from different materials it was noted that Ge can be used to fabricate very smooth and uniform nanostructures. Previous experiences from the lift-off process had shown that it is easy to etch with plasma. This, combined with the good optical properties in the IR range urged us to develop an application using these benefits of Ge.

5.2.1 GMR mirror

In P3 we demonstrated that germanium is an attractive material for a broadband IR guided-mode resonance mirror. It has a very high index of refraction of about 4.0 in the IR [123] and a band gap of 0.66 eV. The absorption of Ge is very small for the wavelengths above the bandgap and the transmission spectrum extends from 1.9 μm to over 17 μm which is a wider range than that of silicon (1.06 – 6.7 μm).

Bulk Ge is a common window material in the IR region. However, there are only a few reports concerning Ge as a material for micro/nano-optical components in the literature. Ge has been used to realize planar photonic crystal structures [127, 144]. Previous reports have also demonstrated broadband reflectors fabricated out of silicon [145]. However, mainly low refractive index materials have been used to realize GMR mirrors resulting in a narrower reflection band, and usually in visible range [146] or in near-IR [147].

The grating mirror was designed for TM-polarized light (E-field is perpendicular to the grating lines) using a 2D RCWA method (see Chapter 2.3.2). The operation range of the mirror was designed to be centered at 2.5 μm and the Nelder-Mead simplex search in method in Matlab was used to maximize the average reflectivity over a wavelength

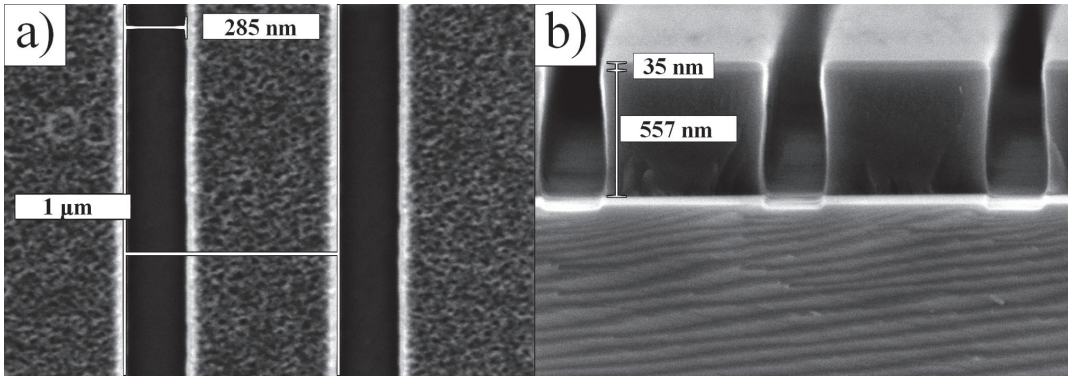

Figure 5.8: *a) Ge grating on a fused silica wafer with a 1 µm period and a 285 nm groove width imaged from above. b) Cross-section of the Ge grating on a Si reference wafer. The Ge layer is 557 nm thick and the residual SiNx etch mask layer is 35 nm thick. A Si wafer was used in reference sample to enable good cross-section quality for inspection of the etching profile.*

region of 1900 – 3000 nm. All of the structural parameters, i.e. period, fill factor and thickness of the grating, were free in the optimization.

The optimization process resulted in the period of the grating of 1 µm, the thickness of the Ge layer of 550 nm and the width of the grating groove of 280 nm (fill factor of 0.72). The effect of the residual SiN_x etch mask layer on the reflectivity spectrum was negligible and it was left over the Ge grating lines. This design resulted in a reflectivity of >95% for the wavelength range between 1850 nm and 3020 nm. Reflectivities approaching 100% could have been achieved by optimizing for a narrower wavelength range.

The fabrication tolerances were analyzed before processing the samples. From the simulation results shown in Fig. 5.9a it can be seen that the fill factor can vary from 0.72 to 0.765 while the reflectance remains over 90%. Note that if the fill factor decreases more than 0.01 from the optimum then the reflectivity around the wavelength of 2100 nm starts to decrease rapidly. Similar simulations were done for the Ge layer thickness (see Fig. 5.9b. The reflectivity stays above 90% with a Ge thickness of 506 – 550 nm.

The transmittance of the sample was measured with a Perkin Elmer Lambda 1050 UV/VIS/NIR spectrophotometer. The reflectance was derived from the transmittance

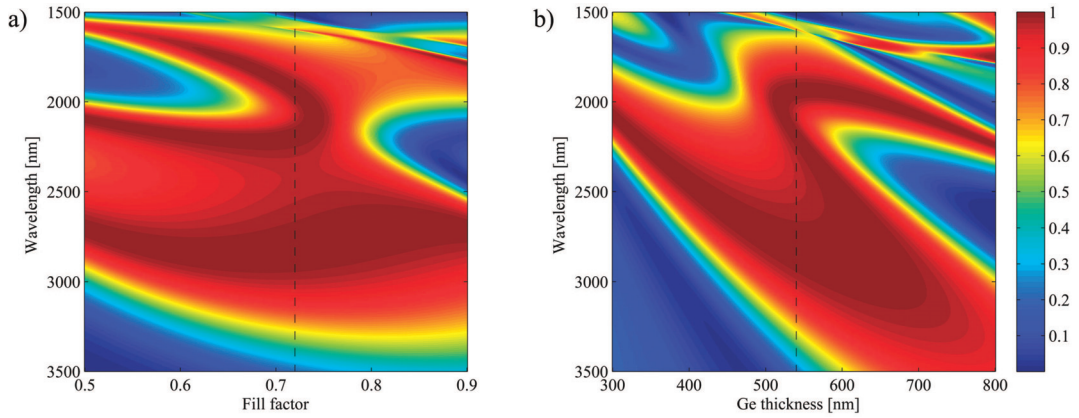

Figure 5.9: *Simulation of the reflectance of the GMR mirror design. Period of the grating design is fixed to 1.0 μm. a) Effect of changing the fill factor. The thickness of the Ge layer is fixed to 550 nm. b) Effect of Ge film thickness. Fill factor is fixed to 0.72. Dashed lines represent the reflectivity with the optimal operation conditions.*

because it was not possible to measure the reflectance in direct incidence with the instrument. The beam size was limited by a shutter to the 3×3 mm^2 grating area of the sample. An IR-range polarizer was aligned parallel to the grating lines for measurements in TE polarization and the sample was rotated 90° for measurements of the TM polarization. A silica wafer without a grating was used as a reference sample.

The absorption of the Ge layer was measured from the transmission spectrum of the unpatterned sample referencing a plain fused silica wafer. It was less than 1% in the designed operating range of the mirror. At the wavelength of 2335 nm the reflectance (Fig. 5.10) is at its maximum, reaching 98.8%. In the simulations the reflectance is ideally 99.99% when no absorption of the materials have been taken into account. This minor discrepancy can be explained by the small undercut in the grating edge profile (Fig. 5.8b) — the sidewalls in the design were perfectly vertical.

We estimated that this undercut decreases the effective grating linewidth by 25 nm and recalculated the reflectance spectra based on this. This simple approximation results in good agreement with the experimental reflectivity spectrum, as can be seen in Fig. 5.10. The reduced reflectivity at the wavelength of ∼2100 nm can be explained by a deviation from the optimum fill factor as can be seen in Fig 5.9a. The rest of the

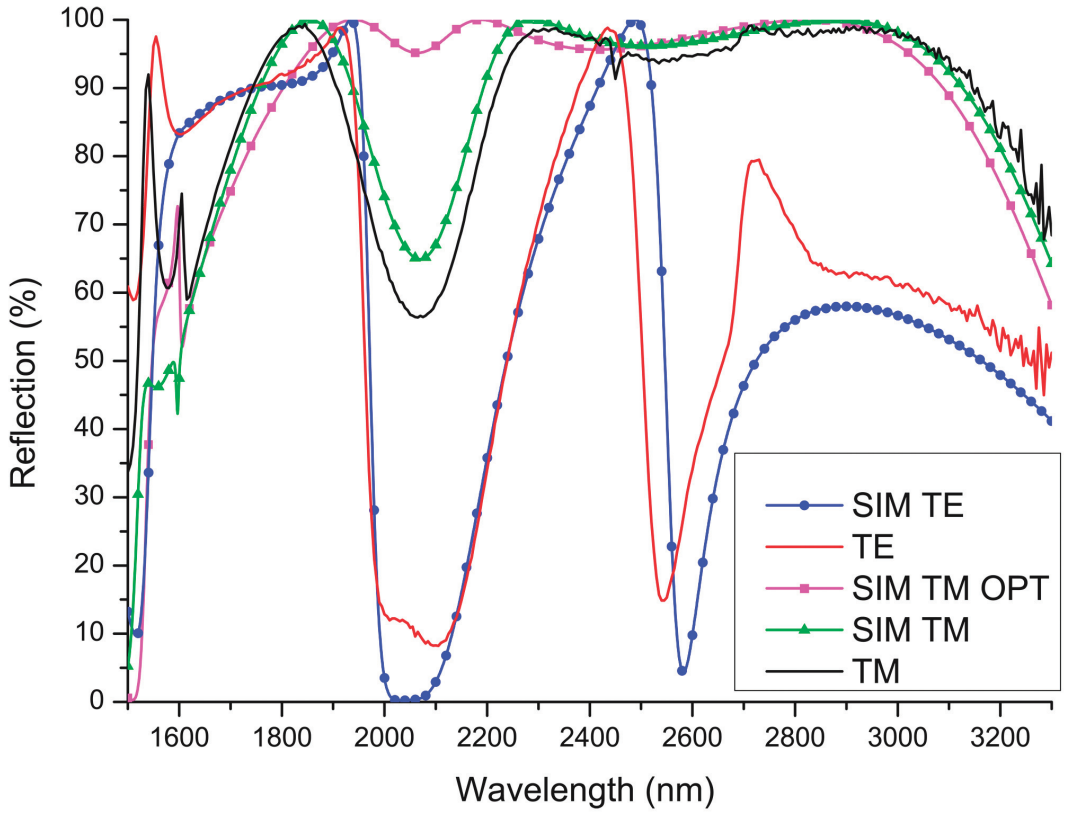

Figure 5.10: *Measured (solid lines) and simulated (dotted lines) reflection spectra of the Ge mirror for TM and TE polarization. The mirror was designed for TM polarization ("SIM TM OPT"). The spectra ("TM" and "TE") were derived from transmission measurements with an IR-spectrophotometer. "SIM TM" and "SIM TE" spectra represent simulated reflectivities for the measured sample with the realized dimensions.*

measurement closely follows the spectrum of the optimal design.

A slight problem in the transmission measurement is introduced by the strong characteristic OH-absorption peak of fused silica at 2.7 µm [148]. Comparing the simulated transmission spectrum with the experimental spectrum, it can be clearly seen that the measured peak at the 2.7 µm is a result of the absorption of the substrate. This absorption peak is missing in the reflectivity spectrum measured from the GMR mirror sample by Fourier transform spectroscopy (FTIR) but was visible in the transmission spectrum of the fused silica substrate. However, it was observed that this OH-absorption peak was

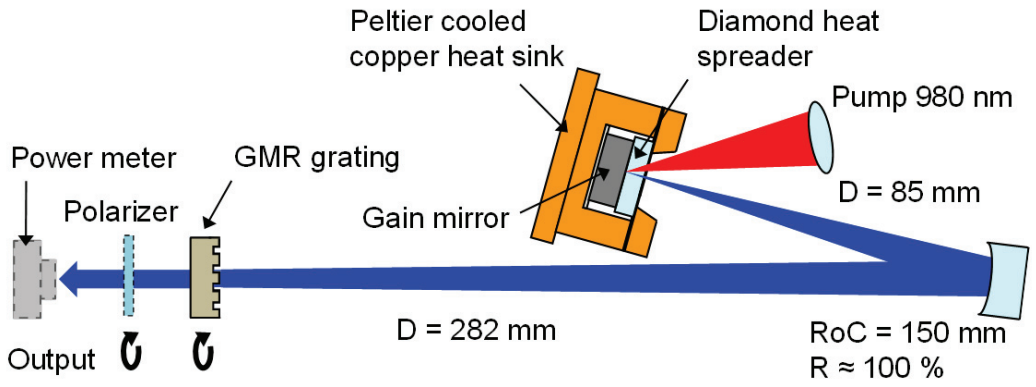

Figure 5.11: *A detailed illustration of the laser cavity with GMR grating used as an output coupler.*

smaller in the processed wafers than in out of box fused silica wafers. This is caused probably by annealing during the SiN_x layer growth in PECVD (at 300 °C).

Ge has a high index of refraction and low losses in the IR range. This allows the GMR mirrors to be designed for longer wavelengths than previously [145]. The main advantages of Ge are low cost and straightforward processing. Due to its extremely high index of refraction Ge mirrors can also operate as waveguides on various high-index semiconductors which is very important for integration.

5.2.2 GMR output coupler mirror in semiconductor disk lasers

A semiconductor disk laser (SDL), also called a vertical external-cavity surface-emitting laser (VECSEL), is a laser where the bottom mirror and the gain material, i.e. quantum wells, is made of compound semiconductor structure. It forms a cavity with an external mirror [149]. The advantages of VECSEL are a high beam quality, a relatively high output power and the adjustability of the wavelength. Usually they are optically pumped, but also electric pumping configurations are reported. Optical pumping is preferred because pumping can be more uniform on a large area. A more common application is ultrashort pulse generation which can be done by adding a semiconductor saturable absorber mirror into the cavity. Polarization stabilization is usually done with diffraction gratings, but their problem is the introduction of high losses in the cavity. Also a spe-

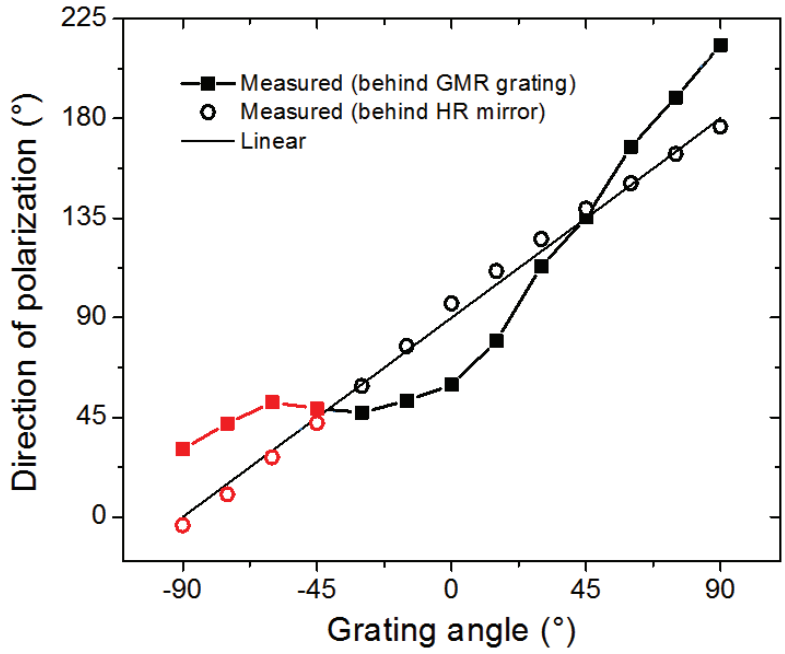

Figure 5.12: *The direction of the output polarization measured from behind the folding mirror and behind the grating. At the 0° grating angle grooves of the grating are lined vertically.*

cially designed laser mirror realized by highly-reflective grating has been presented for this purpose [150].

A GMR mirror was applied to a 2.35 μm SDL setup to be used as an output coupler in a V-shaped laser cavity (see Fig. 5.11). The advances of the GMR mirror in a SDL setup are polarization stabilization and broad-band reflectance, which allows various wavelengths to be tested with the same setup. The reflectance of the GMR mirror is different for TM and TE polarizations. Even a small difference in the reflectance can favor the other polarization mode and the lasing output becomes polarization stabilized.

The polarization dependence of the output beam, when the grating is rotated, is shown in Fig. 5.12. The polarization of the output beam was found to be linear with about 1:30 – 1:5 contrast between the TE and TM components. However, the polarization does not follow the grating angle linearly but slightly sinusoidally. The reason for this (initially) surprising observation is the fact that the response of the gain mirror also depends on polarization. This causes the small sinusoidal variation in the direction of

polarization measured behind the folding mirror (circles in the Fig. 5.12). Moreover, the transmission of the grating is different for TE and TM polarizations (ratio of 25/3).

In summary, it was shown that the GMR grating can be used as an output coupler in a SDL setup to produce an output that is linearly polarized and the direction of polarization could be controlled by rotating the grating.

Chapter 6

Conclusions

This thesis has dealt with the fabrication and development of nanophotonic applications. UV-nanoimprint lithography was the main tool in realizing these nanostructures and the central impact of this thesis was the development of nanofabrication processes and working methods into nanoscale. Optical measurements of the nanostructures were used to demonstrate their functionality in practice.

A NIL-assisted nanocone fabrication process was developed, various metals were tested and the process was further optimized. An array of gold nanocones was used to enhance second-harmonic generation (SHG) and their morphology was investigated by scanning SHG maps with cylindrical vector beams. Silver bridged-nanocones were used to enhance the Raman signal in a tip-enhanced Raman scattering application. Nanocone arrays in wafer-scale volume were demonstrated by NIL. The NIL-fabricated nanocones were shown to be versatile tools for nanophotonics. In addition to demonstrated applications they could be used in field emission, trapping of nanoparticles and metamaterials.

Guided-mode resonance (GMR) was exploited to demonstrate a wide-band high reflectance IR-mirror using germanium as a grating material. The GMR mirror was shown to be a very efficient reflector and the operation region was pushed further into IR than in previously published work. The Ge mirror was also applied to a semiconductor disk laser operating at 2.35 μm as a polarization-stabilizing output coupler. A narrow-band version of the mirror could be used to simultaneously achieve polarization and wavelength selectivity for a laser.

The main achievement of this thesis was the development of fabrication methods for nanophotonic applications using tools that enable industrial-scale fabrication. This work hopefully will support with emerging commercial nanophotonic applications and for its part help the North to succeed in the globalizing world. The field has been plowed.

Bibliography

[1] R. Feynman, "There's plenty of room at the bottom," *Engineering and Science*, vol. 23, no. 5, pp. 22–36, 1960.

[2] R. Stulen, "13-nm extreme ultraviolet lithography," *Selected Topics in Quantum Electronics, IEEE Journal of*, vol. 1, no. 3, pp. 970–975, sep 1995.

[3] M. Switkes and M. Rothschild, "Immersion lithography at 157 nm," *Journal of Vacuum Science and Technology B: Microelectronics and Nanometer Structures*, vol. 19, no. 6, pp. 2353–2356, nov 2001.

[4] S. Y. Chou, P. R. Krauss, and P. J. Renstrom, "Imprint of sub-25 nm vias and trenches in polymers," *Applied Physics Letters*, vol. 67, pp. 3114–3116, 1995.

[5] F. Hua, Y. Sun, A. Gaur, M. A. Meitl, L. Bilhaut, L. Rotkina, J. Wang, P. Geil, M. Shim, J. A. Rogers, and A. Shim, "Polymer imprint lithography with molecular-scale resolution," *Nano Letters*, vol. 4, no. 12, pp. 2467–2471, 2004.

[6] "The Lycurgus Cup," The British Museum, Great Russell Street, London WC1, England. [Online]. Available: http://www.britishmuseum.org/explore/highlights/highlight_objects/pe_mla/t/the_lycurgus_cup.aspx

[7] J. Price, "A survey of the hellenistic and early roman vessel glass found on the unexplored mansion site at knossos in crete," in *Annales du 11e Congrès de l'Association Internationale pour l'Histoire du Verre*, 1988, pp. 27–36.

[8] K. Okamoto, I. Niki, A. Shvartser, Y. Narukawa, T. Mukai, and A. Scherer, "Surface-plasmon-enhanced light emitters based on InGaN quantum wells," *Nature Materials*, vol. 3, pp. 601–605, Sept. 2004.

[9] J. Maxwell, "XXV. on physical lines of force," *The London, Edinburgh, and Dublin Philosophical Magazine and Journal of Science*, vol. 21, no. 139, pp. 161–175, 1861.

[10] O. Heaviside, "On the forces, stresses, and fiuxes of energy in the electromagnetic field," *Philosophical Transactions of the Royal Society of London. A*, vol. 183, pp. 423–480, 1892.

[11] S. Wang, R. Magnusson, J. Bagby, and M. Moharam, "Guided-mode resonances in planar dielectric-layer diffraction gratings," *JOSA A*, vol. 7, no. 8, pp. 1470–1474, 1990. [Online]. Available: http://josaa.osa.org/abstract.cfm?URI=josaa-7-8-1470

[12] D. Rosenblatt, A. Sharon, and A. A. Friesem, "Resonant grating waveguide structures," *IEEE Journal of Quantum Electronics*, vol. 33, pp. 2038–2059, Nov. 1997.

[13] R. W. Wood, "On a remarkable case of uneven distribution of light in a diffraction grating spectrum," *Proceedings of the Physical Society of London*, vol. 18, no. 1, p. 269, 1902. [Online]. Available: http://stacks.iop.org/1478-7814/18/i=1/a=325

[14] A. Hessel and A. A. Oliner, "A new theory of Wood's anomalies on optical gratings," *Appl. Opt.*, vol. 4, no. 10, pp. 1275–1297, Oct 1965. [Online]. Available: http://ao.osa.org/abstract.cfm?URI=ao-4-10-1275

[15] S. S. Wang and R. Magnusson, "Theory and applications of guided-mode resonance filters," *Appl. Opt.*, vol. 32, no. 14, pp. 2606–2613, May 1993. [Online]. Available: http://ao.osa.org/abstract.cfm?URI=ao-32-14-2606

[16] A. Greenwell, "Rigorous analysis of wave guiding and diffractive integrated optical structures," Ph.D. dissertation, University of Central Florida Orlando, Florida, 2007.

[17] M. Shokooh-Saremi and R. Magnusson, "Wideband leaky-mode resonance reflectors: Influence of grating profile and sublayers," *Optics express*, vol. 16, no. 22, pp. 18 249–18 263, 2008.

[18] Z. Liu and R. Magnusson, "Concept of multiorder multimode resonant optical filters," *Photonics Technology Letters, IEEE*, vol. 14, no. 8, pp. 1091–1093, 2002.

[19] H. Wu, W. Mo, J. Hou, D. Gao, R. Hao, H. Jiang, R. Guo, W. Wu, and Z. Zhou, "A high performance polarization independent reflector based on a multilayered configuration grating structure," *Journal of Optics*, vol. 12, no. 4, p. 045703, 2010.

[20] J. Heber, "Plasmonics: Surfing the wave," *Nature*, vol. 461, pp. 720–722, 2009.

[21] A. Sommerfeld, "Ueber die fortpflanzung elektrodynamischer wellen längs eines drahtes," *Annalen der Physik*, vol. 303, no. 2, pp. 233–290, 1899. [Online]. Available: http://dx.doi.org/10.1002/andp.18993030202

[22] J. Garnett, "Colours in metal glasses and in metallic films." *Proceedings of the Royal Society of London*, vol. 73, no. 488-496, pp. 443–445, 1904.

[23] G. Mie, "Beiträge zur optik trüber medien, speziell kolloidaler metallösungen," *Annalen der Physik*, vol. 330, no. 3, pp. 377–445, 1908. [Online]. Available: http://dx.doi.org/10.1002/andp.19083300302

[24] A. Clebsch, "Über die reflexion an einer kugelfläche," *J. Math*, vol. 61, p. 195, 1863.

[25] D. Pines, "Collective energy losses in solids," *Rev. Mod. Phys.*, vol. 28, pp. 184–198, Jul 1956. [Online]. Available: http://link.aps.org/doi/10.1103/RevModPhys.28.184

[26] J. J. Hopfield, "Theory of the contribution of excitons to the complex dielectric constant of crystals," *Phys. Rev.*, vol. 112, pp. 1555–1567, Dec 1958. [Online]. Available: http://link.aps.org/doi/10.1103/PhysRev.112.1555

[27] R. H. Ritchie, “Plasma losses by fast electrons in thin films,” *Phys. Rev.*, vol. 106, pp. 874–881, Jun 1957. [Online]. Available: http://link.aps.org/doi/10.1103/PhysRev.106.874

[28] R. H. Ritchie, E. T. Arakawa, J. J. Cowan, and R. N. Hamm, “Surface-plasmon resonance effect in grating diffraction,” *Phys. Rev. Lett.*, vol. 21, pp. 1530–1533, Nov 1968. [Online]. Available: http://link.aps.org/doi/10.1103/PhysRevLett.21.1530

[29] E. Kretschmann and H. Raether, “Radiative decay of nonradiative surface plasmons excited by light,” *Z. Naturforsch. A*, vol. 23, p. 2135, 1968.

[30] A. Otto, “Excitation of nonradiative surface plasma waves in silver by the method of frustrated total reflection,” *Zeitschrift für Physik A Hadrons and Nuclei*, vol. 216, pp. 398–410, 1968, 10.1007/BF01391532. [Online]. Available: http://dx.doi.org/10.1007/BF01391532

[31] U. Kreibig and P. Zacharias, “Surface plasma resonances in small spherical silver and gold particles,” *Zeitschrift fur Physik*, vol. 231, pp. 128–143, Apr. 1970.

[32] S. L. Cunningham, A. A. Maradudin, and R. F. Wallis, “Effect of a charge layer on the surface-plasmon-polariton dispersion curve,” *Phys. Rev. B*, vol. 10, pp. 3342–3355, Oct 1974. [Online]. Available: http://link.aps.org/doi/10.1103/PhysRevB.10.3342

[33] M. Fleischmann, P. J. Hendra, and A. J. McQuillan, “Raman spectra of pyridine adsorbed at a silver electrode,” *Chemical Physics Letters*, vol. 26, pp. 163–166, May 1974.

[34] J. G. Rivas, M. Kuttge, P. H. Bolivar, H. Kurz, and J. A. Sánchez-Gil, “Propagation of surface plasmon polaritons on semiconductor gratings,” *Phys. Rev. Lett.*, vol. 93, p. 256804, Dec 2004. [Online]. Available: http://link.aps.org/doi/10.1103/PhysRevLett.93.256804

[35] P. Muys, "Electromagnetic field equations of the volume plasmon," *Opt. Lett.*, vol. 37, no. 23, pp. 4928–4930, Dec 2012. [Online]. Available: http://ol.osa.org/abstract.cfm?URI=ol-37-23-4928

[36] H. Myers, *Introductory solid state physics*. Taylor & Francis, 1990. [Online]. Available: http://books.google.fi/books?id=_IfwAAAAMAAJ

[37] S. Park, G. Lee, S. Song, C. Oh, and P. Kim, "Resonant coupling of surface plasmons to radiation modes by use of dielectric gratings," *Opt. Lett.*, vol. 28, no. 20, pp. 1870–1872, Oct 2003. [Online]. Available: http://ol.osa.org/abstract.cfm?URI=ol-28-20-1870

[38] M. Piliarik and J. Homola, "Surface plasmon resonance (SPR) sensors: approaching their limits?" *Optics express*, vol. 17, no. 19, pp. 16 505–16 517, 2009.

[39] U. Durig, D. W. Pohl, and F. Rohner, "Near-field optical-scanning microscopy," *Journal of Applied Physics*, vol. 59, no. 10, pp. 3318–3327, may 1986.

[40] P. Dawson, B. A. F. Puygranier, and J.-P. Goudonnet, "Surface plasmon polariton propagation length: a direct comparison using photon scanning tunneling microscopy and attenuated total reflection," *Phys. Rev. B*, vol. 63, p. 205410, Apr 2001. [Online]. Available: http://link.aps.org/doi/10.1103/PhysRevB.63.205410

[41] W. L. Barnes, A. Dereux, and T. W. Ebbesen, "Surface plasmon subwavelength optics," *Nature*, vol. 424, no. 6950, pp. 824–830, Aug. 2003. [Online]. Available: http://dx.doi.org/10.1038/nature01937

[42] A. Kolomenski, A. Kolomenskii, J. Noel, S. Peng, and H. Schuessler, "Propagation length of surface plasmons in a metal film with roughness," *Appl. Opt.*, vol. 48, no. 30, pp. 5683–5691, Oct 2009. [Online]. Available: http://ao.osa.org/abstract.cfm?URI=ao-48-30-5683

[43] N. Singh and T. Mogi, "Effective skin depth of em fields due to large circular loop and electric dipole sources," *Earth, planets and space*, vol. 55, no. 6, pp. 301–313, 2003.

[44] J. Dionne, L. Sweatlock, H. Atwater, and A. Polman, "Planar metal plasmon waveguides: frequency-dependent dispersion, propagation, localization, and loss beyond the free electron model," *Physical Review B*, vol. 72, no. 7, p. 075405, 2005. [Online]. Available: http://dx.doi.org/10.1103/PhysRevB.72.075405

[45] L. Novotny and B. Hecht, *Principles of Nano-Optics*. Cambridge University Press, 2006. [Online]. Available: http://books.google.fi/books?id=Qrf036kThTQC

[46] M. Brongersma and P. Kik, *Surface Plasmon Nanophotonics*, ser. Springer Series in Optical Sciences. Springer, 2007. [Online]. Available: http://books.google.fi/books?id=7QLHU-2QRSQC

[47] U. Kreibig and M. Vollmer, *Optical properties of metal clusters*. Springer, 1995. [Online]. Available: http://books.google.fi/books?id=jYhRAAAAMAAJ

[48] M. Scharte, R. Porath, T. Ohms, M. Aeschlimann, B. Lamprecht, H. Ditlbacher, and F. Aussenegg, "Lifetime and dephasing of plasmons in Ag nanoparticles," in *Proc. SPIE*, vol. 4456, 2001, pp. 14–21.

[49] M. Salerno, J. Krenn, A. Hohenau, H. Ditlbacher, G. Schider, A. Leitner, and F. Aussenegg, "The optical near-field of gold nanoparticle chains," *Optics communications*, vol. 248, no. 4, pp. 543–549, 2005. [Online]. Available: http://www.sciencedirect.com/science/article/pii/S0030401804012994

[50] V. Giannini, A. Fernández-Domínguez, S. Heck, and S. Maier, "Plasmonic nanoantennas: Fundamentals and their use in controlling the radiative properties of nanoemitters," *Chemical Reviews*, vol. 111, no. 6, pp. 3888–3912, 2011. [Online]. Available: http://pubs.acs.org/doi/abs/10.1021/cr1002672

[51] R. D. Grober, R. J. Schoelkopf, and D. E. Prober, "Optical antenna: Towards a unity efficiency near-field optical probe," *Applied Physics Letters*, vol. 70, no. 11, pp. 1354–1356, 1997. [Online]. Available: http://link.aip.org/link/?APL/70/1354/1

[52] M. Wissert, K. Ilin, M. Siegel, U. Lemmer, and H. Eisler, "Coupled nanoantenna plasmon resonance spectra from two-photon laser excitation," *Nano letters*, vol. 10, no. 10, pp. 4161–4165, 2010.

[53] B. Luk'yanchuk, N. I. Zheludev, S. A. Maier, N. J. Halas, P. Nordlander, H. Giessen, and C. T. Chong, "The Fano resonance in plasmonic nanostructures and metamaterials," *Nature Materials*, vol. 9, pp. 707–715, 2010.

[54] Y. Zhang, T. Jia, H. Zhang, and Z. Xu, "Fano resonances in disk–ring plasmonic nanostructure: strong interaction between bright dipolar and dark multipolar mode," *Optics Letters*, vol. 37, no. 23, pp. 4919–4921, 2012.

[55] U. Fano, "Effects of configuration interaction on intensities and phase shifts," *Phys. Rev.*, vol. 124, pp. 1866–1878, Dec 1961. [Online]. Available: http://link.aps.org/doi/10.1103/PhysRev.124.1866

[56] L. Novotny, R. X. Bian, and X. S. Xie, "Theory of nanometric optical tweezers," *Phys. Rev. Lett.*, vol. 79, pp. 645–648, Jul 1997. [Online]. Available: http://link.aps.org/doi/10.1103/PhysRevLett.79.645

[57] D. Débarre, W. Supatto, and E. Beaurepaire, "Structure sensitivity in third-harmonic generation microscopy," *Opt. Lett.*, vol. 30, no. 16, pp. 2134–2136, Aug 2005. [Online]. Available: http://ol.osa.org/abstract.cfm?URI=ol-30-16-2134

[58] M. Kauranen and A. V. Zayats, "Nonlinear plasmonics," *Nature Photonics*, vol. 6, pp. 737–748, 2012.

[59] B. Canfield, S. Kujala, K. Jefimovs, J. Turunen, and M. Kauranen, "Linear and nonlinear optical responses influenced by broken symmetry in an array of gold nanoparticles," *Opt. Express*, vol. 12, no. 22, pp. 5418–5423, Nov 2004. [Online]. Available: http://www.opticsexpress.org/abstract.cfm?URI=oe-12-22-5418

[60] P. A. Franken, A. E. Hill, C. W. Peters, and G. Weinreich, "Generation of optical harmonics," *Phys. Rev. Lett.*, vol. 7, pp. 118–119, Aug 1961. [Online]. Available: http://link.aps.org/doi/10.1103/PhysRevLett.7.118

[61] A. L. Schawlow and C. H. Townes, "Infrared and optical masers," *Phys. Rev.*, vol. 112, pp. 1940–1949, Dec 1958. [Online]. Available: http://link.aps.org/doi/10.1103/PhysRev.112.1940

[62] A. Härkönen, J. Rautiainen, T. Leinonen, Y. Morozov, L. Orsila, M. Guina, M. Pessa, and O. Okhotnikov, "Intracavity sum-frequency generation in dual-wavelength semiconductor disk laser," *Photonics Technology Letters, IEEE*, vol. 19, no. 19, pp. 1550 –1552, oct.1, 2007.

[63] C. Erny, K. Moutzouris, J. Biegert, D. Kühlke, F. Adler, A. Leitenstorfer, and U. Keller, "Mid-infrared difference-frequency generation of ultrashort pulses tunable between 3.2 and 4.8 μm from a compact fiber source," *Opt. Lett.*, vol. 32, no. 9, pp. 1138–1140, May 2007. [Online]. Available: http://ol.osa.org/abstract.cfm?URI=ol-32-9-1138

[64] G. Bautista, M. J. Huttunen, J. Mäkitalo, J. M. Kontio, J. Simonen, and M. Kauranen, "Second-harmonic generation imaging of metal nano-objects with cylindrical vector beams," *Nano Letters*, vol. 12, no. 6, pp. 3207–3212, 2012. [Online]. Available: http://pubs.acs.org/doi/abs/10.1021/nl301190x

[65] C. V. Raman and K. S. Krishnan, "A New Type of Secondary Radiation," *Nature*, vol. 121, pp. 501–502, 1928.

[66] P. Yu and M. Cardona, *Fundamentals of Semiconductors: Physics and Materials Properties*, ser. Advanced texts in physics. Springer, 2005. [Online]. Available: http://books.google.fi/books?id=W9pdJZoAeyEC

[67] P. C. Ashok, B. B. Praveen, and K. Dholakia, "Near infrared spectroscopic analysis of single malt Scotch whisky on an optofluidic chip," *Opt. Express*, vol. 19, no. 23, pp. 22 982–22 992, Nov 2011. [Online]. Available: http://www.opticsexpress.org/abstract.cfm?URI=oe-19-23-22982

[68] D. L. Jeanmaire and R. P. V. Duyne, "Surface Raman spectroelectrochemistry: Part I. heterocyclic, aromatic, and aliphatic amines adsorbed on the anodized silver electrode," *Journal of Electroanalytical Chemistry and Interfacial*

Electrochemistry, vol. 84, no. 1, pp. 1–20, 1977. [Online]. Available: http://www.sciencedirect.com/science/article/pii/S0022072877802246

[69] M. G. Albrecht and J. A. Creighton, "Anomalously intense Raman spectra of pyridine at a silver electrode," *Journal of the American Chemical Society*, vol. 99, no. 15, pp. 5215–5217, 1977. [Online]. Available: http://pubs.acs.org/doi/abs/10.1021/ja00457a071

[70] E. C. Le Ru, E. Blackie, M. Meyer, and P. G. Etchegoin, "Surface enhanced Raman scattering enhancement factors: A comprehensive study," *The Journal of Physical Chemistry C*, vol. 111, no. 37, pp. 13 794–13 803, 2007. [Online]. Available: http://pubs.acs.org/doi/abs/10.1021/jp0687908

[71] K. Kneipp, Y. Wang, H. Kneipp, L. T. Perelman, I. Itzkan, R. R. Dasari, and M. S. Feld, "Single molecule detection using surface-enhanced Raman scattering (SERS)," *Phys. Rev. Lett.*, vol. 78, pp. 1667–1670, Mar 1997. [Online]. Available: http://link.aps.org/doi/10.1103/PhysRevLett.78.1667

[72] M. Kerker, D.-S. Wang, and H. Chew, "Surface enhanced Raman scattering (SERS) by molecules adsorbed at spherical particles: errata," *Appl. Opt.*, vol. 19, no. 24, pp. 4159–4174, Dec 1980. [Online]. Available: http://ao.osa.org/abstract.cfm?URI=ao-19-24-4159

[73] M. Weaver, S. Zou, and H. Chan, "Peer reviewed: The new interfacial ubiquity of surface-enhanced raman spectroscopy," *Analytical Chemistry*, vol. 72, no. 1, pp. 38–47, 2000.

[74] P. F. Liao and A. Wokaun, "Lightning rod effect in surface enhanced Raman scattering," *The Journal of Chemical Physics*, vol. 76, no. 1, pp. 751–752, 1982. [Online]. Available: http://link.aip.org/link/?JCP/76/751/1

[75] J. Wessel, "Surface-enhanced optical microscopy," *J. Opt. Soc. Am. B*, vol. 2, no. 9, pp. 1538–1541, Sep 1985. [Online]. Available: http://josab.osa.org/abstract.cfm?URI=josab-2-9-1538

[76] F. Zenhausern, M. P. O'Boyle, and H. K. Wickramasinghe, "Apertureless near-field optical microscope," *Applied Physics Letters*, vol. 65, no. 13, pp. 1623–1625, 1994. [Online]. Available: http://link.aip.org/link/?APL/65/1623/1

[77] E. A. Todd and M. D. Morris, "Micron surface-enhanced Raman spectroscopy of intact biological organisms and model systems," *Applied Spectroscopy*, vol. 48, no. 5, pp. 545–548, 1994. [Online]. Available: http://www.ingentaconnect.com/content/sas/sas/1994/00000048/00000005/art00002

[78] R. M. Stöckle, Y. D. Suh, V. Deckert, and R. Zenobi, "Nanoscale chemical analysis by tip-enhanced Raman spectroscopy," *Chemical Physics Letters*, vol. 318, pp. 131–136, 2000. [Online]. Available: http://www.sciencedirect.com/science/article/pii/S0009261499014517

[79] M. S. Anderson, "Locally enhanced Raman spectroscopy with an atomic force microscope," *Applied Physics Letters*, vol. 76, no. 21, pp. 3130–3132, 2000. [Online]. Available: http://link.aip.org/link/?APL/76/3130/1

[80] N. Hayazawa, Y. Inouye, Z. Sekkat, and S. Kawata, "Metallized tip amplification of near-field Raman scattering," *Optics communications*, vol. 183, no. 1, pp. 333–336, 2000.

[81] B. Yeo, J. Stadler, T. Schmid, R. Zenobi, and W. Zhang, "Tip-enhanced raman spectroscopy – Its status, challenges and future directions," *Chemical Physics Letters*, vol. 472, no. 1, pp. 1–13, 2009. [Online]. Available: http://www.sciencedirect.com/science/article/pii/S0009261409001778

[82] O. Zienkiewicz and R. Taylor, *Finite Element Method: Volume 1 - The Basis*, 5th ed. Oxford: Butterworth-Heinemann, 2000.

[83] M. G. Moharam and T. K. Gaylord, "Rigorous coupled-wave analysis of planar-grating diffraction," *J. Opt. Soc. Am.*, vol. 71, no. 7, pp. 811–818, Jul 1981. [Online]. Available: http://www.opticsinfobase.org/abstract.cfm?URI=josa-71-7-811

[84] H. Herzig, *Micro-Optics: Elements, Systems And Applications*. Taylor & Francis, 1997. [Online]. Available: http://books.google.fi/books?id=pJGjwwQ4-DsC

[85] R. Harrington, *Field Computation by Moment Methods*, ser. IEEE/OUP Series on Electromagnetic Wave Theory. Oxford University Press, USA, 1993. [Online]. Available: http://books.google.fi/books?id=IwRRAAAAMAAJ

[86] E. W. Weisstein, "Green's Function," MathWorld – A Wolfram Web Resource. [Online]. Available: http://mathworld.wolfram.com/GreensFunction.html

[87] J. Mäkitalo, S. Suuriniemi, and M. Kauranen, "Boundary element method for surface nonlinear optics of nanoparticles," *Opt. Express*, vol. 19, no. 23, pp. 23 386–23 399, Nov 2011. [Online]. Available: http://www.opticsexpress.org/abstract.cfm?URI=oe-19-23-23386

[88] M. Schøeyn, "Pre-Gutenberg Printing," The Schøeyn Collection. [Online]. Available: http://www.schoyencollection.com/pre1450.html

[89] J. Viheriälä and T. Niemi and, J. Kontio and Markus Pessa, *Nanoimprint Lithography - Next Generation Nanopatterning Methods for Nanophotonics Fabrication, Recent Optical and Photonic Technologies*. http://www.intechopen.com/books/recent-optical-and-photonic-technologies/nanoimprint-lithography-next-generation-nanopatterning-methods-for-nanophotonics-fabrication InTech, 2010.

[90] K. Haring, J. Viheriälä, M. Viljanen, J. Paajaste, R. Koskinen, S. Suomalainen, A. Laakso, K. Leinonen, T. Niemi, and M. Guina, "Laterally-coupled distributed feedback ingasb/gasb diode lasers fabricated by nanoimprint lithography," *Electronics letters*, vol. 46, no. 16, pp. 1146–1147, 2010.

[91] J. Tommila, A. Tukiainen, J. Viheriälä, A. Schramm, T. Hakkarainen, A. Aho, P. Stenberg, M. Dumitrescu, and M. Guina, "Nanoimprint lithography patterned gaas templates for site-controlled inas quantum dots," *Journal of Crystal Growth*, vol. 323, no. 1, pp. 183–186, 2011.

[92] J. Viheriälä, T. Niemi, J. Laukkanen, M. Karjalainen, and M. Pessa, "Large-area nanoperforated sin membranes for optical and mechanical filtering," *Microelectronic Engineering*, vol. 87, no. 5, pp. 1620–1622, 2010.

[93] J. Viheriälä, T. Niemi, J. Kontio, T. Rytkönen, and M. Pessa, "Fabrication of surface reliefs on facets of single mode optical fibres using nanoimprint lithography," *Electronics Letters*, vol. 43, no. 3, pp. 150–151, 2007.

[94] M. D. Austin, W. Zhang, H. Ge, D. Wasserman, S. A. Lyon, and S. Y. Chou, "6 nm half-pitch lines and 0.04 μm^2 static random access memory patterns by nanoimprint lithography," *Nanotechnology*, vol. 16, no. 8, p. 1058, 2005. [Online]. Available: http://stacks.iop.org/0957-4484/16/i=8/a=010

[95] E. Delamarche, H. Schmid, B. Michel, and H. Biebuyck, "Stability of molded polydimethylsiloxane microstructures," *Advanced Materials*, vol. 9, no. 9, pp. 741–746, 1997. [Online]. Available: http://dx.doi.org/10.1002/adma.19970090914

[96] M.-R. Viljanen, "Advanced processing methods for laterally corrugated DFB - laser diodes," Master's thesis, Tampere University of Technology, Tampere, October 2010.

[97] K. Owen, B. VanDerElzen, R. Peterson, and K. Najafi, "High aspect ratio deep silicon etching," in *Micro Electro Mechanical Systems (MEMS), 2012 IEEE 25th International Conference on*, 29 2012-feb. 2 2012, pp. 251–254.

[98] M. M. Kincaid, "Investigation of a roll-to-roll nanoimprinting process utilizing inkjet based resist deposition," Ph.D. dissertation, The University of Texas, Austin, 2011.

[99] H. Hiroshima, "Nanoimprint with thin and uniform residual layer for various pattern densities," *Microelectronic Engineering*, vol. 86, no. 4, pp. 611–614, 2009.

[100] "mr-UVCur21+mr-UVCur06 Overview," micro resist technology GmbH, Köpenicker Straße 325, 12555 Berlin-Köpenick, Germany. [Online].

Available: http://www.microresist.de/produkte/polymere_nil/pdf/uvcur21_06_mr_08092301_en_ls.pdf

[101] D. F. Spicer, A. C. Rodger, and G. L. Varnell, "Computer controlled pattern generating system for use with electron-beam writing instruments," *Journal of Vacuum Science and Technology*, vol. 10, no. 6, pp. 1052–1055, 1973. [Online]. Available: http://link.aip.org/link/?JVS/10/1052/1

[102] G. L. Varnell, D. F. Spicer, and A. C. Rodger, "E-beam writing techniques for semiconductor device fabrication," *Journal of Vacuum Science and Technology*, vol. 10, no. 6, pp. 1048–1051, 1973. [Online]. Available: http://link.aip.org/link/?JVS/10/1048/1

[103] M. Hatzakis, "Electron resists for microcircuit and mask production," *Journal of The Electrochemical Society*, vol. 116, no. 7, pp. 1033–1037, 1969. [Online]. Available: http://link.aip.org/link/?JES/116/1033/1

[104] V. R. Manfrinato, L. L. Cheong, H. Duan, D. Winston, H. I. Smith, and K. K. Berggren, "Sub-5 keV electron-beam lithography in hydrogen silsesquioxane resist," *Microelectronic Engineering*, vol. 88, no. 10, pp. 3070–3074, 2011. [Online]. Available: http://www.sciencedirect.com/science/article/pii/S016793171100520X

[105] M. Manheller, S. Trellenkamp, R. Waser, and S. Karthäuser, "Reliable fabrication of 3 nm gaps between nanoelectrodes by electron-beam lithography," *Nanotechnology*, vol. 23, no. 12, p. 125302, 2012. [Online]. Available: http://stacks.iop.org/0957-4484/23/i=12/a=125302

[106] J. P. Spallas, A. M. Hawryluk, and D. R. Kania, "Field emitter array mask patterning using laser interference lithography," *Journal of Vacuum Science and Technology B: Microelectronics and Nanometer Structures*, vol. 13, no. 5, pp. 1973–1978, sep 1995.

[107] H. Wolferen and L. Abelmann, *Laser Interference Lithography*. Nova Publishers, 2011.

[108] "International Technology Roadmap for Semiconductors - Lithography." [Online]. Available: http://www.itrs.net/Links/2011ITRS/2011Chapters/2011Lithography.pdf

[109] M. Emons, K. Obata, T. Binhammer, A. Ovsianikov, B. Chichkov, and U. Morgner, "Two-photon polymerization technique with sub-50 nm resolution by sub-10 fs laser pulses," *Optical Materials Express*, vol. 2, no. 7, pp. 942–947, 2012.

[110] S. Tarutani, H. Tsubaki, and S. Kanna, "Development of materials and processes for double patterning toward 32 nm node ArF immersion lithography," *Journal of Photopolymer Science and Technology*, vol. 21, no. 5, pp. 685–690, 2008.

[111] C. Wagner and N. Harned, "EUV]ithography: Lithography gets extreme," *Nat Photon*, vol. 4, no. 1, pp. 24–26, jan 2010. [Online]. Available: http://dx.doi.org/10.1038/nphoton.2009.251

[112] T. Chang, M. Mankos, K. Y. Lee, and L. P. Muray, "Multiple electron-beam lithography," *Microelectronic Engineering*, vol. 57–58, no. 0, pp. 117–135, 2001, micro- and Nano-Engineering 2000. [Online]. Available: http://www.sciencedirect.com/science/article/pii/S0167931701005287

[113] B. Lin, "Future of multiple-e-beam direct-write systems," in *SPIE Advanced Lithography*. International Society for Optics and Photonics, 2012, pp. 832 302–832 302.

[114] L. Giannuzzi and N. University, *Introduction to Focused Ion Beams: Instrumentation, Theory, Techniques and Practice*. Springer, 2004. [Online]. Available: http://books.google.fi/books?id=h1sM6iwg4-wC

[115] Wanzenboeck, Heinz D and Waid, Simon, *Focused Ion Beam Lithography, Recent Advances in Nanofabrication Techniques and Applications*. InTech, 2011. [Online]. Available: http://cdn.intechopen.com/pdfs/24490/InTech-Focused_ion_beam_lithography.pdf

[116] K. Ariga, J. P. Hill, M. V. Lee, A. Vinu, R. Charvet, and S. Acharya, "Challenges and breakthroughs in recent research on self-assembly," *Science and Technology of Advanced Materials*, vol. 9, no. 1, p. 014109, 2008. [Online]. Available: http://stacks.iop.org/1468-6996/9/i=1/a=014109

[117] H. Soh, K. Guarini, and C. Quate, *Scanning Probe Lithography*, ser. Microsystems (Series). Springer, 2001. [Online]. Available: http://books.google.fi/books?id=uTJWCN_LEeQC

[118] "AR-P 631 ... 679 datasheet," ALLRESIST GmbH, Am Biotop 14, 15344 Strausberg, Germany. [Online]. Available: http://www.allresist.de/wMedia/pdf/wEnglish/produkte_ebeamresist/AR-P631_679.pdf

[119] "LOR/PMGI Data Sheet," MicroChem Corp., 90 Oak St. Newton, MA 02464, USA. [Online]. Available: http://microchem.com/pdf/RevPMGI-Resists-data-sheetV-rhcedit-100311.pdf

[120] V. Stout and M. Gibbons, "Gettering of gas by titanium," *Journal of applied physics*, vol. 26, no. 12, pp. 1488–1492, 1955.

[121] C. A. Spindt, I. Brodie, L. Humphrey, and E. R. Westerberg, "Physical properties of thin-film field emission cathodes with molybdenum cones," *Journal of Applied Physics*, vol. 47, no. 12, pp. 5248–5263, 1976. [Online]. Available: http://link.aip.org/link/?JAP/47/5248/1

[122] M. IslamRaja, M. Cappelli, J. McVittie, and K. Saraswat, "A 3-dimensional model for low-pressure chemical-vapor-deposition step coverage in trenches and circular vias," *Journal of applied physics*, vol. 70, no. 11, pp. 7137–7140, 1991.

[123] D. R. Lide, *Optical Properties of Selected Elements*, ser. CRC Handbook of Chemistry and Physics. Boca Raton, Florida: Taylor & Francis, 2010.

[124] A. Fuchs, M. Bender, U. Plachetka, L. Kock, N. Koo, T. Wahlbrink, and H. Kurz, "Lithography potentials of UV-nanoimprint," *Current Applied Physics*, vol. 8, no. 6, pp. 669–674, 2008. [Online]. Available: http://www.sciencedirect.com/science/article/pii/S1567173907001174

[125] G. Spoldi, S. Beuer, M. Rommel, V. Yanev, A. Bauer, and H. Ryssel, "Experimental observation of FIB induced lateral damage on silicon samples," *Microelectronic Engineering*, vol. 86, no. 4, pp. 548–551, 2009.

[126] C. J. Mogab, A. C. Adams, and D. L. Flamm, "Plasma etching of si and SiO_2 – the effect of oxygen additions to CF_4 plasmas," *Journal of Applied Physics*, vol. 49, no. 7, pp. 3796–3803, 1978. [Online]. Available: http://link.aip.org/link/?JAP/49/3796/1

[127] M. Lindblom, J. Reinspach, O. von Hofsten, M. Bertilson, H. M. Hertz, and A. Holmberg, "High-aspect-ratio germanium zone plates fabricated by reactive ion etching in chlorine," *Journal of Vacuum Science and Technology B: Microelectronics and Nanometer Structures*, vol. 27, no. 2, pp. L1–L3, 2009. [Online]. Available: http://link.aip.org/link/?JVB/27/L1/1

[128] J. Telkkälä, J. Viheriälä, A. Aho, P. Melanen, J. Karinen, M. Dumitrescu, and M. Guina, "Narrow linewidth laterally-coupled 1.5 μm DFB lasers fabricated using nanoimprint lithography," *Electronics Letters*, vol. 47, no. 6, pp. 400–401, 2011. [Online]. Available: http://link.aip.org/link/?ELL/47/400/1

[129] "Acetone Material Safety Data Sheet," OneMed Oy, PL 10, Metsäläntie 20, 00321 Helsinki. [Online]. Available: www.tamro.fi/TS_ktt.nsf/($All)/2D431D145F1E09CFC2256F200042EC5F/$File/ASETONI.PDF

[130] "Microposit Remover 1165 data sheet," Shipley Company, 455 Forest St. Marlborough, Massachusetts 01752. [Online]. Available: www.first.ethz.ch/infrastructure/Chemicals/Photolithography/Data_Remover1165.pdf

[131] H. Aouani, J. Wenger, D. Gérard, H. Rigneault, E. Devaux, T. Ebbesen, F. Mahdavi, T. Xu, and S. Blair, "Crucial role of the adhesion layer on the plasmonic fluorescence enhancement," *ACS nano*, vol. 3, no. 7, pp. 2043–2048, 2009.

[132] C. A. Goss, D. H. Charych, and M. Majda, "Application of (3-mercaptopropyl)trimethoxysilane as a molecular adhesive in the fabrication of vapor-deposited gold electrodes on glass substrates," *Analyti-*

cal Chemistry, vol. 63, no. 1, pp. 85–88, 1991. [Online]. Available: http://pubs.acs.org/doi/abs/10.1021/ac00001a018

[133] T. G. Habteyes, S. Dhuey, E. Wood, D. Gargas, S. Cabrini, P. J. Schuck, A. P. Alivisatos, and S. R. Leone, "Metallic adhesion layer induced plasmon damping and molecular linker as a nondamping alternative," *ACS Nano*, vol. 6, no. 6, pp. 5702–5709, 2012. [Online]. Available: http://pubs.acs.org/doi/abs/10.1021/nn301885u

[134] J. Chen, G. Smolyakov, S. Brueck, and K. Malloy, "Surface plasmon modes of finite, planar, metal-insulator-metal plasmonic waveguides," *Optics Express*, vol. 16, no. 19, pp. 14 902–14 909, 2008.

[135] C. A. Spindt, "A thin-film field-emission cathode," *Journal of Applied Physics*, vol. 39, no. 7, pp. 3504–3505, 1968. [Online]. Available: http://link.aip.org/link/?JAP/39/3504/1

[136] H. Mimura, "The status of field emission displays," in *Vacuum Electronics Conference, 2007. IVEC'07. IEEE International*. IEEE, 2007, pp. 1–4.

[137] Q. Zhan, "Cylindrical vector beams: from mathematical concepts to applications," *Adv. Opt. Photon*, vol. 1, no. 1, pp. 1–57, 2009.

[138] T. Corrigan, P. Kolb, A. Sushkov, H. Drew, D. Schmadel, and R. Phaneuf, "Optical plasmonic resonances in split-ring resonator structures: an improved lc model," *Optics Express*, vol. 16, no. 24, pp. 19 850–19 864, 2008.

[139] C. Rockstuhl, F. Lederer, C. Etrich, T. Zentgraf, J. Kuhl, and H. Giessen, "On the reinterpretation of resonances in split-ring-resonators at normal incidence," *Optics express*, vol. 14, no. 19, pp. 8827–8836, 2006.

[140] A. Kudelski, "Raman studies of rhodamine 6G and crystal violet sub-monolayers on electrochemically roughened silver substrates: Do dye molecules adsorb preferentially on highly SERS-active sites?" *Chemical physics letters*, vol. 414, no. 4, pp. 271–275, 2005.

[141] J. Tommila, V. Polojärvi, A. Aho, A. Tukiainen, J. Viheriälä, J. Salmi, A. Schramm, J. Kontio, A. Turtiainen, T. Niemi, *et al.*, "Nanostructured broadband antireflection coatings on AlInP fabricated by nanoimprint lithography," *Solar Energy Materials and Solar Cells*, vol. 94, no. 10, pp. 1845–1848, 2010.

[142] W. Guter, J. Schone, S. Philipps, M. Steiner, G. Siefer, A. Wekkeli, E. Welser, E. Oliva, A. Bett, and F. Dimroth, "Current-matched triple-junction solar cell reaching 41.1% conversion efficiency under concentrated sunlight," *Applied Physics Letters*, vol. 94, no. 22, pp. 223 504–223 504, 2009.

[143] P. B. Clapham and M. C. Hutley, "Reduction of Lens Reflexion by the "Moth Eye" Principle," *Nature*, vol. 244, pp. 281–282, 1973.

[144] T.-P. Ngo, M. E. Kurdi, X. Checoury, P. Boucaud, J. F. Damlencourt, O. Kermarrec, and D. Bensahel, "Two-dimensional photonic crystals with germanium on insulator obtained by a condensation method," *Applied Physics Letters*, vol. 93, no. 24, p. 241112, 2008. [Online]. Available: http://link.aip.org/link/?APL/93/241112/1

[145] C. Mateus, M. Huang, L. Chen, C. Chang-Hasnain, and Y. Suzuki, "Broad-band mirror (1.12–1.62 μm) using a subwavelength grating," *Photonics Technology Letters, IEEE*, vol. 16, no. 7, pp. 1676–1678, july 2004.

[146] T. Saastamoinen, T. Alasaarela, A. Lehmuskero, I. Vartiainen, N. Heikkilä, and M. Kuittinen, "Resonance waveguide reflectors with semi-wide bandwidth at the visible wavelengths," *Optics express*, vol. 19, no. 3, pp. 2126–2132, 2011.

[147] C. Mateus, M. Huang, Y. Deng, A. Neureuther, and C. Chang-Hasnain, "Ultrabroadband mirror using low-index cladded subwavelength grating," *Photonics Technology Letters, IEEE*, vol. 16, no. 2, pp. 518–520, 2004.

[148] K. Kobayashi, "Development of infrared transmitting glasses," *Journal of Non-Crystalline Solids*, vol. 316, no. 2–3, pp. 403–406, 2003. [Online]. Available: http://www.sciencedirect.com/science/article/pii/S0022309302019075

[149] R. Paschotta, "Vertical external-cavity surface-emitting lasers," RP Photonics Consulting GmbH, Waldstr. 17, 78073 Bad Dürrheim, Germany. [Online]. Available: http://www.rp-photonics.com/vertical_external_cavity_surface_emitting_lasers.html

[150] S. Giet, C. Lee, S. Calvez, M. Dawson, N. Destouches, J. Pommier, and O. Parriaux, "Stabilization of a semiconductor disk laser using an intra-cavity high reflectivity grating," *Optics express*, vol. 15, no. 25, pp. 16 520–16 526, 2007.

P1

Publication1

J.M. Kontio, H. Husu, J. Simonen, M.J. Huttunen, J. Tommila, M. Pessa, and M. Kauranen, "Nanoimprint fabrication of gold nanocones with ~10 nm tips for enhanced optical interactions," *Optics Letters* , Vol. 34, No. 14, pp. 1979-1981, 2009

Nanoimprint fabrication of gold nanocones with ~10 nm tips for enhanced optical interactions

Juha M. Kontio,[1,*] Hannu Husu,[2] Janne Simonen,[1] Mikko J. Huttunen,[2] Juha Tommila,[1] Markus Pessa,[1] and Martti Kauranen[2]

[1]Optoelectronics Research Centre, Tampere University of Technology, FIN-33101 Tampere, Finland
[2]Department of Physics, Optics Laboratory, Tampere University of Technology, FIN-33101 Tampere, Finland
*Corresponding author: juha.kontio@tut.fi

Received March 20, 2009; accepted May 8, 2009;
posted May 27, 2009 (Doc. ID 108985); published June 24, 2009

We show that nanoimprint lithography combined with electron-beam evaporation provides a cost-efficient, rapid, and reproducible method to fabricate conical nanostructures with very sharp tips on flat surfaces in high volumes. We demonstrate the method by preparing a wafer-scale array of gold nanocones with an average tip radius of 5 nm. Strong local fields at the tips enhance the second-harmonic generation by over 2 orders of magnitude compared with a nonsharp reference. © 2009 Optical Society of America

OCIS codes: 220.4241, 190.2620.

Metal nanostructures are under intense investigation especially in the fields of plasmonics [1] and metamaterials [2]. They act as optical antennas [3], which couple light between the near and the far fields, allowing light to be manipulated beyond the diffraction limit. The resulting strong nanoscale electromagnetic fields can enhance optical interactions, such as surface-enhanced Raman scattering [4]. The nanoscale localization of light arises from plasmon resonances of metal nanoparticles and can be further enhanced by nanoscale gaps between particles [5]. In addition, sharp tips can lead to very strong local fields through geometrical effects (lightning rod effect) [6], which has many applications in tip-enhanced near-field microscopy [7], sensing [8], and nanofocusing of light [9]. Strong local fields are particularly important for nonlinear optical interactions, which scale with a high power of the fields, as demonstrated by second-harmonic generation (SHG) from nanodimers [10], sharp tips [7,11], four-wave mixing [12], and high-harmonic generation [13]. Sharp metallic tips are also in wide use outside optics acting as efficient Spindt-type electron emitters [14], for example, in the emerging applications of surface conduction electron emitter displays (SED) [15].

It is challenging to fabricate metal nanostructures reproducibly over large areas while maintaining good structural quality. Individual particles can be made by focused ion beam (FIB) milling and two-dimensional particle arrays by electron-beam (e-beam) induced deposition, but the sample dimensions are limited by reasonable lithography time to 0.1–1 mm. Both methods have also been used to demonstrate conical structures with sharp tips (nanocones), but the processing is slow and quite expensive [16]. Conical shapes can also be prepared by self-assembly and etching [17] or by nanotransfer printing [18]. These methods do not simultaneously produce truly sharp features (i.e., a few nanometer tip radii) and allow accurate control of the placement of the particles. Sharp low aspect ratio nanostructures have been produced by a soft lithography-based approach [19], but the shape is limited to pyramids because of the crystallographic etching in mold fabrication.

In this Letter, we show that UV-nanoimprint lithography (UV-NIL), combined with e-beam evaporation, can overcome the problems of other fabrication techniques. Our method enables the fabrication of large arrays of gold nanocones with sharp 10 nm scale tips, good structural quality, and high reproducibility. The technique is fast and relatively cheap and provides accurate control of the particle positions. We characterize the nanocones by extinction spectroscopy, which identifies a plasmon resonance along the cone axis and SHG, which verifies the existence of a strong local field polarized along the cone axis.

We prepared arrays of conical gold nanocones of 130 nm base diameter, organized in a square array with a cone-to-cone period of 300 nm (Fig. 1). A master template with a lattice of cylindrical holes was first prepared by laser-interference lithography (LIL) (AMO GmbH) on a silicon wafer. The nanopatterns on the master were copied to a stamp made of poly(dimethylsiloxane) (PDMS). A fused-silica wafer used as a substrate was coated with a 600 nm polymethyl methacrylate (PMMA) film and a germanium intermediate layer, followed by spin coating of a thin nanoimprint lithography (NIL) resist layer (Amonil, AMO GmbH). The nanoimprinting was performed by an EVG 620 mask aligner using a PDMS stamp [Fig. 2(a)]. Reactive ion etching (RIE) was then used to etch through the lift-off structure to expose the substrate and to form deep cylindrical holes in the resist

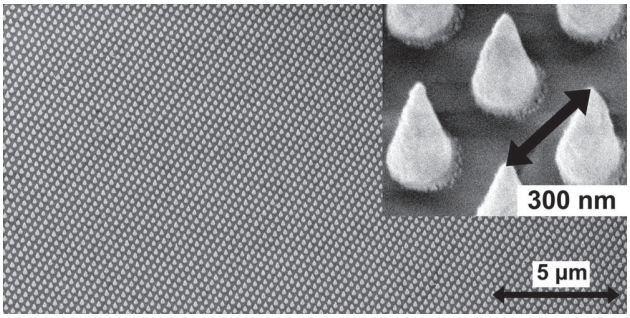

Fig. 1. Array of gold nanocones with a period of 300 nm, a base diameter of 130 nm, and an average cone height of 291 nm on a fused-silica substrate.

0146-9592/09/131979-3/$15.00

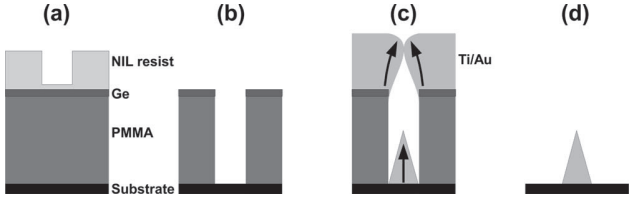

Fig. 2. Fabrication principle. (a) The lift-off structure. The top layer is the NIL patterned resist layer. (b) Etching by RIE to expose the substrate. (c) Metal evaporation. Arrows mark the growth direction. (d) After lift-off in acetone.

mask [Fig. 2(b)]. The metal layers forming conical nanostructures were defined by depositing titanium adhesion (10 nm) and gold (300 nm) layers in an e-beam evaporator until the holes in the resist mask were completely filled with gold [Fig. 2(c)]. Finally, lift-off was applied in acetone using ultrasonic agitation [Fig. 2(d)].

In traditional lift-off processes the gold patterns would have vertical sidewalls similar to those of the mask. Therefore one would expect to grow cylindrical nanorods, but this did not occur in our case. The holes in the resist mask were narrow (130 nm diameter) and deep (600 nm), giving them a high aspect ratio. The structures grew conically because the top of the hole shrank in diameter during gold evaporation, similar to the process for Spindt-type emitters [14]. Owing to mutual collisions, the gold atoms arrived at the sample from slightly different directions during evaporation. Thus, the atoms tended to stick on the top edge of the hole rather than the bottom edge of the hole, leading to the preferred deposition to the center part of the bottom. The end result was that the particle grew sharper during the deposition until the hole was completely covered with gold as shown in Fig. 2(c).

The shape of the gold nanocones was verified by an atomic force microscope (AFM) (not shown) and a field-emission scanning electron microscope (FESEM) (Fig. 1). The yield of an unoptimized nanocone process was approximately 95% on a 4 cm^2 area, which consisted of 4.4×10^9 nanocones. The size of the patterned area is only limited by the size of the NIL stamp and could be as large as 150 mm.

The main advantages of our process arise from the use of NIL. After the initial master pattern is produced, for example, by expensive electron-beam lithography (EBL), it can be replicated hundreds of times cost effectively. Compared with EBL, our NIL-based process is superior in time and repeatability. Moreover, the final cone height, together with sharpness, may be accurately controlled contrary to nanotransfer printing [18]. Our method is also less damaging than FIB milling. The most damaging process step for the substrate in our method is the O_2 etching of the PMMA layer in RIE. This is an advantage if nanocones are to be prepared, for example, over compound semiconductor quantum wells. Furthermore, FIB is not suitable for large-volume production. The disadvantage of our method compared with FIB is that the deposited gold structures are grainy, unlike features produced by removing material from bulk metal. However, in many applications the metal structures will in any case be deposited on a substrate, so our cones will be of similar quality.

To identify the plasmon resonance of the nanocones, we measured their extinction spectrum using a fiber-optic spectrometer for wavelengths from 450 to 950 nm. For TE polarization the spectra are featureless in this range. However, for TM polarization and at oblique angle of incidence, a strong resonance is located at 615 nm [Fig. 3(a)]. This result, therefore, suggests that the resonance is associated with the longitudinal particle plasmon of the cone, which oscillates along the cone axis.

To demonstrate the strong local fields at the tips of the cones, we utilized optical SH generation with an ultrafast pulsed Nd:glass laser (wavelength of 1060 nm, pulse length of 200 fs, repetition rate of 82 MHz). Note that the fundamental wavelength is nonresonant with the plasmon peak, but the second-harmonic (SH) wavelength of 530 nm is rather close to the resonance. The diameter of the focal spot in the experiment was about 3 μm, so there were approximately 80 nanocones within the spot area. The SH signal was detected by a photomultiplier tube combined with a single-photon counting system. To couple the incident beam with the direction of the cone axis, a polarization component along this direction is needed. A simple way to do this is to tilt the sample away from normal incidence. However, this can lead to two problems. First, because the array is periodic, a propagating diffraction order appears for the SH wavelength at a certain angle of incidence. Second, the incident field can also couple to off-diagonal components of the nonlinear response because of polarization components in the plane of the sample, complicating the analysis. These problems are avoided by using a focused radially polarized fundamental beam, which has a strong longitudinal electric field component at the focal plane, while the lateral polarization components cancel each other. Simulations using the finite-element method (Comsol) show that this situation leads to a strongly enhanced field [white area in Fig. 3(b)] at the cone tip.

To quantify the enhancement of the SH response from the nanocones, we had as a reference sample a

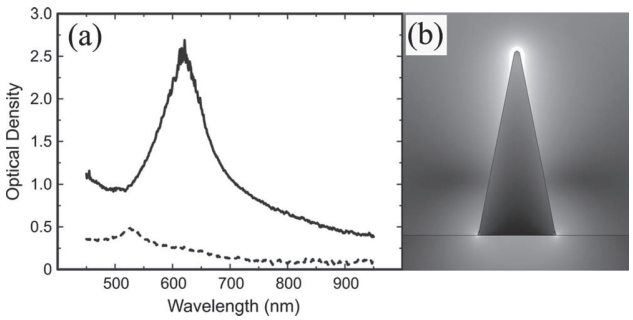

Fig. 3. (a) Extinction spectra for TM-polarized light at 50° angle of incidence for nanocones with (solid curve) and without (dashed curve) sharp tips. (b) A 3D finite-element simulation of electric field distribution in a gold nanocone with a 5 nm tip radius of curvature, illuminated from above by a focused radially polarized beam at 1060 nm wavelength. The scale is logarithmic and is cropped at 85% for better visibility.

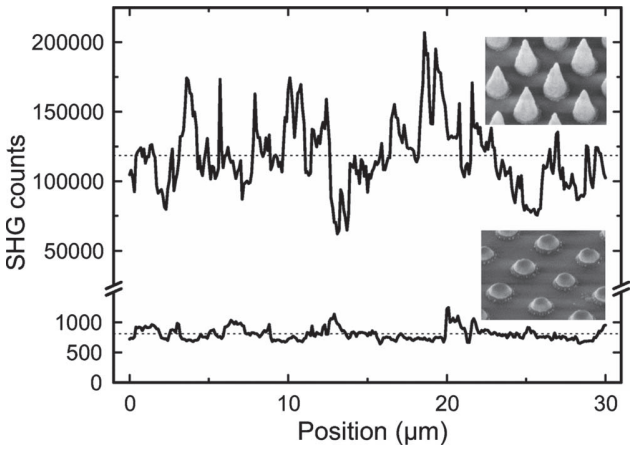

Fig. 4. SHG signal as the sample is scanned in transverse direction. The measurement is done for sharp nanocones, with a height of 291 nm, and half-cones, with a height of 88 nm. Dashed lines illustrate the average SHG intensities.

similar array of half-cones with 88 nm height. The reference thus lacks the sharp tip. Its longitudinal plasmon is shifted to a slightly shorter wavelength of 525 nm [Fig. 3(a)]. Therefore our reference sample is actually closer to the two-photon resonance with our laser than the sample with sharp tips.

Figure 4 presents the SH signals from the two samples as they were scanned in a transverse direction in the focal plane. There is a significant fluctuation in the SH signal for the sharp nanocones, whereas the signal from the reference sample is more uniform. This is significant because the measured signals represent averages over about 200 individual cones. During the scan nanocones are moving into and out of the focal area. The SH signal is therefore very sensitive to the SH response of single nanocones. Such sensitivity arises from the fact that the SH intensity is proportional to the fourth power of the local fundamental field and to the second power of the local SH field. Thus, even small differences in the features of the individual cones and of their local fields can lead to large differences in SH signals. To quantify the enhancement, we averaged the SH signals over the whole transverse scan. The SH intensity from the sample with sharp nanocones was enhanced by a factor of 150 compared with the half-cones. Clearly, sharp nanocones are efficient in producing high local electric fields.

In conclusion, we have shown that nanoimprint lithography enables cost-effective fabrication of large-area arrays of gold nanocones. Gold evaporation into deep holes spontaneously forms nanocones with good reproducibility, uniformity, and sharp tips. We have also shown, using SHG, that the nanocones enhance local electric fields polarized along the cone axis. Such structures could prove useful in applications where a large number of regularly spaced sharp nanotips are needed, such as plasmonic sensors, nanoemitters, nanofocusing, and metamaterials.

This work is supported by the Academy of Finland (projects 114913 and 123109), the Finnish Funding Agency for Technology and Innovation (project 40149/08), and the Finnish Ministry of Education (The Research and Development Project on Nanophotonics). Timo Lehto is acknowledged for technical help in optical measurements. J. M. Kontio and H. Husu acknowledge the graduate school of the Tampere University of Technology. J. M. Kontio also acknowledges the Vilho, Yrjö, and Kalle Väisälä Foundation and the Emil Aaltonen Foundation for financial support.

References

1. S. A. Maier and H. A. Atwater, J. Appl. Phys. **98**, 011101 (2005).
2. V. M. Shalaev, Nat. Photonics **1**, 41 (2006).
3. K. B. Crozier, A. Sundaramurthy, G. S. Kino, and C. F. Quate, J. Appl. Phys. **94**, 4632 (2003).
4. K. Kneipp, Y. Wang, H. Kneipp, L. T. Perelman, I. Itzkan, R. R. Dasari, and M. S. Feld, Phys. Rev. Lett. **78**, 1667 (1997).
5. A. Sundaramurthy, K. B. Crozier, G. S. Kino, D. P. Fromm, P. J. Schuck, and W. E. Moerner, Phys. Rev. B **72**, 165409 (2005).
6. L. Novotny and B. Hecht, *Principles of Nano-Optics* (Cambridge U. Press, 2006).
7. A. Bouhelier, M. Beversluis, A. Hartschuh, and L. Novotny, Phys. Rev. Lett. **90**, 013903 (2003).
8. B. Knoll and F. Keilmann, Nature **399**, 134 (1999).
9. D. K. Gramotnev, M. W. Vogel, and M. I. Stockman, J. Appl. Phys. **104**, 034311 (2008).
10. B. Canfield, H. Husu, J. Laukkanen, B. Bai, M. Kuittinen, J. Turunen, and M. Kauranen, Nano Lett. **7**, 1251 (2007).
11. S. Takahashi and A. V. Zayats, Appl. Phys. Lett. **80**, 3479 (2002).
12. M. Danckwerts and L. Novotny, Phys. Rev. Lett. **98**, 026104 (2007).
13. S. Kim, J. Jin, Y. Kim, I. Park, Y. Kim, and S. W. Kim, Nature **453**, 757 (2008).
14. C. A. Spindt, I. Brodie, L. Humphrey, and E. R. Westerberg, J. Appl. Phys. **47**, 5248 (1976).
15. H. Mimura, in *IEEE International Vacuum Electronics Conference (IVEC) 2007* (2007), pp. 1–4.
16. F. De Angelis, G. Das, C. Liberale, F. Mecarini, M. Matteucci, and E. Di Fabrizio, Microelectron. Eng. **85**, 1286 (2007).
17. C. Hsu, S. T. Connor, M. X. Tang, and Y. Cui, Appl. Phys. Lett. **93**, 133109 (2008).
18. T. Kim, J. Kim, S. Son, and S. Seo, Nanotechnology **19**, 295302 (2008).
19. T. W. Odom, J. C. Love, D. B. Wolfe, K. E. Paul, and G. M. Whitesides, Langmuir **18**, 5314 (2002).

Publication2

P2

J.M. Kontio, J. Simonen, J. Tommila, and M. Pessa, "Arrays of metallic nanocones fabricated by UV-nanoimprint lithography," *Microelectronic Engineering*, Vol. 87, No. 9, pp. 1711-1715, 2010

Arrays of metallic nanocones fabricated by UV-nanoimprint lithography

Juha M. Kontio*[,a], Janne Simonen[a], Juha Tommila[a], Markus Pessa[a]

[a] *Optoelectronics Research Centre, Tampere University of Technology, P.O. Box 692, FIN-33101, Tampere, Finland*

Abstract

We introduce a novel method for fabricating nanocones of various metals. Based on a combination of UV-nanoimprint lithography and electron beam evaporation, the method enables fast, high volume, and reproducible fabrication of conical nanostructures on flat substrates. We investigate cone formation with eight different metals and find that the shape of the cone depends on the material characteristics of the deposited metal.

Key words: , nanocone, cones, gold, optical antenna, nanoimprint lithography, second-harmonic generation, field emission

1. Introduction

Metallic nanostructures are under intense investigation for plasmonics [1] and metamaterials [2]. Nanostructures with sharp features efficiently localize electromagnetic fields, producing very strong local field intensities in the nanoscale through plasmon resonances and geometrical effects (a so-called lightning rod effect) [3]. Since 1960's, Spint-type field emitters have ex-

*Corresponding author
Email address: juha.kontio@tut.fi (Juha M. Kontio)

ploited sharp conical metal structures for the efficient emission of electrons [4]. In plasmonics, sharp metallic structures can act as nanoscale antennas [5]. The localization of electromagnetic fields is beneficial for many applications, such as a tip-enhanced near-field microscopy [6, 7], sensing [8, 9] and nano-focusing of light [10]. Moreover, an interesting commercial application of metal nanotips is SED (surface conduction electron emitter) flat displays where Spindt-type emitters are used [11]. Nanocones and -tips can also be used to create superhydrophobic surfaces [12].

Despite decades of work in this area, the fabrication of sharp metallic nanostructures remains challenging. One of the main problems is achieving high quality structures. Individual particles can readily be made by focused ion beam milling (FIB), whereas two-dimensional arrays of particles can be prepared by electron-beam lithography (EBL), though the sample dimensions usually remain small, $0.1 - 1$ mm in size. EBL is not suited for large-volume fabrication because of long patterning times. FIB and electron-beam induced deposition have been employed to demonstrate conical structures with sharp tips (nanocones), but the process is slow and quite expensive [13]. In addition, conical shapes can be prepared by self-assembly and etching [14] or by nano-transfer printing [15]. These methods do not produce truly sharp features (i.e., a few nanometer tip radii) and they do not simultaneously allow for an accurate control of the placement of the particles.

In this paper we show that UV-nanoimprint lithography (UV-NIL) combined with e-beam evaporation can be used to fabricate large arrays of nanocones out of various metals. The method is relatively simple, low-cost, versatile, and scalable, and it works on flat surfaces. The fabrication prin-

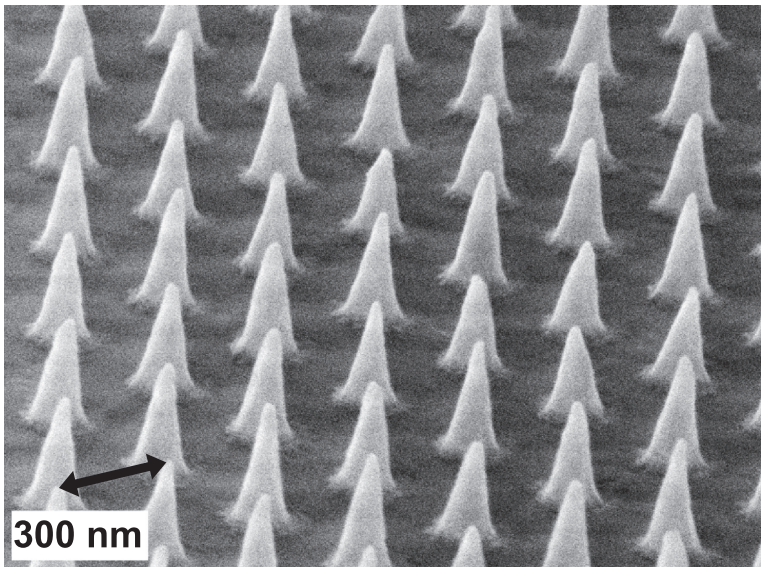

Figure 1: An array of gold nanocones on a silicon substrate. The period is 300 nm, the cone base diameter is 130 nm, and the average height is 257 nm (Ti/Au 20/230 nm).

ciple is similar to what is used for Spindt-type emitters [4] but to the best of our knowledge such structures have never been demonstrated by means of UV-NIL.

The paper is organized as follows. We shall first describe the the fabrication method, followed by an analysis of the cone formation process. We then compare the characteristics of the structures of various metals and conclude with ideas of possible applications.

2. Fabrication

We fabricated regular arrays of conical metal nanoparticles; i.e.nanocones, which were 130 nm in base diameter, organized in a square grid with a 300 nm period from eight different metals by UV-NIL.

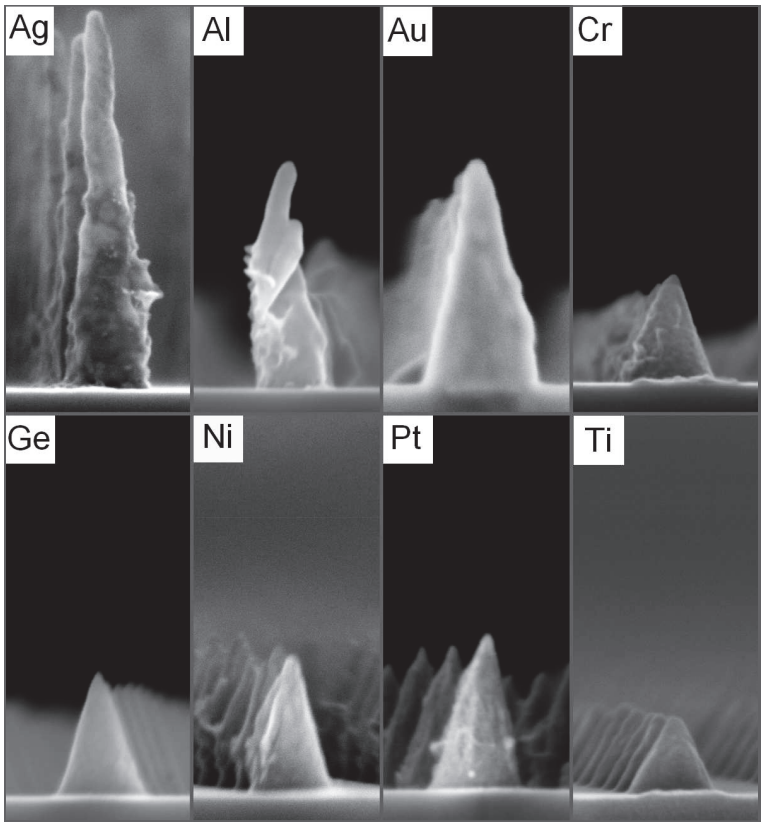

Figure 2: Nanocones of different metals. The SEM photos are taken at the same magnification in order to facilitate the comparison.

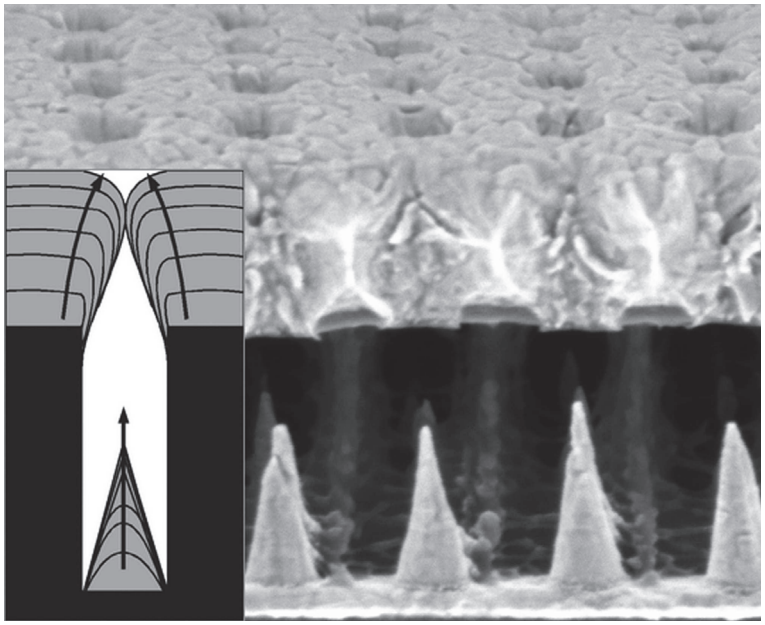

Figure 3: An SEM image of a sectional view of the structure upon gold evaporation before lift-off. The conical shape is formed spontaneously when the holes in the mask shrink during evaporation (inset). The arrows mark the growth direction of the Au layer.

We used UV-NIL and reactive ion etching to replicate a pattern of cylindrical holes into a thick resist layer. The holes had a high aspect ratio, which is an essential feature here. Then we deposited a metal layer by e-beam evaporation, until the holes were filled-up. After lift-off, instead of having an array of cylindrical metal nanorods that might be expected, we obtained an array of nanocones.

A master template having a 2D-lattice of cylindrical holes was prepared by laser-interference lithography (LIL) on a silicon wafer. The nanopatterns on this master template were copied to a transparent elastomer stamp made of poly(dimethylsiloxane) (PDMS). The silicon substrate was spin-coated

with a 600 nm layer of polymethyl methacrylate (PMMA) and baked on a hotplate at 170 °C for 90 seconds. This sacrificial PMMA layer was needed for the successful lift-off step because of the properties of the NIL resist. Although the sidewalls of imprinted patterns were vertical, the NIL resist proved very hard to remove from the substrate by usually used solvents (like acetone).

Next, a 20 nm thick Ge layer was deposited by electron beam evaporation, serving as an etch-stop layer for improving the controllability of the etching steps and preventing intermixing of the UV-NIL and PMMA resist layers. A thin layer of UV-NIL resist (Amonil from Amo GmbH) was then spun over the Ge layer. Nanoimprinting was carried out by an EVG 620 mask aligner using the PMDS stamp. Following imprinting, reactive ion etching with a CHF_3/Ar-based plasma chemistry was utilized to etch through both the NIL resist and Ge layer, and the PMMA layer was subsequently etched anisotropically with an O_2 plasma, exposing the substrate.

The conical shape of the nanocones was defined through metal deposition of a titanium adhesion layer (10 nm), followed by the evaporation of the metal investigated. The adhesion layer was used for each metal studied to ensure a comparable reference surface. The metals were Ti, Cr, Pt, Ni, Ge (a metalloid), Au, Ag, and Al. The evaporation rate was constant 2.5 Å/s, and the chamber pressure after evaporation of the Ti reference was about 10^{-8} mbar. During deposition, the pressure was 10^{-7} mbar for all metals, except for Ni, for which the pressure was 10^{-5} mbar. Our e-beam evaporator chamber was water-cooled during the evaporation and heated during venting to avoid moisture condensation on the chamber walls. The deposition was

continued until the holes in the resist mask were completely filled with metal.

Finally, a lift-off process was performed in an acetone bath using ultrasonic agitation. After this step we observed an array of metallic nanocones on the substrate (Fig. 1).

The shape and quality of the nanocones was investigated by an atomic force microscope (AFM) and a field-emission scanning electron microscope (FE-SEM) (Fig. 2). The yield of the nanocone process was approximately 95% over an area of 4 cm^2 which consisted of 4.4×10^9 nanocones. The only limiting factor for the area was the size of the stamp used in the process. One of the advantages of our process is the easy scalability to larger wafers simply by adjusting process parameters (mainly in dry etching). Also, the cone dimensions are scalable, depending only on the pattern size in the NIL master mould.

3. Formation of nanocones

Since the produced metal pattern in traditional lift-off processes is identical to the shape of the mask, one could expect to have an arrays nanorods, and not nanocones. In our method, the holes in the resist mask were both narrow (130 nm in diameter) and deep (600 nm), giving rise to a high aspect ratio. The conical shape of the pattern derived from the shrinkage of the top of the hole during metal evaporation [16]. Due to mutual collisions, the metal atoms arrived at the sample from slightly different directions. This effect produced lens-shaped metal particles instead of particles of uniform thicknesses. However, the metal also covered the edges of the hole, preferring the top edge and leading to the shrinkage of the top of the hole. The

end result was that the deposited particle grew sharper until the hole was completely covered with metal (see the inset of Fig. 3). If the holes were deep enough, the tip of the cone would not touch the metal layer covering the resist, making the lift-off process possible.

A problem in lift-off was the damage caused by metal flakes to the cones in the ultrasonic bath. The flakes were heavy enough to detach the nanocones as they hit the wafer surface in ultrasonic agitation. This problem was solved by a tape that is used in wafer dicing. The evaporated metal layer was peeled off the top of the lift-off structure aided by the dicing tape. A N_2 blow was used to attach the tape as gently as possible to the metallized surface. The tape removed over 90% of the evaporated metal from the nanopatterned wafer before the ultrasonic bath, and significantly improved the overall yield of the process.

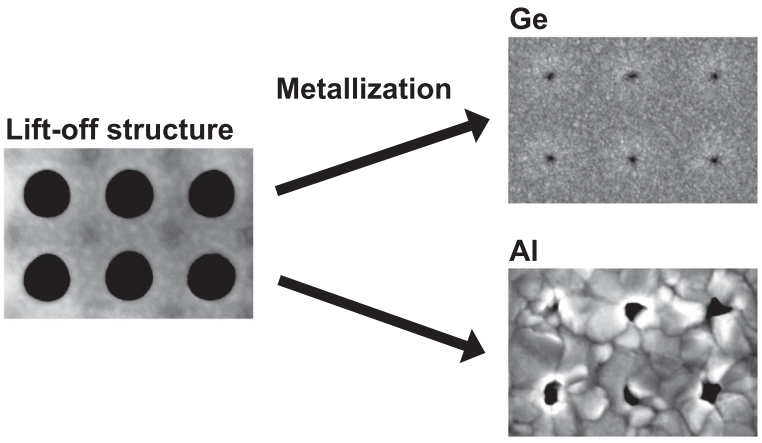

Figure 4: SEM pictures from an etched lift-off structure in RIE before and after metallization. The surface of the Ge sample is less grainy after evaporation than the Al sample. The period of the holes is 300 nm.

Fig. 2 shows SEM images of nanocones fabricated with eight different metals. It is obvious that the height and quality of the cones strongly depended on the material. The dimensions and other details are shown in Table 1.

Material	Evaporated	h nm (AFM)	h nm (SEM)	Aspect ratio	Hole status
Ag	1000	446-645	530-603	4.3	Open
Al	350	181-325	251-354	1.9	Open and closed
Au	400	295	281-335	2.4	Open
Cr	300	160	159-172	1.2	Closed
Ge	350	186-190	186-195	1.5	Closed
Ni	300	233	217-239	1.8	Closed
Pt	300	253	243-246	1.9	Closed
Ti	225	111	123-131	0.9	Closed

Table 1: Parameters of nanocones for different metals. SEM and AFM were used to define the heights. The hole status refers to the hole in the resist mask upon metal evaporation – an open hole means that depositing additional metal to the cone would have been possible.

The gold nanocones were reasonably high (aspect ratio ≈ 2.4) and their uniformity was good. The horizontal cross-sections of the cones were circular. These cones could be useful in plasmonic applications because of their high conductance at visible frequencies. Another often used metal in plasmonics is silver which formed the highest nanocones (aspect ratio ≈ 4.3) but the height uniformity was the poorest of all the materials, due to grain formation which caused irregular shrinkage of the hole in the mask. This could be clearly seen after evaporation of Ag when most of the etched holes were still open but the hole diameter varied substantially. Moreover, silver is soft, and the cones

bent easily during processing.

Aluminum formed the largest grains during its evaporation, yielding polygonal holes (Fig. 4). Because of this the Al cones were highly non-uniform. Uniformity was also a problem with chromium but for a different reason. Cr formed small cones (aspect ratio ≈ 1.2) which were circular and symmetric, but the yield was poor because the Cr layer peeled off and started to roll up on top of the resist mask during evaporation. The Cr layer was so strained after solidification that it ripped the intermediate germanium layer off the PMMA layer. This could become a serious problem in large arrays of Cr patterns.

Similarly to Cr, the Ge cones were relatively small (aspect ratio ≈ 1.5) but the quality and uniformity was the best of all the materials. Ge metalloid is an interesting material for the infrared spectral range, due to its very high refractive index. Conical photonic crystals could be realized using our Ge process. Ge is neither transparent nor metallic in the visible band but could be coated, for example by Au, to achieve high-quality metallic nanocones. Nickel also formed good nanocones with reasonable uniformity. The magnetic properties of Ni, combined with the property of nanocones to localize light, could be interesting in metamaterial applications.

Platinum formed sharp cones of average height (aspect ratio ≈ 1.9). Platinum could be useful in inert probe tips, an area where titanium cones could also be used. Ti formed the smallest cones, and being a very strong material might excel in applications where mechanical durability is an issue. Ti could also be used to shrink the hole-size during the cone process to form "hat-like" cones with an intermediate Ti layer, for example, with Au.

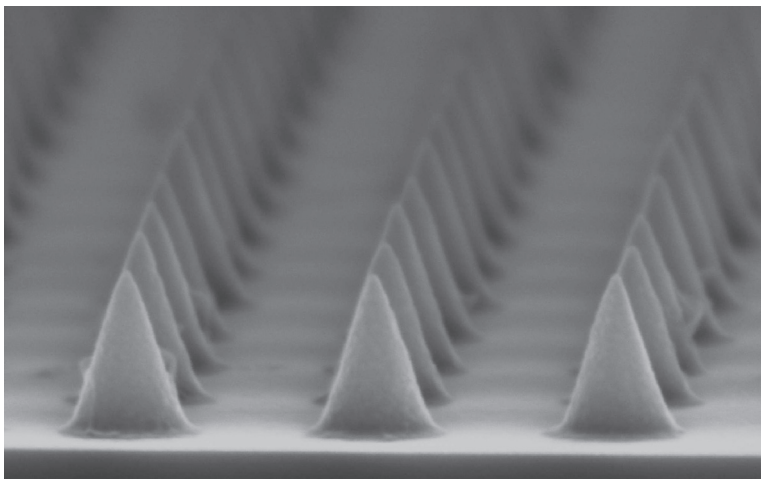

Figure 5: An Array of Ge nanocones. The height and shape of the cones is the most uniform for all of the tested metals.

The sharpness of the cone depended on the evaporated material, because a material with good adhesion to the etched lift-off structure defines a shrinkage-rate of the hole in the mask. The same process also defines the final height of the cone. If the hole shrank slowly, the resulting cone would be tall and sharp. Silver produced the tallest cones, with an aspect ratio of about 4.5 (Table 1).

The uniformity of the cone height was directly proportional to the grain size of a metal film after evaporation. The grain size was characteristic of every material studied and was the main challenge for our method. Not only did grainy metals grow into irregularly shaped grainy cones, but also covered the holes non-uniformly, leading to wide variations in height of the cones. Aluminum was a prime example of this effect (Fig. 4). The same problem was also observed for silver, but the circular shape of the cones was less distorted. However, the high aspect ratio of the Ag cones caused

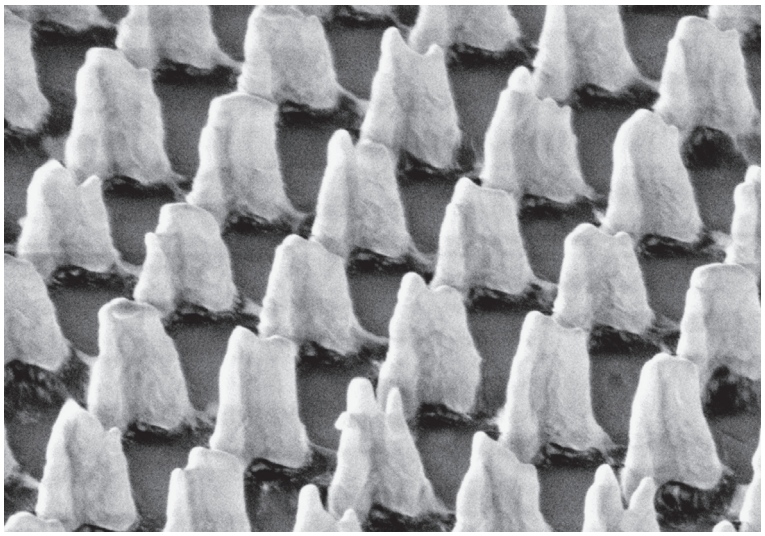

Figure 6: Conical nanostructures formed from L-shaped patterns. Cones grow higher at the corner of L because the line width of the etched hole is wider there so that the hole shrinks slower during metal evaporation yielding higher structure. The period of these structures is 400 nm.

considerable non-uniformity in cone heights. With germanium the grains were very small (Fig. 4) resulting in uniform and symmetric nanocones (Fig. 5). With chromium, the limiting factor for uniformity was the peeling of the metal layer during evaporation. This could be avoided by determining a critical thickness of Cr for peeling. In the SEM micrographs (not shown) the Cr layer was seen to peel off the Ge intermediate layer from the PMMA. The adhesion between Ge and PMMA was poor, as expected. The PMMA layer could be replaced by another, harder material to alleviate this problem.

4. Discussion

The main advantages of our nanocone fabrication method come from the use of UV-NIL. Upon producing the initial master pattern, for example by expensive EBL, the pattern could be replicated hundreds of times cost-effectively. Moreover, the cones could be made of different metals or a combination of metals. Using UV-NIL arrays of nanocones can cover wafers large as 6 inches [17] which are widely used in silicon industry. We also demonstrated high-quality cones from germanium, a metalloid, which is very interesting for its high ($n > 4$) refractive index in the infrared.

With dielectric materials (results not shown) our process did not produce nanocones, but formed structures that resembled hemispherical dots. In principle, any material that could be deposited by e-beam evaporation or other deposition techniques may be used. The final cone height and sharpness can be accurately controlled by the evaporation rate and time. It is possible to fabricate multi-layered cones from any e-beam vaporizable material. One application could be metal-insulator-metal (MIM) nanostructures. Also, nanocones with various height could be prepared at the same time if the patterned holes had different diameters. Large holes will shrink slowly, resulting in higher cones when compared to the holes with small diameters. The base of the cone need not to be circular in cross-section - any shape of a resist groove will grow into a conical structure. For example, consider Fig. 6, which depicts conical patterns formed from an L-shaped hole covered with Au. Our method causes less damage to the substrate than does FIB etching [18]; the most damaging step is an O_2 plasma RIE etching step. Plasmonics benefits from our method because the process is simple, and UV-NIL enables

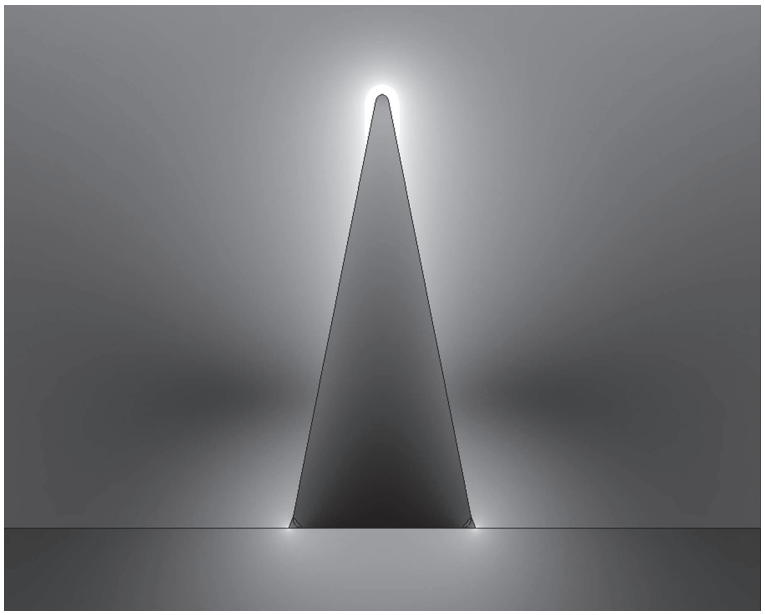

Figure 7: A 3D finite-element simulation of the electric field distribution in a gold nanocone with a 5 nm tip radius of curvature, illuminated from the top by a focused radially polarized beam at the wavelength of 1060 nm. The electric field (in logarithmic scale and cropped at 85% for better visibility) is strongly lozalized at the tip of the cone.

exact replication of desired nanopatterns in a fast and reproducible way.

A disadvantage of our method compared to FIB is that the deposited metal structures are always grainy. However, in many applications, metal structures are deposited directly onto a substrate, so that our cones will be of a similar quality.

As mentioned above, sharp metallic tips are desired for plasmonics, as they produce high enhancement of optical fields in the nanoscale, due to particle plasmon resonances and the lightning rod effect. Fig 7 shows a calculated 3D finite-element simulation of the electric field distribution in a gold nanocone when illuminated from the top by radially polarized light. The

electric field concentrates strongly on the tip. In essence, the cone acts as a nanoscale antenna. The lighting rod effect enables strong coupling of light to the nanoparticle. Possible applications for arrays of conical metal structures include plasmonic sensors, nanoemitters, nanofocusing, and metamaterials. We have started to investigate optical properties of our samples in greater detail and have already presented results on highly enhanced second-harmonic generation [19].

5. Conclusion

In conclusion, we have shown that UV-NIL allows for the fabrication of arrays of metal nanocones cost-effectively in large volumes. In most cases metal evaporation into deep holes spontaneously formed nanocones with good reproducibility, uniformity and sharp tips, although the shape of the nanocone depended strongly on the properties of the evaporated metal. The results suggested that the nanocones could prove useful in applications where a large number of regularly spaced nanotips are needed.

6. Acknowledgments

This work was supported by the Finnish Funding Agency for Technology and Innovation (project 40149/08, Nanophotonics - Extension), and the Ministry of Education of Finland (The Research and Development Project on Nanophotonics). J. Kontio acknowledges the graduate school of the Tampere University of Technology. J. Kontio also acknowledges the Emil Aaltonen Foundation, the Jenny and Antti Wihuri Foundation, and the Vilho, Yrjö

and Kalle Väisälä Foundation for financial support. J. Simonen acknowledges the support of the Academy of Finland (project 123109, A-PLAN).

References

[1] S.A. Maier, and H.A. Atwater, "Plasmonics: Localization and guiding of electromagnetic energy in metal/dielectric structures," J. Appl. Phys. **98,** 011101 (2005).

[2] V.M. Shalaev, "Optical negative-index metamaterials," Nature Photonics **1,** 41 (2006).

[3] L. Novotny, and B. Hecht, *Principles of Nano-optics*, (Cambridge University Press 2006).

[4] C. A. Spindt, "A Thin-Film Field-Emission Cathode," J. Appl. Phys. **39,** 3504 (1968)

[5] Issue "Antennas for Light," Nature Photonics **4,** 199 (2008)

[6] A. Bouhelier, M. Beversluis, A. Hartschuh, and L. Novotny, "Near-field Second-harmonic Generation Induced by Local Field Enhancement," Phys. Rev. Lett. **90,** 013903 (2003).

[7] E.J. Sánchez, L. Novotny, and X.S. Xie, "Near-Field Fluorescence Microscopy Based on Two-Photon Excitation with Metal Tips," Phys. Rev. Lett. **82,** 4014 (1999).

[8] B. Knoll, and F. Keilmann, "Near-field probing of vibrational absorption for chemical microscopy," Nature **399,** 134 (1999).

[9] D. Yelin, D. Oron, S. Thiberge, E. Moses, and Y. Silberberg, "Multiphoton plasmon-resonance microscopy," Opt. Express **11,** 1385 (2003).

[10] D.K. Gramotnev, M.W. Vogel, and M.I. Stockman, "Optimized nonadiabatic nanofocusing of plasmons by tapered metal rods," J. Appl. Phys. **104,** 034311 (2008)

[11] H. Mimura, "The Status of Field Emission Displays," Vacuum Electronics Conference IVEC '07, IEEE International (2007)

[12] C. Choi, and C. Kim, "Large Slip of Aqueous Liquid Flow over a Nanoengineered Superhydrophobic Surface," Phys. Rev. Lett. **96,** 066001 (2006)

[13] F. De Angelis, Gobind Das, C. Liberale, F. Mecarini, M. Matteucci, and E. Di Fabrizio, "Fabrication and characterization of plasmonic nanolens for applications in biophotonics," Microelectronic Engineering **85,** 1286 (2008).

[14] C. Hsu, S.T. Connor, M.X. Tang, and Y. Cui, "Wafer-scale silicon nanopillars and nanocones by LangmuirBlodgett assembly and etching," Appl. Phys. Lett. **93,** 133109 (2008).

[15] T. Kim, J. Kim, S. Son, and S. Seo, "Gold nanocones fabricated by nanotransfer printing and their application for field emission," Nanotechnology **19,** 295302 (2008).

[16] C. A. Spindt, I. Brodie, L. Humphrey, and E.R Westerberg, "Physical properties of thin-film field emission cathodes with molybdenum cones," J. Appl. Phys. **47,** 5248 (1976).

[17] A. Fuchs, M. Bender, U. Platchetka, L.Koch, N. Koo, T. Wahlbrink, and H. Kurz, "Lithography potentials of UV-nanoimprint," Current Applied Physics **8,** 669 (2008).

[18] G. Spoldi, S. Beuer, M. Rommel, V. Yanev, J. Bauer and H. Ryssel, "Experimental observation of FIB induced lateral damage on silicon samples," Microelectronic Engineering (2009), 10.1016/j.mee.2009.01.003.

[19] J.M. Kontio, H. Husu, J. Simonen, M. Huttunen, J. Tommila, M. Pessa, and M. Kauranen, "Nanoimprint fabrication of gold nanocones with $\sim$ 10 nm tip for enhanced optical interactions," Submitted to Optics Letters (2009).

Publication3

P3

J.M. Kontio, J. Simonen, K. Leinonen, M. Kuittinen, and T. Niemi, “ Broadband infrared mirror using guided-mode resonance in sub-wavelength germanium grating,'' *OpticsLetters* ,Vol.35,No.15,pp.2564-2566,2010

Broadband infrared mirror using guided-mode resonance in a subwavelength germanium grating

Juha M. Kontio,[1,*] Janne Simonen,[1] Kari Leinonen,[2,3] Markku Kuittinen,[2] and Tapio Niemi[1]

[1]*Optoelectronics Research Centre, Tampere University of Technology, P.O. Box 692, FIN-33101, Tampere, Finland*

[2]*Department of Physics and Mathematics, University of Eastern Finland, P.O. Box 111, FIN-80101 Joensuu, Finland*

[3]*Currently with the North Karelia Polytechnic, Centre for Business and Engineering, Karjalankatu 3, FIN-80200 Joensuu, Finland*

**Corresponding author: juha.kontio@tut.fi*

Received May 19, 2010; revised June 29, 2010; accepted July 1, 2010; posted July 8, 2010 (Doc. ID 128740); published July 22, 2010

We demonstrate a broadband mirror for the IR wavelength region comprising a subwavelength grating made of germanium. We design and optimize the guided-mode resonances in the structure for TM-polarized incident light by rigorous electromagnetic simulations. The grating structure is realized by nanoimprint lithography and dry etching. The reflectivity of the mirror is over 95% for the wavelength range between 2245 and 3080 nm.

OCIS codes: 050.6624, 310.2790, 130.3060.

Photonics technology is strongly moving into IR wavelengths in several rapidly developing application areas, including spectroscopy, sensors, imaging, telecommunications, and surveillance [1–3]. IR photonics is one of the key technologies in developing optical wireless local-area networks [4]. Common optical IR materials are Al_2O_3, BaF_2, Si, GaAs, Ge, IR grade quartz, NaCl, MgF_2, ZnSe, and ZnS. Of these, Si, GaAs, and Ge are the most feasible in terms of modern microelectronic device processing.

The miniaturization of photonic components requires integration to other optical devices, such as lasers and mirrors. For example, subwavelength gratings have been used as cavity mirrors in vertical cavity light-emitting diodes. Based on guided-mode resonance (GMR), these fully dielectric gratings can theoretically reflect all incident light, thus replacing thick distributed Bragg reflector mirrors [5,6]. The main idea of a GMR mirror is to create standing waves in a periodic waveguide layer. Reflection takes place when an incident wave couples to waveguide-forming standing waves. These leaky standing waves interact with the waveguide grating and reradiate back the incident wave [7]. The main challenge with pushing the operation regime of GMR mirrors into the IR range is in finding suitable material systems. A high refractive-index contrast and low absorbance are needed to achieve high reflection. Dielectrics do not possess a high enough index of refraction, nor are they usually very easily processable. Many dielectrics, such as calcium fluoride (CaF_2), are also fragile. Several semiconductors have a high index of refraction in the IR, but their deposition is not always straightforward, i.e., lattice matched III–V semiconductors cannot be epitaxially grown on top of fused silica or silicon.

In this Letter, we show that germanium is an attractive material for a broadband IR mirror. It has a very high index of refraction of ~4.0 in the IR [8] and a bandgap of 0.66 eV. The absorption of Ge is very small for the wavelengths above the bandgap, and the transmission spectrum extends from 1.9 to over 17 μm, which is a wider range than that of silicon (1.06–6.7 μm). We designed and fabricated a Ge GMR mirror structure and characterized it. Bulk Ge is common window material in the IR region. However, there are only a few reports concerning Ge as a material for micro/nano-optical components in the literature. For example, Ge has recently been used to realize planar photonic crystal structures [9,10]. Previous reports have also demonstrated broadband reflectors fabricated out of silicon [11]. However, mainly low refractive index materials have been used to realize GMR mirrors, resulting in a narrow reflection band.

We designed the grating mirror for TM-polarized light (E-field is perpendicular to the grating lines) using two-dimensional (2D) rigorous coupled-wave analysis (RCWA) [12]. Our RCWA code works in MATLAB, which allows utilizing efficient optimization tools to automatically find the parameters to fulfill the predefined design criteria. The operation range of the mirror was designed to be centered at 2.5 μm, and the Nelder–Mead simplex search method was used to maximize the average reflectivity over a wavelength region of 1900–3000 nm. All of the structural parameters, i.e., period, fill factor, and thickness of the grating, were free in the optimization.

The grating material was amorphous Ge and the substrate was fused silica. For fabrication reasons, a thin layer of silicon nitride (SiNx) was placed between the substrate and the Ge layer in the simulation. Another thin layer of SiNx was added on top of the grating lines to take into account the residual etch mask. The refractive index of SiNx was fixed at 2.0 and the fused silica at 1.44. For the refractive index of Ge, we used data from NASA [13]. The real part of the refractive index varies from 4.17 to 4.03 for wavelengths between 1500 and 3000 nm, respectively. The imaginary part of the refractive index responsible for the absorption in Ge was set to zero at wavelengths over 1750 nm and to 0.03 at 1500 nm in the simulations.

The optimization process led to a design having a period of the grating of 1 μm, a thickness of the Ge layer of 550 nm, and a width of the grating groove of 280 nm (fill factor of 0.72). The effect of the additional SiNx layers on the reflectivity spectrum was negligible. This design resulted in the reflectivity of >95% for the wavelength range between 1850 and 3020 nm. Reflectivities

0146-9592/10/152564-03$15.00/0

approaching 100% could have been achieved by optimizing for a narrower wavelength range.

It is important to analyze the fabrication tolerances before processing the samples. From the simulation results shown in Fig. 1(a), it can be seen that the fill factor can vary from 0.72 to 0.765 while the reflectance remains over 90%. Note that if the fill factor decreases more than 0.01 from the optimum then the reflectivity around a wavelength of 2100 nm starts to reduce rapidly. Similar simulations were done for the Ge layer thickness [see Fig. 1(b)]. The reflectivity stays above 90% with Ge thickness of 506–550 nm.

We fabricated a 3 mm × 3 mm Ge GMR mirror with the parameters obtained from the simulations. A master template was first prepared by electron beam lithography on a silicon wafer. The grating pattern on the master was copied into a nanoimprint lithography (NIL) stamp made of poly(dimethylsiloxane) (PDMS). A fused silica substrate was then coated with a 10 nm SiNx to improve adhesion of the Ge layer using plasma-enhanced chemical vapor deposition (PECVD). After this, a 550-nm-thick Ge layer was deposited by electron beam evaporation. Finally, a 70 nm SiNx layer was deposited by PECVD.

In the next step, 60 nm of NIL resist (mr-UVCur06, Micro Resist Technology GmbH) was spin coated on the sample. The nanoimprinting of the grating pattern was performed with an EVG 620 mask aligner (EV Group GmbH) using the PDMS stamp. Reactive ion etching with O_2 plasma was then used to etch through the residual layer of the NIL resist on the bottom of the grating grooves. A mixture of CHF_3/Ar was used to etch through the SiNx mask layer. Prior to Ge etching, the surface of the sample was cleaned using O_2 plasma to remove possible residuals left from the Freon etching. The Ge layer was then etched in inductively coupled plasma using $SiCl_4/Cl_2$/He chemistry. Our etch recipe produced an almost vertical etch profile with smooth sidewalls.

After the fabrication process, a thin layer (35 nm) of residual SiNx remained on top of the grating lines. It was not removed since, in the simulations, its effect was negligible. The fabricated sample was finally investigated by an atomic force microscope and a field emission scanning electron microscope (Fig. 2). For this figure, the grating was fabricated on Si substrate to achieve a good cross-section image.

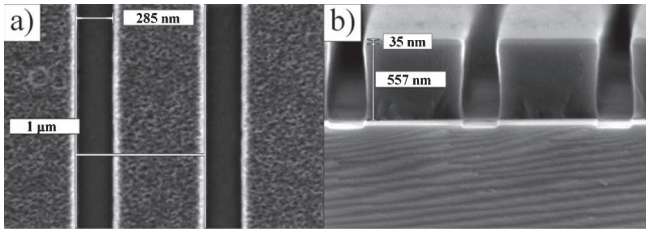

Fig. 2. (a) Ge grating on a fused silica wafer with a 1 μm period and a 285 nm groove width imaged from above. (b) Cross section of the Ge grating on a Si reference wafer. The Ge layer is 557 nm thick, and the residual SiNx etch mask layer is 35 nm thick. The Si wafer was used in a reference sample to enable good cross-section quality for inspection of the etching profile.

The transmittance of the fabricated sample was measured with a Perkin Elmer Lambda 1050 UV/VIS/NIR spectrophotometer. The reflectance was derived from the transmittance, because it was not possible to measure the reflectance in direct incidence with the instrument. The beam size was limited by a shutter to the 3 mm × 3 mm grating area of the sample. An IR-range polarizer was aligned parallel to the grating lines for measurements in TE polarization, and the sample was rotated 90° for measurements of the TM polarization. A silica wafer without a grating was used as a reference sample.

The absorption of the Ge layer was measured from the transmission spectrum of the unpatterned sample referencing a plain fused-silica wafer. It was less than 1% in the designed operating range of the mirror. At the wavelength of 2335 nm, the reflectance (Fig. 3) is at its maximum, reaching 98.8%. In the simulations the reflectance is ideally 99.99% when no absorption has been taken into account. This minor discrepancy can be explained by the small undercut in the grating edge profile [Fig. 2(b)]—the sidewalls in the design were perfectly vertical. We estimated that this undercut decreases the grating effective linewidth by 25 nm and recalculated the reflectance spectra based on this. This simple approximation results in good agreement with the experimental reflectivity spectrum, as can be seen in Fig. 3. The reduced reflectivity at the wavelength of ~2100 nm can be explained by a deviation from the optimum fill factor, as can be seen in Fig. 1(a). The rest of the measurement closely follows the spectrum of the optimal design.

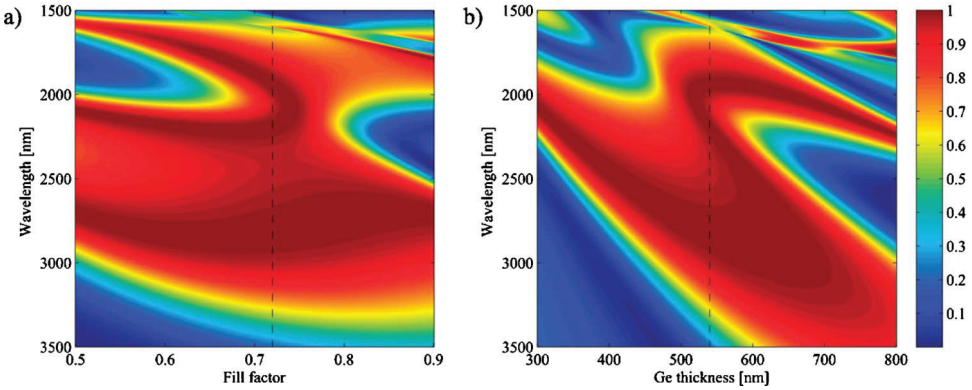

Fig. 1. (Color online) Simulation of the reflectance of the GMR mirror design. Period of the grating design is fixed to 1.0 μm. (a) Effect of changing the fill factor. The thickness of Ge layer is fixed to 550 nm. (b) Effect of Ge film thickness. Fill factor is fixed to 0.72. Dashed lines represent the reflectivity with the optimal operation conditions.

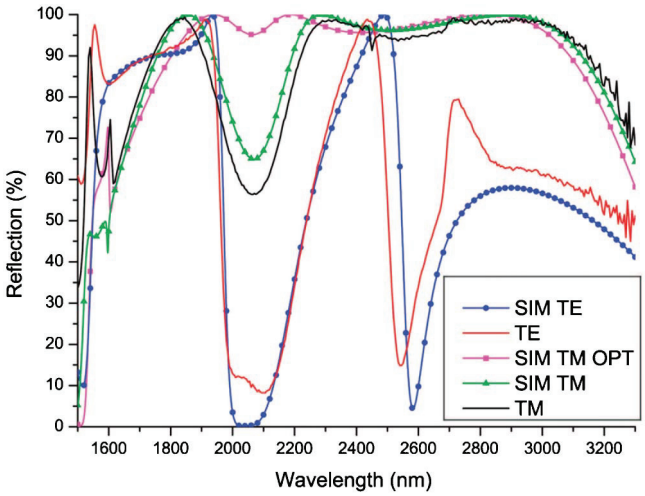

Fig. 3. (Color online) Measured (solid curves) and simulated (dotted curves) reflection spectra of the Ge mirror for TM and TE polarization. The mirror was designed for TM polarization ("SIM TM OPT"). The spectra ("TM" and "TE") were derived from transmission measurements with an IR-spectrophotometer. "SIM TM" and "SIM TE" spectra represent simulated reflectivities for the measured sample with the realized dimensions.

A slight problem in the transmission measurement is introduced by the strong characteristic OH-absorption peak of fused silica at 2.7 μm [14]. Comparing the simulated transmission spectrum with the experimental spectrum, it can be clearly identified that the measured peak at the 2.7 μm is a result of the absorption of the substrate. This absorption peak is missing in the reflectivity spectrum measured from the GMR mirror sample by Fourier transform spectroscopy (FTIR) but was visible in the transmission spectrum of the fused silica substrate. Unfortunately, comprehensive characterization of the GMR mirror with reliable referencing was not possible with the FTIR, because it used a focused measurement beam. In measuring the reflection in direct incidence, an uncollimated beam resulted in unwanted resonances in the GMR mirror structure, because a focused beam always contains components at nonzero incident angles.

One challenge with GMR mirrors has been to find materials having a higher index of refraction than silicon but that still are straightforward to process and highly transparent. Ge has a high index of refraction and low losses in the IR range. This allows the GMR mirrors to be designed for longer wavelengths than previously [11]. The main advantages of Ge are low cost and straightforward processing. Because of its extremely high index of refraction, Ge mirrors can also operate as waveguides on various high-index semiconductors, which is very important for integration. In addition, Ge is a metalloid, which enables the GMR mirror structure to be used as an electrode. This gives versatility for the application designer to combine the Ge mirror with active components, such as lasers. GMR mirror design can be extended to a 2D grating for improved polarization insensitivity [15].

In conclusion, we have shown that Ge can be used to fabricate a broadband GMR mirror in the IR range for TM-polarized light. Because of its ease of fabrication, the mirror can be integrated with any photonic component with a flat surface. The operating region can be adjusted by varying the period, Ge layer thickness, and the fill factor. The substrate material has a strong influence on the operation bandwidth, but the structure can be reoptimized, e.g., for silicon substrates. Ge GMR mirrors may find applications in vertical cavity lasers and other IR-range photonic applications.

This work was supported by the Academy of Finland (projects 123109 and 135084), the Finnish Funding Agency for Technology and Innovation (project 40149/08), and the Finnish Ministry of Education (The Research and Development Project on Nanophotonics). The authors thank Jouni Hiltunen and Noora Heikkinen for IR-spectrophotometer measurements at the InFotonics Center and Joensuu Campus of the University of Eastern Finland and Lassi Rieppo and Arto Koistinen for FTIR measurements at the Biomater Centre in the Kuopio Campus of the University of Eastern Finland. The authors also thank Juha Tommila for NIL stamp fabrication. J. M. Kontio acknowledges the graduate school of the Tampere University of Technology, the Vilho, Yrjö and Kalle Väisälä Foundation, and the Emil Aaltonen Foundation for financial support.

References

1. C. J. Fecko, J. D. Eaves, J. J. Loparo, A. Tokmakoff, and P. L. Geissler, Science **301**, 1698 (2003).
2. Z. Wu, P. E. Powers, A. M. Sarangan, and Q. Zhan, Opt. Lett. **33**, 1653 (2008).
3. Yu. I. Zavadskiĭ, A. S. Skrylev, B. M. Khotyanov, and V. V. Chernokozhin, J. Opt. Technol. **76**, 755 (2009).
4. R. Ramirez-Iniguez, S. M. Idrus, and Z. Sun, *Optical Wireless Communications: IR for Wireless Connectivity* (CRC Press, 2008).
5. M. C. Y. Huang, Y. Zhou, and C. J. Chang-Hasnain, Nat. Photon. **1**, 119 (2007).
6. R. Magnusson and M. Shokooh-Saremi, Opt. Express **16**, 3456 (2008).
7. S. S. Wang and R. Magnusson, Appl. Opt. **32**, 2606 (1993).
8. D. R. Lide, in *CRC Handbook of Chemistry and Physics*, 90th ed., Internet Version (CRC Press, 2010).
9. T.-P. Ngo, M. El Kurdi, X. Checoury, P. Boucaud, J. F. Damlencourt, O. Kermarrec, and D. Bensahel, Appl. Phys. Lett. **93**, 241112 (2008).
10. M. Lindblom, J. Reinspach, O. von Hofsten, M. Bertilson, H. M. Hertz, and A. Holmberg, J. Vac. Sci. Technol. B **27**, L1 (2009).
11. C. F. R. Mateus, M. C. Y. Huang, L. Chen, C. J. Chang-Hasnain, and Y. Suzuki, IEEE Photonics Technol. Lett. **16**, 1676 (2004).
12. M. G. Moharam and T. K. Gaylord, J. Opt. Soc. Am. **71**, 811 (1981).
13. B. J. Frey, D. B. Leviton, and T. J. Madison, Proc. SPIE **6273**, 62732J (2006).
14. K. Kobayashi, J. Non-Cryst. Solids **316**, 403 (2003).
15. A.-L. Fehrembach, A. Talneau, O. Boyko, F. Lemarchand, and A. Sentenac, Opt. Lett. **32**, 2269 (2007).

Publication4

S. Rao, M.J. Huttunen, J.M. Kontio, J. Mäkitalo, M-R. Viljanen, J. Simonen, M. Kauranen, and D. Petrov, ''Tip-enhanced Raman scattering from bridged nanocones," *OpticsExpress,* Vol.18,No.23,pp.23790-23795,2010

P4

Tip-enhanced Raman scattering from bridged nanocones

Satish Rao,[1] Mikko J. Huttunen,[2] Juha M. Kontio,[3] Jouni Makitalo,[2] Milla-Riina Viljanen,[3] Janne Simonen,[3] Martti Kauranen,[2] and Dmitri Petrov,[1,4,*]

[1] *ICFO - Institut de Ciències Fotòniques, Mediterranean Technology Park, 08860 Castelldefels (Barcelona), Spain*
[2] *Department of Physics, Tampere University of Technology, FI-33101 Tampere, Finland*
[3] *Optoelectronics Research Centre, Tampere University of Technology, FI-33101 Tampere, Finland*
[4] *ICREA - Institucio Catalana de Recerca i Estudis Avancats, 08010 Barcelona, Spain*
[*] *Dmitri.Petrov@icfo.es*

Abstract: We present two silver nanocones separated by 450 nm, well beyond the typical gap spacing of coupled nanoantennas, and connected by a metal bridge to facilitate plasmonic coupling between them. The tip-enhanced Raman scattering from crystal violet molecules is found to be almost an order of magnitude higher from the bridged cones than from individual cones. This result is supported by local-field calculations of the two types of structures. The bridged nanocones are easily fabricated by a nanoimprint-based process, thus offering a faster and simpler approach compared to other fabrication techniques.

OCIS codes: (240.6695) Surface-enhanced Raman scattering; (300.6280) Spectroscopy, fluorescence and luminescence; (240.6680) Surface plasmons; (240.3990) Micro-optical devices.

References and links

1. M. Brongersma and V. Shalaev, "The case for plasmonics," Science **328**, 440–441 (2010).
2. X. Hoa, A. Kirk, and M. Tabrizian, "Towards integrated and sensitive surface plasmon resonance biosensors: a review of recent progress," Biosens. Bioelectron. **23**, 151–160 (2007).
3. D. Ward, N. Grady, C. Levin, N. Halas, Y. Wu, P. Nordlander, and D. Natelson, "Electromigrated nanoscale gaps for surface-enhanced Raman spectroscopy," Nano Lett. **7**, 1396–1400 (2007).
4. E. Bailo and V. Deckert, "Tip-enhanced Raman scattering," Chem. Soc. Rev. **37**, 921–930 (2008).
5. T. Yano, P. Verma, Y. Saito, T. Ichimura, and S. Kawata, "Pressure-assisted tip-enhanced Raman imaging at a resolution of a few nanometres," Nat. Photonics **3**, 473–477 (2009).
6. F. Angelis, G. Das, P. Candeloro, P. Maddalena, M. Galli, A. Bek, M. Lazzarino, I. Maksymov, C. Liberale, L. Andreani, and E. Fabrizio, "Nanoscale chemical mapping using three-dimensional adiabatic compression of surface plasmon polaritons," Nat. Nanotechnol. **5**, 67–72 (2010).
7. C. Hsu, S. Connor, M. Tang, and Y. Cui, "Wafer-scale silicon nanopillars and nanocones by Langmuir-Blodgett assembly and etching," Appl. Phys. Lett. **93**, 133109 (2008).
8. J. Kontio, J. Simonen, J. Tommila, and M. Pessa, "Arrays of metallic nanocones fabricated by uv-nanoimprint lithography," Microelectron. Eng. **87**, 1711–1715 (2010).
9. C. Rockstuhl, F. Lederer, C. Etrich, T. Zentgraf, J. Kuhl, and H. Giessen, "On the reinterpretation of resonances in split-ring-resonators at normal incidence," Opt. Express **14**, 8827–8836 (2006).
10. T. Corrigan, P. Kolb, A. Sushkov, H. Drew, D. Schmadel, and R. Phaneuf, "Optical plasmonic resonances in split-ring resonator structures: an improved lc model," Opt. Express **16**, 19850–19864 (2008).
11. I. Mikhailyuk and A. Razzhivin, "Background subtraction in experimental data arrays illustrated by the example of raman spectra and fluorescent gel electrophoresis patterns," Instrum. Exp. Tech. **46**, 765–769 (2003).

#135204 - $15.00 USD Received 17 Sep 2010; revised 21 Oct 2010; accepted 25 Oct 2010; published 27 Oct 2010

12. A. Kudelski, "Raman studies of rhodamine 6G and crystal violet sub-monolayers on electrochemically roughened silver substrates: do dye molecules adsorb preferentially on highly SERS-active sites?" Chem. Phys. Lett. **414**, 271–275 (2005).
13. X. Jiao, J. Goeckeritz, S. Blair, and M. Oldham, "Localization of near-field resonances in bowtie antennae: influence of adhesion layers," Plasmonics **4**, 37-50 (2009).
14. R. Harrington, *Field computation by moment methods* (Wiley-IEEE Press, 1993).
15. C. Geuzaine and J.-F. Remacle, "Gmsh: a three-dimensional finite element mesh generator with built-in pre- and post-processing facilities," Int. J. Numer. Methods Eng. **79**, 1309–1331 (2009).
16. L. Novotny, R. X. Bian, and X. S. Xie, "Theory of nanometric optical tweezers," Phys. Rev. Lett. **79**, 645–648 (1997).
17. X. Ling, L. Xie, Y. Fang, H. Xu, H. Zhang, J. Kong, M. Dresselhaus, J. Zhang, and Z. Liu, "Can graphene be used as a substrate for Raman enhancement?" Nano Lett. **10**, 553–561 (2010).
18. H. Frey, S. Witt, K. Felderer, and R. Guckenberger, "High-resolution imaging of single fluorescent molecules with the optical near-field of a metal tip," Phys. Rev. Lett. **93**, 200801 (2004).

1. Introduction

The plasmonics field has progressed in producing ordered systems that enhance the optical fields applied onto, emitted, and scattered by metal nanostructures [1]. Such structures have the potential to be integrated in to numerous lab-on-a-chip applications such as high throughput analyte detection [2]. The work to date has included various forms of nanoantennas that utilize nanosized gaps between metal structures [3] and metal tips whose apex sizes lie in the range of tens of nanometers. The latter have been studied extensively for tip-enhanced Raman scattering (TERS), a specialized form of surface-enhanced Raman scattering (SERS), where strong local fields at the tip enhance the Raman signal at spatial resolutions on the order of the tip apex size [4]. An advantage of such tip structures is that they offer field enhancement along the third dimension, away from the planar surface, which could be useful for certain lab-on-a-chip and optical trapping applications, for example. Additionally, their position can be accurately controlled as a movable probe when attached to an atomic force microscope (AFM) [5].

The development of high-quality tips has depended on the choice of metal and patterning processes. For example, focused ion-beam milling (FIB) and electron-beam lithography (EBL) have produced nanocones, however, the processes are complicated, slow, and expensive [6]. Various forms of self-assembly and etching techniques [7] have also been employed although they fail to achieve similar tip sharpness when compared to FIB and EBL techniques. We have recently demonstrated a fast and robust method for constructing reproducible nanocone structures by utilizing UV-nanoimprint lithography (UV-NIL) combined with electron-beam evaporation [8].

With the nanocones in hand, previous efforts have attempted, with success, to further improve the field enhancing capability of these structures. For example, single cones made from silicon based materials were used with a deposited thin layer of metal to facilitate the plasmon effects [5]. Another successful method attached a single nanocone, constructed by FIB, to a photonic crystal cavity [6]. The system was constructed to couple the excitation light to the surface plasmons in the nanocone via surface plasmon polaritons, which led to the observation of Raman signal from a single chemical monolayer. Although signal enhancements have been achieved, the processes to construct such devices require multiple steps which can prove to be costly when a chip of structures is needed.

In this paper, we demonstrate a simple approach to prepare bridged nanocones with sharp tips that outperform single nanocones in terms of the achievable Raman signal enhancement. Two silver nanocones are connected by a silver bridge that overcomes the relatively large separation distance to achieve plasmon coupling between the two cones. The structure is intended to mimic the planar "U-shaped" split-ring-resonator (SRR) where plasmon coupling between two arms is facilitated through a base wire [9, 10]. Additionally, the sharp tips at the ends of the arms are

#135204 - $15.00 USD Received 17 Sep 2010; revised 21 Oct 2010; accepted 25 Oct 2010; published 27 Oct 2010

shown to be favorable for the field enhancement effects.

2. Methods

The method used for the single nanocone fabrication has been studied and reported previously [8]. Briefly, a master template having a lattice of both cylindrical holes (single nanocones) and connected hole pairs (bridged nanocones) was first prepared by EBL on a silicon wafer. The resulting nanopatterns were then copied to a transparent elastomer stamp made of poly(dimethylsiloxane) (PDMS). A glass substrate with thickness of 180 μm was spin-coated with 800 nm of polymethyl methacrylate (PMMA) and baked on a hotplate at 170° C for 2 min. Next, a 20 nm thick Ge layer was deposited by electron-beam evaporation, serving as an etch-stop layer for improving the controllability of the etching steps and preventing intermixing of NIL and PMMA resist layers. A thin layer of NIL resist (Amonil from Amo GmbH) was then spun over the Ge layer followed by nanoimprinting with an EVG 620 mask aligner using the PMDS stamp. Following imprinting, reactive ion etching with a CHF3/Ar based plasma chemistry was utilized to etch through the NIL resist and Ge layers. The PMMA layer was subsequently etched anisotropically with O_2 plasma, exposing the substrate. Note that the final structure does not contain Ge, which could significantly modify the plasmonic properties of the fabricated structure.

The conical shape of the nanocones was defined through metal deposition of a titanium adhesion layer (20 nm) followed by evaporation of 1000 nm of silver. In principle, any metal could be used, however, we choose silver due to its natural resonances around our excitation wavelength and the ability to obtain high aspect ratios with the material in order to realize concentrated fields far away from the glass surface. The conical shape is formed spontaneously when the holes in the mask shrink during the evaporation. The deposition was continued until the holes in the resist mask were completely filled with metal. The connecting bridge between the cones also forms spontaneously during the evaporation of the metal and contains small spikes due to grain formation. This grain formation is also a limiting factor of the overall quality of the nanocones. A lift-off process was performed in an acetone bath using ultrasonic agitation resulting in an array of metallic nanocones on the substrate. The quality of the structures was verified by field-emission scanning electron microscope (FE-SEM) (Fig. 1).

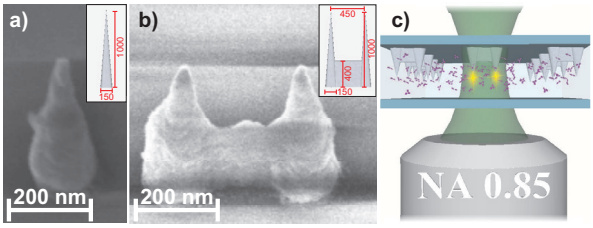

Fig. 1. FE-SEM images of the single (a) and bridged (b) nanocones structures with drawings depicting their dimensions included (insets). An illustration (c) of the orientation of the cones in the experimental setup is also given.

Each cone had a base diameter of 150 nm and a height of approximately 1 μm with a final tip radius of curvature of approximately 5 nm. The array period of the single cones was 1 μm. The bridged nanocone structures were made up of two cones separated by 450 nm and connected with the metal bridge in an array of the same periodicity as the single cones. The bridge was 50 nm wide and 330 nm in height. We concluded this to be a safe geometry where the bridge is short enough such that the cone tips remain active while being large enough to avoid producing any additional local fields in the bridge itself. As a control, single nanocones with an array

#135204 - $15.00 USD Received 17 Sep 2010; revised 21 Oct 2010; accepted 25 Oct 2010; published 27 Oct 2010

period of 450 nm were also constructed and tested in order to mimic a pair of cones in the absence of a bridge.

For the experiments, the cones were immersed in an aqueous solution of crystal violet (CV) (10^{-6}M) by placing drops of the solution on top of the cones and then enclosing the system with a second coverslip. The construct was held by a custom made sample holder before being placed on a microscope stage. The excitation beam (532 nm at 9 mW) was incident normal to the glass surface with the cones inverted such that the beam passed through the tip before the base (Fig. 1c). Similar to the SRR, we expect maximum fields to be produced with an excitation polarization parellel to the bridge, and so, we keep the polarization fixed in this direction for all experiments. The emission from the cones was collected in the backscattered direction through the same objective (60× NA = 0.85) that passes the excitation beam. The backscattered light was passed to a spectroscopic confocal detection system. The acquisition time for all spectra was 1 s.

3. Raman emission enhancement by nanocone structures

A comparison of the emitted signals from the structures in the presence of CV molecules is given in Fig. 2. The Raman and fluorescence bands of the CV molecules are clearly observed

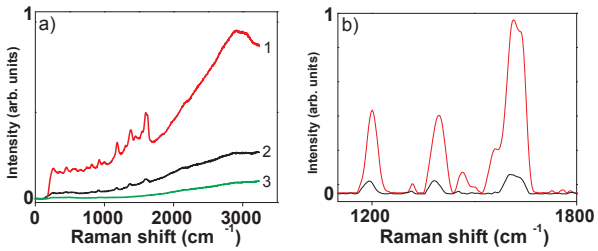

Fig. 2. (color online) a) The emission spectra for the bridged nanocones (1) and single nanocone (2) in the presence of CV. The background signal (3), obtained by measuring from a point in the solution away from the cones, is given. b) The resulting Raman bands after the CV fluorescence background has been removed demonstrating the TERS enhancement improvement of the bridged nanocones (red) compared to the single nanocone (black).

and at this dye concentration, no Raman signal and a low fluorescence signal above noise was observed at the same excitation power in the absence of nanocones. The broad emission peak at 2900 cm^{-1} (630 nm) is the main fluorescence band of CV and acts as background for the CV Raman spectrum. The fluorescence background is removed using an established method [11] in order to further distinguish the Raman bands (Fig. 2b). The three main peaks, at 1200, 1400, and 1615 cm^{-1}, agree with previous observations of the CV SERS spectrum [12].

The bridge clearly alters the optical properties of the system leading to a 4-fold increase in the fluorescence output from the single nanocone. The TERS enhancement is even higher: the three main CV peaks experience an average 8-fold Raman intensity increase relative to the single nanocone. Finally, the control structures, single nanocones at a period of 450 nm, produced spectra (data not shown) nearly identical to the single cone, thus further solidifying the positive effect of the bridge.

4. Local field analysis

The mechanisms for the differing enhancements of the Raman and fluorescence emission will be discussed later, however, both are a consequence of the local fields produced by the optically

#135204 - $15.00 USD Received 17 Sep 2010; revised 21 Oct 2010; accepted 25 Oct 2010; published 27 Oct 2010

excited structures. Thus, in order to facilitate the comparison, we conducted simulations to obtain the local electric field amplitude distributions for three structures: single cone, two cones separated by 450 nm, and the bridged nanocones structure. Due to the large structure height and similarity of the refractive indices of water and glass, the presence of the substrate and thin Ti adhesion layer were neglected. The absorption of Ti may, though, cause small decrease and shift of the resonances as estimated in [13]. We adopted the frequency domain method of moments (MOM) [14] where a focused beam was used as the input field. The surface mesh of the nanocone was generated with the free software Gmsh [15]. The input polarization of the beam was set to be linear and parallel to the plane of the cones and the focusing conditions matched those of the experiment. The focal field distribution was calculated using vector diffraction theory.

The results of the field calculations are presented in Fig. 3. The improved performance of

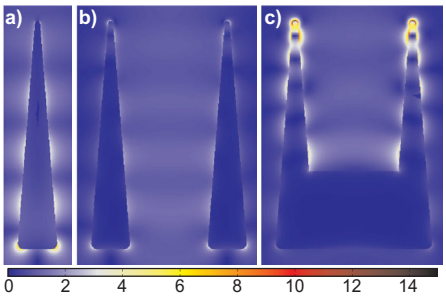

Fig. 3. Local field amplitude distribution simulations for three structures: single nanocone (a), two nanocones separated by 450 nm (b), and the bridged nanocones structure (c). The amplitudes were normalized to the maximum value of the focused beam without the structures. A 5-fold increase in field amplitude is observed at the tips of the bridged structure compared to single nanocones.

the bridged nanocones is immediately apparent where a 5-fold increase of the field amplitude at the tip is calculated compared to the single nanocone. As previously reported [16] there is no significant field enhancement near the tips with the single and two nanocone systems. This is due to the fact that a longitudinal field, i.e., a field with a component along the cone height axis, is needed to concentrate the local field into the tip [16]. The addition of the metal bridge breaks the symmetry of the single cone, facilitating the necessary coupling of electric field to the tips without the longitudinal field component. Only a transverse field component along the bridge is required, making the structure more feasible. Since the 532 nm excitation wavelength is away from the fundamental surface plasmonic resonances of the structure, the field enhancement is due to plasmonic resonances of higher-order [9]. The bridged nanocones structure mimics a metallic SRR that is U-shaped (for example, [9, 10]) where the bridge acts as the base wire and the cones as the two arms of the ”U”. The difference is that our version of the SRR is a three-dimensional structure with a large height that engineers the fields far away from the glass surface. Additionally, the cone shape forces higher localized fields at the tips without creating additional field concentrations at the bridge-cone interface edges, as is the case for the U-shaped SRR [10], thus optimizing the use of the input excitation while eliminating the additional non-radiative heating.

4.1. Discussion

The simulation results agree well with the experimental data. Generally for SERS and TERS, the intensity is proportional to the fourth power of the electric field because the field enhance-

#135204 - $15.00 USD Received 17 Sep 2010; revised 21 Oct 2010; accepted 25 Oct 2010; published 27 Oct 2010

ment occurs twice in this regime: the incident and scattered fields are equivalently amplified by the same plasmonic oscillations. Since the experimental TERS intensities are due to the total TERS signals from the molecules nearby and adsorbed to the cones, the volume integral of the quartic electric field amplitude over the focal volume should provide a qualitative agreement with the experiments. From the calculation, this value is 5 times greater in the bridged nanocones structures relative to the single cone, while an 8-fold increase is observed in the experiment where the average TERS intensity of the three main CV peaks is considered. The discrepancy can be related to the fact that the TERS intensity dependency on the fourth power of the electric field only considers the electromagnetic field enhancement. For many SERS systems, where molecules are also absorbed on to the metal surface, an additional chemical effect, where charges exchange directly between the molecule and the metal, should also be considered (for example, [17]). The secondary effect would add to the enhancement of the Raman signal and was not considered in our calculation. This would explain the existence of TERS signal from the single nanocone and the disparity between the measured and calculated relative enhancement factors between the bridged and single cones structures.

The mechanisms for the fluorescence enhancement are different because radiative and non-radiative processes are involved including some quenching due to the metal [18]. Thus, although an increase in the fluorescence enhancement is also observed from the bridged nanocones, connecting the local electric field intensity to a fluorescence enhancement factor is not clear, even at an estimation level, and is beyond the scope of this study.

Based on our current simulations and previous works, it is apparent that improvements can be made to the engineering of the bridge and in tailoring the light to be more specific, in regards to wavelength and polarization, to the structure. For example, the use of higher-order modes for excitation, such as radial polarization, could better couple the input electric field with the cones and further concentrate the fields into the tips. The physical parameters of the bridge must also play a role and could be tailored specifically to an excitation wavelength and the relationship of its dimensions to those of the cones should also be considered. Nevertheless, the results are clear: the bridged nanocones structure offers a decisive improvement in Raman enhancement compared to single cones. As mentioned previously here, there have been a number of attempts to improve the nanocone performance through additional complicated steps such as utilizing multi-layers of materials or photonic coupling to other structures. The distinct advantage here is the lack of additional processing steps in the fabrication method while leading to an improved performance. The structure remains suitable for lab-on-a-chip applications such as analyte detection or even biological studies such as spectroscopy of cells. This conclusion can also open doors to more complicated structures where multiple cones are utilized.

Acknowledgement

Spanish Ministry of Science and Innovation (MICINNFIS2008-00114), Fundacion CELLEX Barcelona, the Academy of Finland (123109, 135084), and the Finnish Funding Agency for Technology and Innovation (40149/08). MJH acknowledges support from the Graduate School of Modern Optics and Photonics in Finland and the COST action MP0604. JMK acknowledges support from the graduate school of the Tampere University of Technology and Ulla Tuominen Foundation.

#135204 - $15.00 USD Received 17 Sep 2010; revised 21 Oct 2010; accepted 25 Oct 2010; published 27 Oct 2010

Tampereen teknillinen yliopisto
PL 527
33101 Tampere

Tampere University of Technology
P.O.B. 527
FI-33101 Tampere, Finland

ISBN 978-952-15-3073-9
ISSN 1459-2045